Sum Frequency Generation Vibrational Spectroscopy Studies on Model Peptide Adsorption at the Hydrophobic Solid-Water and Hydrophilic Solid-Water Interfaces

By

Roger Louis York

B.S. (California State University, Long Beach) 2003

A dissertation submitted in partial fulfillment of the

requirements for the degree of

Doctor of Philosophy

In

Chemistry

in the

GRADUATE DIVISION

of the

UNIVERSITY OF CALIFORNIA, BERKELEY

Committee in charge:

Professor Gabor A. Somorjai, Chair
Professor Phillip L. Geissler
Professor Y. Ron Shen

Fall 2007

The dissertation of Roger Louis York is approved:

_____

Chair Date

_____

Date

_____

Date

University of California, Berkeley

2007

Sum Frequency Generation Vibrational Spectroscopy Studies on Model Peptide Adsorption at the Hydrophobic Solid-Water and Hydrophilic Solid-Water Interfaces

by

Roger Louis York

Abstract

Sum Frequency Generation Vibrational Spectroscopy Studies on Model Peptide and Amino Acid Adsorption at the Hydrophobic Solid-Water and Hydrophilic Solid-Water Interfaces

by

Roger Louis York

Doctor of Philosophy in Chemistry

University of California, Berkeley

Professor Gabor A. Somorjai, Chair

Sum frequency generation (SFG) vibrational spectroscopy has been used to study the interfacial structure of several polypeptides and amino acids adsorbed to hydrophobic and hydrophilic surfaces under a variety of experimental conditions. Peptide sequence, peptide chain length, peptide hydrophobicity, peptide side-chain type, surface hydrophobicity, and solution ionic strength all affect an adsorbed peptide's interfacial structure. Herein, it is demonstrated that with the choice of simple, model peptides and amino acids, surface specific SFG vibrational spectroscopy can be a powerful tool to elucidate the interfacial structure of these adsorbates.

Herein, four experiments are described. In one, a series of isosequential amphiphilic peptides are synthesized and studied when adsorbed to both hydrophobic and

hydrophilic surfaces. On hydrophobic surfaces of deuterated polystyrene, it was determined that the hydrophobic part of the peptide is ordered at the solid-liquid interface, while the hydrophilic part of the peptide appears to have a random orientation at this interface. On a hydrophilic surface of silica, it was determined that an ordered peptide was only observed if a peptide had stable secondary structure in solution. In another experiment, the interfacial structure of a model amphiphilic peptide was studied as a function of the ionic strength of the solution, a parameter that could change the peptide's secondary structure in solution. It was determined that on a hydrophobic surface, the peptide's interfacial structure was independent of its structure in solution. This was in contrast to the adsorbed structure on a hydrophilic surface, where the peptide's interfacial structure showed a strong dependence on its solution secondary structure. In a third experiment, the SFG spectra of lysine and proline amino acids on both hydrophobic and hydrophilic surfaces were obtained by using a different experimental geometry that increases the SFG signal. Upon comparison of these spectra to the SFG spectra of interfacial polylysine and polyproline it was determined that the interfacial structure of a peptide is strongly dependent on its chain length. Lastly, SFG spectroscopy has been extended to the Amide I vibrational mode of a peptide (which is sensitive to peptide secondary structure) by building a new optical parametric amplifier based on lithium thioindate. Evidence is presented that suggests that the interfacial secondary structure of a peptide can be perturbed by a surface.

Professor Gabor A. Somorjai
Dissertation Committee Chair

Contents

List of Figures

List of Tables

Acknowledgements

I would like to thank Prof. Gabor A. Somorjai for giving the opportunity to accomplish what I have. He has taught me how to advance science by an order of magnitude, and his advice and help will not be soon forgotten. I would also like to thank my undergraduate advisor, Prof. Krzysztof (Kris) Slowinski. His mentorship taught me to love science, and if it wasn't for him, I would have never made it to Berkeley.

While at Berkeley, I met someone very special who I love very much, Katie M. Bratlie. Her love, support, and our shared time together meant the world to me, and I look forward to our future together. Thank you, and I love you, Katie.

My co-workers in the Somorjai group have been the most valuable resource of my graduate career. At the beginning, I primarily interacted with Ozzy Mermut, a postdoc who was also a very dear friend, and Diana C. Phillips, an older graduate student who was also a good friend. Later, I primarily worked with George J. Holinga, another co-worker that I am proud to call a friend. I feel confident leaving the future of this project in his hands. William K. Browne (one of my best friends whose interactions will not soon be forgotten) and Phillip L. Geissler have provided theoretical advice and study that has proven invaluable to this project. Without the help and patient advice of Keith R. McCrea and Sasha J. Kweskin, this thesis would have never made it off the ground. They taught me the basics of SFG, and Keith unselfishly helped me implement many of the ideas we had. Telly Koffas and Jamie Kim should be thanked for all their training of me during my first months in the Somorjai group.

This project is extremely interdisciplinary in nature, requiring the advice of a wide range of scientists. I would like to thank David King (HHMI) for invaluable help in

both the synthesis and characterization of the peptides described in this thesis. Kevin Healy (Bioengineering) provided access to the QCM we used (training by Beth Irwin and Naomi Kohen). Carolyn Bertozzi also provided access to equipment used in peptide synthesis and purification (training by Jennifer Prescher and Sarah Hubbard). Susan Marqusee (MCB) provided access to her Circular Dichroism instrument (training by Tracy Young). I would like to thank all the professors who took time to discuss my project with me (including, but not limited to, Susan Marqusee, Arup Chakraborty, David Chandler, and Ron Shen). A few minutes with them advanced the intellectual level of my research by several levels. In fact, that it what I will miss most about Berkeley: the interdisciplinary and open-access approach to science.

There are several Somorjai past and present members that I have worked indirectly with. Derek Butcher, Lucio Flores, Rob Rioux, Mike Ferguson, Jeong Park, James Hoefelmeyer, Max Montano, Anthony Contreras, Chris Kliewer, Russ Renzas, Yuri Borodko, Jeff Grunes, Xianqiao Liu, Kevin Becraft, Andy Marsh, Leonid Belau, Marco Bieri, Wenyu Huang, Feng Tao, Tianfu Zhang, Yawen Zhang, Louis Jones, Staffan Westerberg, David Tang, Xiaoming (Mike) Yan, Eric Ji, and Mario Farias are just some of the people I will not forget soon.

Most importantly, I would like to take this opportunity to thank my family making me who I am today. My father, Roger Lynn York, and my mother, Linda Marie York, deserve tremendous thanks, in addition to my aunts, uncles, and grandparents. I would not be here today if it wasn't for you.

There are several people I would like to thank for making my time in Berkeley so enjoyable. Elad Harel has proven to be one of my best friends, and the memories of our

Berkeley experience will not be forgotten. Bradley Compton and Jennifer Blough were wonderful roommates that made the “eigenspot” what it was. Matt Prantil’s help and hard work during our first year was much appreciated, and he has become a good friend. Amber Wise, Allon Hochbaum, Elizabeth Read (Dizzle), Mike Hagan, Sander Pronk, John “CJ” Herbert, and Jason Locasale are friends that I greatly enjoyed interacting with, both professionally and socially.

And I thank the government agencies that supported this work. This work was supported by the Director, Office of Science, Office of Basic Energy Sciences, Materials Sciences and Engineering Division, of the U.S. Department of Energy under Contract No. DE-AC02-05CH11231. Additional support was provided by the NIH through grant R21EB005262.

Chapter 1

Introduction

The molecular understanding of protein adsorption on biopolymer surfaces provides the opportunity to develop biocompatible implant systems or prevent unfavorable protein adsorption from the blood onto medical devices, which alters their biological and immunological responses.[1,2] Because of this, both the biomedical and surface science communities have taken an interest in understanding protein adsorption.[3] Although protein adsorption has been the focus of many studies, details on the molecular structure of adsorbed proteins remains poorly understood. This is primarily due to the lack of a surface-specific technique that provides information on molecular structure at surfaces. Recently, the surface-specific technique of visible-infrared sum frequency generation (SFG) vibrational spectroscopy has been developed.[4,5] This vibrational spectroscopy provides a molecular level understanding of adsorbate orientation and ordering at any interface accessible by light. Unfortunately, adsorbed proteins are difficult molecules to study with vibrational spectroscopy on a molecular level due to their size and structural complexity. Therefore, we have turned to the study of amino acids and small peptides as model systems. In this dissertation, we will discuss their adsorption onto hydrophobic and hydrophilic surfaces studied by SFG.

SFG is a surface-specific vibrational spectroscopy that was first demonstrated in 1987.[6-8] As will be discussed in Chapter 2, SFG allows for the determination of orientation and ordering of the vibrational modes of interfacial molecules. In SFG, two

pulsed optical beams, one having a frequency in the visible range (ω_{vis}) and the other having a frequency in the infrared region (ω_{IR}) are overlapped in space and time at a surface. Through a non-linear wave mixing process, a beam at the sum-frequency ($\omega_{SFG} = \omega_{vis} + \omega_{IR}$) is created in both the reflected and transmitted directions. The intensity of reflected light at the sum frequency is measured as a function of ω_{IR}. As ω_{IR} is tuned over a frequency range, interfacial molecules will come into resonance with ω_{IR}, at which point the intensity of the sum-frequency light will become enhanced. This allows for a surface-specific vibrational spectroscopy.

Chapter 3 discusses the application of SFG to study the interfacial structure of a series of model peptides at hydrophobic solid/water and hydrophilic solid/water interfaces. It was found that hydrophobic parts of peptides are ordered at hydrophobic interfaces. Conversely, it was observed that peptides do not order at hydrophilic surfaces, with the exception of peptides with well defined secondary structure in solution. In this case, it appears that the hydrophilic portion of the peptide is ordered at the interface. Additionally, the effect of peptide chain length and sequence was examined. It was found that at the hydrophobic solid/water interface, the most hydrophobic side-chains interfacial orientation was largely independent of peptide chain length and sequence; side-chains of less hydrophobicity (yet still considered hydrophobic) were shown to have an interfacial orientation that depended on peptide chain-length and sequence. Hydrophilic side-chains were not observed to order at the hydrophobic solid/water interface.

Chapter 4 discusses the influence of the ionic strength of a solution on the adsorbed structure of a model peptide, LK_{14}. This peptide is known to be an α-helix if the ionic strength is sufficiently high, otherwise, this peptide is a random coil. On a

hydrophobic surface, it is shown that the observed ordering of the hydrophobic leucine side-chains is independent of the ionic strength of the solution (and hence the peptides' secondary structure in solution). In the absence of peptide, the interfacial water structure at the hydrophobic solid/water interface is independent of the ionic strength of the solution. This is in contrast to the situation when LK_{14} is adsorbed to the hydrophobic solid/water interface, when the interfacial water ordering shows a clear dependence on the ionic strength of the solution. At the hydrophilic interface, the ordering of the hydrophilic part of LK_{14} is only observed unambiguously when the peptide has well defined secondary structure in solution. The interfacial water structure at this surface is shown to depend on the ionic strength of the solution, whether or not there is adsorbed peptide at this interface.

Chapter 5 deals with SFG studies of individual amino acids and long polypeptides at both hydrophobic and hydrophilic interfaces. The SFG spectra of adsorbed peptides at the solid/liquid interface were not observed previously, most likely due to poor SFG sensitivity to molecules that show weak interfacial ordering. It was determined that amino acids always show less side-chain ordering than long peptides, at both hydrophobic and hydrophilic surfaces. Additionally, it is shown that completely hydrophilic peptides, such has polylysine, show different interfacial structure than ampliphilic peptides at both hydrophobic and hydrophilic surfaces. In order to collect these spectra, total internal reflection SFG was employed. This is discussed in detail in chapter 5.

Chapter 6 deals with extending SFG spectroscopy to longer infrared wavelengths, allowing for the measurement of the Amide I vibrational mode of the peptide backbone.

This was done by building a new Optical Parametric Amplifier, which is discussed in detail in chapter 6. The Amide I mode was observed to be at the same frequency for LK14 (adsorbed to the hydrophobic solid/water interface) under both high and low solution ionic strength conditions. This was interpreted as the peptide having the same secondary structure at the interface, independent of the peptides' solution secondary structure. However, this interpretation could be incorrect, and other possible interpretations are discussed. At the hydrophilic solid/water interface, this mode was blue-shifted, indicating a change in its interfacial secondary structure, relative to the hydrophobic solid/water interface.

References

(1) Castner, D. G.; Ratner, B. D. *Surface Science* **2002**, *500*, 28-60.

(2) Kasemo, B. *Current Opinion in Solid State and Materials Science* **1998**, *3*, 451-459.

(3) Somorjai, G. A.; York, R. L.; Butcher, D.; Park, J. Y. *Physical Chemistry Chemical Physics* **2007**, *9*, 3500-3513.

(4) Lambert, A. G.; Davies, P. B.; Neivandt, D. J. *Applied Spectroscopy Reviews* **2005**, *40*, 103-145.

(5) Shen, Y. R.; Ostroverkhov, V. *Chemical Reviews* **2006**, *106*, 1140-1154.

(6) Hunt, J. H.; Guyot-Sionnest, P.; Shen, Y. R. *Chemical Physics Letters* **1987**, *133*, 189-192.

(7) Zhu, X. D.; Suhr, H.; Shen, Y. R. *Physical Review B* **1987**, *35*, 3047-3050.

(8) Harris, A. L.; Chidsey, C. E. D.; Levinos, N. J.; Loiacono, D. N. *Chemical Physics Letters* **1987**, *141*, 350-356.

Chapter 2

Sum Frequency Generation

Sum frequency generation is a powerful surface-specific vibrational spectroscopy with sub-monolayer sensitivity. Isotropic materials, such as the gas phase, do not produce sum frequency signal, allowing only adsorbates present on the surface to contribute to the spectrum. This allows SFG to be an extremely useful tool for vibrational studies of catalytic reactions performed at high pressures.

2.1. Sum Frequency Generation Theory

Sum frequency generation vibrational spectroscopy (SFG) was first observed[1] and described[2,3] in the 1960s. However, the technique was not developed into a surface-specific vibrational spectroscopy until the 1980s by the groups of Shen[4,5] and Harris.[6] Since then, SFG as a technique for vibrational spectroscopy has been extensively described.[7-17] An excellent review that gives a simplistic picture has been published recently.[18] The principle of SFG is regulated by second-order nonlinear optics, and the technique itself is permitted by high-energy pulsed lasers. Under weak electric fields, the polarization $\vec{P}$ (or dipole moment per unit volume) expansion has two terms as shown in equation 2.1, where $\vec{P}^{(0)}$ is the static polarization, $\vec{P}^{(1)}$ is the first-order linear polarization, ε_0 is the permittivity of free space, $\vec{\chi}^{(1)}$ is the linear susceptibility, t is time, and $\vec{E}(r)\cos(\omega t)$ describes the electric field.

$$\vec{P} \approx \vec{P}^{(0)} + \vec{P}^{(1)} = \vec{P}^{(0)} + \varepsilon_0 \vec{\chi}^{(1)} \vec{E}(r)\cos(\omega t) \qquad (2.1)$$

For linear optics, this equation shows that the frequency of the light is invariant as it passes through a medium.

Under strong electric fields, the polarization can be further expanded to include higher-order terms.

$$\vec{P} \approx \vec{P}^{(0)} + \vec{P}^{(1)} + \vec{P}^{(2)} + \vec{P}^{(3)} + \ldots \tag{2.2}$$

The second-order polarization, $P_i^{(2)}$, where $\chi_{ijk}^{(2)}$ is the second-order nonlinear susceptibility and $\vec{E}_j(r)\cos(\omega_1 t)$ and $\vec{E}_k(r)\cos(\omega_2 t)$ are the two input fields at different frequencies, is given by equation 2.3

$$P_i^{(2)} = \varepsilon_0 \sum_{j,k} \chi_{ijk}^{(2)} \vec{E}_j(r)\cos(\omega_1 t)\vec{E}_k(r)\cos(\omega_2 t) \tag{2.3}$$

Which can be rearranged to form

$$P_i^{(2)} = \tfrac{1}{2}\varepsilon_0 \sum_{j,k} \chi_{ijk}^{(2)} \vec{E}_j(r)\vec{E}_k(r)\left[\cos(\omega_1 + \omega_2)t + \cos(\omega_1 - \omega_2)t\right]. \tag{2.4}$$

Equation 2.4 illustrates how the frequency of light can change after passing through a medium, resulting in a SFG and difference frequency generation (DFG). A more general form of eq. 2.4 is given in Chapter 1 of Boyd.[19] In SFG vibrational spectroscopy, ω_1 is typically chosen to be in the visible region of the spectrum while ω_2 is in the infrared.

The sum frequency radiation is strongly peaked in one direction determined by phase matching conditions. Efficient energy transfer from the ω_{vis} and ω_{IR} to the sum frequency ω_{SF} occurs when both energy and momentum are conserved. Energy conservation requires that $\omega_{SF} = \omega_{vis} + \omega_{IR}$, while momentum conservation requires

$$\vec{k}_{SF} = \vec{k}_{vis} + \vec{k}_{IR}. \tag{2.5}$$

Equation 2.5 can be rewritten for the angles of incidence for the visible and infrared beams.

$$k_{SF}\sin\theta_{SF} = k_{vis}\sin\theta_{vis} + k_{IR}\sin\theta_{IR} \tag{2.6}$$

where k_{SF}, k_{vis}, and k_{IR} are the three wavenumbers ($2\pi/\lambda$), θ_{vis} and θ_{IR} are the angles of incidence compared to the surface normal of the visible and IR laser beams, and θ_{SF} is the angle of the sum frequency radiation. From this equation, it can be noted that the angle of emission changes as ω_{IR} is scanned over the spectrum.

The magnitude of the SFG signal is proportional to the absolute square of $\chi^{(2)}_{eff}$ shown in equation 2.7.

$$I(\omega_{SF}) \propto \left|\chi^{(2)}_{eff}\right|^2 \propto \left|\sum_q \chi^{(2)}_{R,q} + \chi^{(2)}_{NR}\right|^2 \tag{2.7}$$

$\chi^{(2)}_{eff}$ is comprised of both a non-resonant susceptibility term, $\chi^{(2)}_{NR}$, and a resonant susceptibility term, $\chi^{(2)}_{R,q}$ of the q^{th} vibrational mode. A more explicit relationship between I_{SFG} and $\chi^{(2)}$ depends on the experimental geometry and is discussed in chapter 5. The non-resonant susceptibility term arises from non vibrational resonant excitations (e.g. electronic excitations) and is typically invariant as the IR beam is scanned over the spectrum.

The surface specificity in SFG arises from the fact that $\chi^{(2)}$ is a third rank tensor whose element values depend on the properties of the medium under investigation. For centrosymmetric media, $\chi^{(2)}$ should be invariant under inversion symmetry, however, the electric field and the polarization must change signs as vectors. From equation 2.3,

one can see that the inversion operator will result in $\chi^{(2)} = -\chi^{(2)}$ or $\chi^{(2)} = 0$, thus yielding no SFG signal from media with inversion symmetry. At interfaces, inversion symmetry is necessarily broken, allowing light at the sum-frequency to be created.

The resonant susceptibility, which originates from vibrational modes on the surface, can be described by equation 2.8.

$$\chi_R^{(2)} = N\chi_{ijk}^{(2)} \sum_q \sum_{i,j,k} \langle (\hat{i}\cdot\hat{l})(\hat{j}\cdot\hat{m})(\hat{k}\cdot\hat{n})\rangle \frac{A_q}{\omega_{IR} - \omega_q + i\Gamma_q} \Delta\rho_{gq} \qquad (2.8)$$

where A_q is the strength of the q[th] vibrational mode, N is the number density of molecules on the surface, ω_{IR} is the frequency of the infrared laser beam, ω_q is the frequency of the q[th] vibrational mode, Γ_q is the damping constant of the q[th] vibrational mode, and $\Delta\rho_{gq}$ is the population difference between the ground and first excited states. The subscripts l, m, and n refer to the axes for the molecular coordinate system (whereas the subscripts i, j, and k refer to the laboratory coordinate systems) and so the expression, $\langle (\hat{i}\cdot\hat{l})(\hat{j}\cdot\hat{m})(\hat{k}\cdot\hat{n})\rangle$, is the coordinate transformation from molecular fixed coordinates to laboratory fixed coordinates averaged over molecular orientations. Since this average is over all of the molecular orientations, the adsorbates must have some ordering to produce a sum frequency signal. This is an important selection rule that is used throughout this thesis to understand the measured SFG spectra. To understand this result, the orientational average can be rewritten in a more intuitive form:

$$\chi_{R,q}^{(2)} = N\int a_q^{(2)}(\Omega) f(\Omega) d\Omega \qquad (2.9)$$

where $a_q^{(2)}$ is the second-order susceptibility for the q[th] vibrational mode of an individual molecule, Ω represents three Euler angles that describe a transformation between the

laboratory and molecular coordinate frames, and $f(\Omega)$ represents an orientational distribution function of the q[th] vibrational mode. As can be seen from equation 2.9, this integral will vanish if $f(\Omega)$ is a uniform function. From equation 2.8, one can see that $\chi_R^{(2)}$ reaches a maximum when $\omega_{IR} = \omega_q$, and hence a vibrational spectrum is acquired by scanning the IR frequency.

Selection rules for the SFG process can be inferred from equation 2.10.[19,20]

$$a_q^{(2)} = \frac{1}{2\omega_q} \frac{\partial \mu_n}{\partial q} \frac{\partial \alpha_{lm}^{(1)}}{\partial q} \tag{2.10}$$

where μ_n is the dipole moment and $\alpha_{lm}^{(1)}$ is the Raman polarizability. Hence, in order for $\chi_{R,q}^{(2)}$ to be non-zero, the vibrational mode of interest must be both IR and Raman active.

2.2. Sum Frequency Generation from a Surface

In general, the surface susceptibility $\chi_{ijk}^{(2)}$ is a 27-element tensor, however, it can often be reduced to several non-vanishing elements by symmetry constraints. Interfaces are isotropic in the plane of the surface. The symmetry constraints for an in-plane isotropic surface reduces $\chi_{ijk}^{(2)}$ to the following four independent non-zero elements:[18]

$$\chi_{zzz}^{(2)}; \chi_{xxz}^{(2)} = \chi_{yyz}^{(2)}; \chi_{xzx}^{(2)} = \chi_{yzy}^{(2)}; \chi_{zxx}^{(2)} = \chi_{zyy}^{(2)}. \tag{2.11}$$

Here z is defined to be the direction normal to the surface, x is perpendicular to z and in the plane of incidence of the light, and y is perpendicular to both z and x. These four independent elements contribute to the SFG signal under four different polarization conditions: ppp, ssp, sps, and pss, where the polarizations are listed in order of decreasing frequency (SF, vis, IR). P polarization occurs when the electrical field vector is parallel

to the plane of incidence, which contains the surface normal and the incident beam (and hence contains both x and z polarized light). The vector is perpendicular to the plane of incidence in s polarization (and hence contains y polarized light).

Information about molecular orientation of the adsorbate on the surface may be determined using different polarization combinations of IR, vis, and SF radiation.[21,22] Different susceptibility components are measured for each polarization combination used during an SFG experiment. These polarization combinations determine the ratios of the different tensor elements, which provide molecular orientation information. The orientation of adsorbates can be extracted through modeling of the susceptibility components. However, this approach is limited when studying the interfacial orientation of a molecule as complex as a peptide containing one or two types of amino acids. This is because each side chain could have its own orientation distribution, making quantitative analysis difficult. Other problems with this approach have been discussed.[17,23] Therefore, all spectra presented here are in the *ssp* polarization combination. Finally, water is always present when peptides are adsorbed to surfaces. SFG studies on the interfacial properties of water have been performed and recently extensively reviewed.[16]

2.3. Sum Frequency Generation Setup

All SFG spectra were obtained using a mode-locked Nd:YAG laser (Leopard D20, Continuum). This laser produces a 1064 nm fundamental having a 20 ps long pulse with a 20 Hz repetition rate. The 1064 nm beam is split, with some light being frequency doubled to 532 nm in a KTP crystal. This 532 beam is also split, with some of the light becoming the visible (vis) beam for the experiment, and the rest going to an optical parametric generator (OPG) that produces light at a wavelength of ~0.8 and ~1.2

microns. This ~1.2 micron light is sent to a second stage (the optical parametric amplifier or OPA stage). The tunable IR beam for the SFG experiment was generated in a pair of KTA crystals (the OPA stage) by difference frequency mixing of the 1064 nm beam with the output of a KTP OPG (~1.2 microns). A schematic of the OPA/OPG is illustrated in figure 2.1. The VIS beam (200 μJ) and the IR (200 μJ) beams were spatially and temporally overlapped on the sample surface. The generated SFG beam was sent through a monochromator and the signal intensity was detected with a photomultiplier tube (Hamamatsu) and a gated integrator (Stanford Research) as the IR beam was scanned over the range of interest.

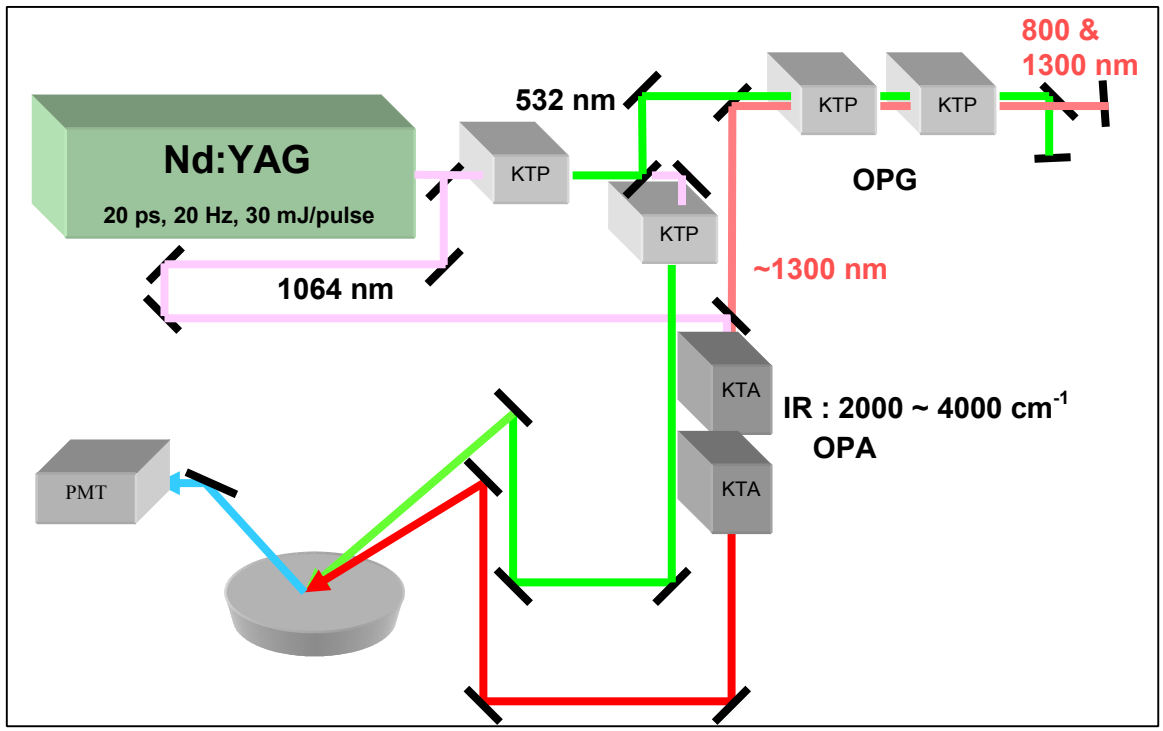

Figure 2.1. *Schematic of OPG/OPA system to generate laser beams used for SFG experiments. Tuning range is between 2000 and 4000 cm^{-1}.*

References

(1) Bass, M.; Franken, P. A.; Hill, A. E.; Peters, C. W.; Wieinreich, G. *Physical Review Letters* **1962**, *8*, 18-18.

(2) Bloembergen, N.; Pershan, P. S. *Physical Review* **1962**, *128*, 606-622.

(3) Bloembergen, N. *Nonlinear Optics*; Benjamin: New York, NY, 1965.

(4) Hunt, J. H.; Guyot-Sionnest, P.; Shen, Y. R. *Chemical Physics Letters* **1987**, *133*, 189-192.

(5) Zhu, X. D.; Suhr, H.; Shen, Y. R. *Physical Review B* **1987**, *35*, 3047-3050.

(6) Harris, A. L.; Chidsey, C. E. D.; Levinos, N. J.; Loiacono, D. N. *Chemical Physics Letters* **1987**, *141*, 350-356.

(7) Shen, Y. R. *Nature* **1989**, *337*, 519-525.

(8) Shen, Y. R. *Annual Review of Physical Chemistry* **1989**, *40*, 327-350.

(9) Shen, Y. R. *Surface Science* **1994**, *299/300*, 551-562.

(10) Shen, Y. R. *The Principles of Nonlinear Optics*; Wiley: New York, 2003.

(11) Du, Q.; Superfine, R.; Freysz, E.; Shen, Y. R. *Physical Review Letters* **1996**, *70*, 2313-2316.

(12) Johal, M. S.; Ward, R. N.; Davies, P. B. *Journal of Physical Chemistry* **1996**, *100*, 274-279.

(13) Conboy, J. C.; Messmer, M. C.; Richmond, G. L. *Journal of Physical Chemistry* **1996**, *100*, 7617-7622.

(14) Buck, M.; Himmelhaus, M. *Journal of Vacuum Science and Technology A-Vacuum Surfaces and Films* **2001**, *19*, 2717-2736.

(15) Hirose, C.; Akamatsu, N.; Domen, K. *Applied Spectroscopy* **1992**, *46*, 1051-1072.

(16) Shen, Y. R.; Ostroverkhov, V. *Chemical Reviews* **2006**, *106*, 1140-1154.

(17) Wang, H. F.; Gan, W.; Lu, R.; Rao, Y.; Wu, B. H. *International Reviews of Physical Chemistry* **2005**, *24*, 191-256.

(18) Lambert, A. G.; Davies, P. B.; Neivandt, D. J. *Applied Spectroscopy Reviews* **2005**, *40*, 103-145.

(19) Boyd, R. W. *Nonlinear Optics*; 2nd ed.; Academic Press: San Diego, 2003.

(20) Shen, Y. R. *The Principles of Nonlinear Optics*; Wiley: New York, NY, 1984.

(21) Hirose, C.; Yamamoto, H.; Akamatsu, N.; Domen, K. *Journal of Chemical Physics* **1993**, *97*, 10064-10069.

(22) Wei, X.; Hong, S. C.; Zhuang, X. W.; Goto, T.; Shen, Y. R. *Physical Review E* **2000**, *62*, 5160-5172.

(23) Simpson, G. J.; Rowlen, K. L. *Journal of the American Chemical Society* **1999**, *121*, 2635-2636.

Chapter 3

Side Chain, Chain Length, and Sequence Effects on Amphiphilic Peptide Adsorption at Hydrophobic and Hydrophilic Surfaces Studied by Sum-Frequency Generation Vibrational Spectroscopy and Quartz Crystal Microbalance

The surface molecular structure and adsorbed mass of a series of model amphiphilic peptides have been studied in situ with surface-specific sum frequency generation (SFG) vibrational spectroscopy and quartz crystal microbalance (QCM) at the hydrophobic polystyrene and hydrophilic silica solid-water interface. The peptides are designed to form α-helical (XY_{14}) or β-strand (XY_7) secondary structures at an apolar interface and contain hydrophobic (X) and charged (Y) amino acids with sequence Ac-XYYXXYXXYYXXYX-NH_2 or Ac-XYXYXYX-NH_2, respectively. The X and Y combinations are leucine (L) and lysine (K), alanine (A) and lysine (K), alanine (A) and arginine (R), and phenylalanine (F) and arginine (R). One additional peptide with sequence Ac-LKKLLKL-NH_2 (LK_7 α) was synthesized. These peptides allow for the study of how chain length (LK_{14} vs LK_7 α and LK_7 β), amino acid side chain character (LK vs AK vs AR vs FR), and sequence (LK_7 α-helix vs LK_7 β-strand sequences) affect adsorption. The SFG spectra of adsorbed peptides on polystyrene typically show CH resonances characteristic of the hydrophobic side chains oriented at the interface. On polystyrene, the molecular orientation of the side chain of alanine is more sensitive to

changes in peptide chain length and sequence than that of leucine or phenylalanine. The SFG spectra of adsorbed peptides on silica show no distinct peptide modes, with the exception of the LK_{14} peptide, where an amide A NH mode is observed. The results demonstrate that SFG vibrational spectra can fingerprint specific amino acid ordering occurring at the polystyrene interface and secondary structure ordering at the silica interface. QCM data indicates that all peptides except LK_7 β adsorb onto both hydrophobic polystyrene and hydrophilic silica surfaces, even when SFG active modes are not observed.

3.1. Introduction

Protein adsorption at the solid-liquid interface is involved in a wide range of phenomena in nature and in many industrial applications. It is of great interest to the scientific and medical communities due to its application in implant biocompatibility, drug delivery, and biosensors.[1-4] An example of unfavorable protein adsorption is the adsorption of blood proteins onto medical devices, which subsequently alter their biological and immunological responses.[5,6] Understanding protein adsorption may provide the means to exert molecular control of surface properties of biomaterials. Proteins are composed of chains of amino acids, which form secondary structural motifs including α-helices and β-sheets. The secondary structures associate to form tertiary domains, which assemble to form the unique three-dimensional structure of proteins. Proteins are such large and complex molecules that it is difficult to identify the features in their structure that lead to adsorption and interaction with solid surfaces. Designed peptides provide simple model systems for understanding protein adsorption.[7] Depending on the amino acid sequence of a peptide, different secondary structures (α-helix and β-sheet) can be induced at apolar interfaces.[8] Having a well-defined model system allows experiments to be carried out under controlled conditions, where it is possible to investigate the affects of peptide amino acid sequence and chain length, concentration, buffering effects, etc. on adsorbed peptide structure.[9,10] The present work examines the molecular-level behavior of designed polypeptides adsorbed onto hydrophobic polystyrene and hydrophilic silica using sum frequency generation (SFG) vibrational spectroscopy and quartz crystal microbalance (QCM) to study the molecular surface

structure and adsorbed amount of biological molecules at the solid-liquid interface. SFG vibrational spectroscopy has been used to study protein adsorption at the buried interface with molecular-level surface specificity.[11,12] SFG spectroscopy is a nonlinear optical process where two input beams (typically a fixed frequency visible and tunable infrared) overlap at a surface and generate light at the sum frequency. The selection rules for SFG require molecules to be in a noncentrosymmetric environment, such as an interface, to produce a SFG signal. Additionally, only molecules that have a net ordering at an interface (i.e., only molecules that do not have a random geometric distribution) produce a SFG signal.[13] SFG spectroscopy is used here to carry out a systematic adsorption study of synthetic amphiphilic peptides (composed of one hydrophobic amino acid and one charged amino acid) on polystyrene and silica. QCM is used to quantify the adsorption on each surface. The model peptides are designed with a specific sequence and length to induce formation of an α-helix or β-strand structure at an apolar interface.[8,14] Unlike proteins, which contain numerous types of amino acids that make identification of SFG active vibrational modes difficult,[15,16] these peptides contain only two amino acids, which leads to more easily interpretable SFG spectra. By systematically varying such parameters as the amino acid side chain type, chain length, and sequence in a set of peptides, it is possible to examine how each parameter influences interfacial molecular structure and amount adsorbed. On polystyrene, we measure a local hydrophobic interaction (alignment of the hydrophobic residues) that is unique to the amino acid and provides a spectroscopic signature attributed to individual amino acid side chains. Unambiguous assignment of SFG vibrational modes for leucine, alanine, and phenylalanine in a peptide is possible. On silica, we measure a molecular scale surface

interaction, where only peptides that possess a stable secondary structure in solution yield SFG active modes attributed to the peptide.

3.2. Experimental

3.2.1. Peptide Synthesis. Peptides were synthesized using an Applied Biosystems ABI 431A synthesizer using rink amide 4-methylbenzhydrylamine (MBHA) resin (Nova Biochem) and standard 9-fluorenylmethyloxycarbonyl (FMOC) chemistry.[17] Approximately 200 mg of rink amide resin was used in the synthesis, with a 9 equiv excess of reagents. The N-terminus of the peptide was acetylated by adding acetic anhydride to the resin-bound peptide prior to cleaving in a solution of 95% trifluoroacetic acid in water. The crude peptides were purified by reversed-phase high-pressure liquid chromatography (rp-HPLC) with a C-18 column (Vydac) where possible. Hydrophobic peptides were not HPLC purified due to low solubility and retention on the HPLC column. The purity and composition of the peptides were characterized using LC-ESI-MS (electrospray ionization) mass spectrometry. Peptides were precipitated in cold methyl-*tert*-butyl ether and lyophilized to dryness.

The peptides contain hydrophobic (X) and charged (Y) amino acids with sequence Ac-XYYXXYXXYYXXYX-NH_2 or Ac-XYXYXYX-NH_2, where the X and Y combinations are leucine (L) and lysine (K), alanine (A) and lysine (K), alanine (A) and arginine (R), and phenylalanine (F) and arginine (R) (Figure 3.1). The 14-amino acid peptides were sequenced to induce α-helical formation at an apolar interface, while the 7-amino acid peptides were sequenced to induce β-strand formation.[8,14] One additional 7-amino acid peptide was synthesized, with sequence Ac-LKKLLKL-NH_2, referred to as LK_7 α. This

peptide was designed to form a helix; however, it may contain fewer than the nominal number of residues required to stabilize helix formation.[8]

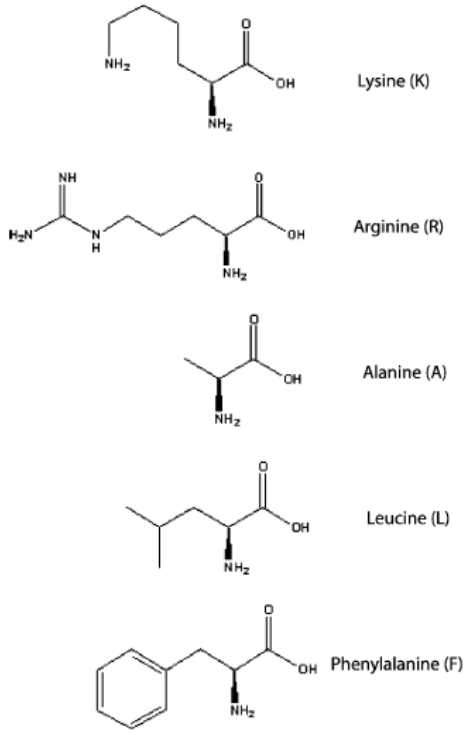

Figure 3.1. *Amino acids used in model synthetic peptides. Lysine (pK_a = 10.8) and arginine (pK_a = 12.5) have positively charged side chains containing ionizable NH_2 moieties, while the nonpolar side chains of alanine, leucine, and phenylalanine are composed of methyl, isopropyl, and phenyl side chains, respectively.*

Peptide solutions were prepared using phosphate-buffered saline (PBS, 0.01 M phosphate buffered saline, 0.14 M NaCl, 0.0027 M KCl, Aldrich) solution. The LK, AK, AR, and FR peptides used in this study all had drastically different solution solubilities, so we were unable to perform all of the experiments at the same peptide concentration. We observed that the peptide solubility decreased in the order AR ~ AK > LK > FR.

3.2.2. Circular Dichroism (CD) Measurements. CD spectra were collected between 190 and 240 nm with 1 s averaging and 1 nm increments using an Aviv 62DS circular dichroism instrument. Lyophilized peptides samples were dissolved in PBS solution in a 1 mm strain-free (Aviv) cuvette.

3.2.3. QCM Measurements. QCM is a highly sensitive mass sensor capable of measuring nanogram quantities of adsorbed material on surfaces.[18] The wet mass adsorbed (Δm) induces a linear resonant frequency shift (Δf) according to eq. 3.1, provided that the adsorbed mass in a liquid environment is evenly distributed and produces a sufficiently rigid and thin film (i.e., elastic masses are adsorbed).[19] In eq. 3.1, n denotes the overtone number and C is the mass sensitivity constant for $\Delta f = 1$ Hz (17.7 ng·cm^{-2} using a 5 MHz crystal).

$$\Delta m = \frac{-C\Delta f}{n} \tag{3.1}$$

We used a Q-Sense D300 model QCM for all measurements. SiO_2-coated sensor crystals (Q-Sense QSX 303, AT-cut, 5 MHz, active surface area = 0.2 cm^2) were used following oxygen plasma treatment or coated with polystyrene films for use as a hydrophobic substrate. The polystyrene surface was prepared by spin-casting (Specialty Coating Systems, P-6000 spin-coater) a 2 wt % solution of polystyrene (MW ~ 280 000, polydispersity = 1.05, Aldrich) in toluene onto the fused silica substrate and annealing at 110 °C (12 h). The silica or polystyrene coated sensor crystal was initially stabilized in pH 7.4 PBS solution. After a stable resonant crystal frequency was observed, a volume of ~2 mL of temperature-stabilized peptide sample liquid was delivered to the chamber

containing the sensor crystal (internal volume 80 μL) to ensure a complete exchange of the liquid. Signal distortion (peaks of Δf < 5 Hz) was observed briefly upon sample injection due to temperature and pressure fluctuations in the cell. Measurements of f were acquired at several harmonics (15, 25, and 35 MHz) simultaneously, beginning when the crystal was stabilized in buffer solution until a steady-state frequency was reached following peptide adsorption (typically ~60 min). All measurements were performed at a temperature of 24-25 °C to within 0.5 °C. The QCM liquid cell was thoroughly cleaned with Hellmanex between measurements.

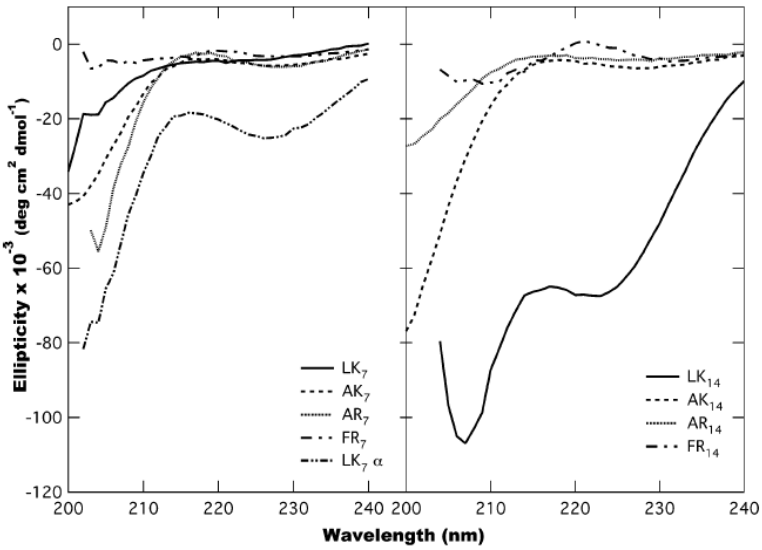

Figure 3.2. *CD spectra of model amphiphilic peptides: 7-amino acid peptides (left) and 14-amino acid peptides (right). Only LK_{14} has a predominantly α-helical structure in solution.*

3.2.4. SFG Spectroscopy. Our laser experimental setup, substrate preparation, and experimental geometry have been described in detail elsewhere.[20,21] Briefly, fused silica

windows (Esco Products) were used as the hydrophilic substrate following cleaning in NOCHROMIX (Godax Laboratories) oxidizing solution. Polystyrene thin films (200 nm) were prepared similarly to the QCM crystal substrates by spin-casting a 3 wt % solution of deuterated polystyrene (PS-d_8, MW ~ 300 000, polydispersity = 1.17, Polymer Source, Inc.) onto the fused silica windows. Deuterated polystyrene was used for SFG measurements to eliminate vibrational modes of the substrate from the spectral region under study (2800-3600 cm^{-1}). Background PBS spectra were obtained on the cleaned silica or PS-d_8 surface and were the average of at least 50 shots per data point. The peptide solution was injected directly to the buffer-solid interface, and SFG spectra were acquired immediately. Sample scans shown here are the average of at least 100 shots per data point (requiring ~60 min) collected using $s_{sfg}s_{vis}p_{ir}$ polarization combination (ssp), which probes the *yyz* component of $\chi^{(2)}$.

The effective surface nonlinear susceptibility was related to $\chi^{(2)}$, the surface nonlinear susceptibility, through the tensorial Fresnel coefficients:[22]

$$\chi_{eff}^{(2)} = \left[L(\omega_{SFG}) \cdot \hat{e}_{SFG} \right] \cdot \chi^{(2)} : \left[L(\omega_{VIS}) \cdot \hat{e}_{VIS} \right] \left[L(\omega_{IR}) \cdot \hat{e}_{IR} \right] \qquad (3.2)$$

where $\hat{e}_i$ is a unit polarization vector of the optical field at ω_i, and $L(\omega_i)$ is the tensorial Fresnel factor. The measured SFG spectra were fit to the equation ($\chi_{NR}^{(2)}, \omega_q, \Gamma_q$ and A_q are the fit parameters):

$$\left| \chi^{(2)} \right|^2 = \left| \chi_{NR}^{(2)} + \sum_q \frac{A_q}{\omega_{IR} - \omega_q + i\Gamma_q} \right|^2 \qquad (3.3)$$

where $\chi_{NR}^{(2)}$ is the nonresonant part of the surface nonlinear susceptibility, $\chi^{(2)}$, ω_{IR} is the frequency of the infrared beam, and ω_q and Γ_q are the frequency and damping constant of the q^{th} vibrational mode, respectively. The strength of a vibrational mode, $\mathbf{A}_q$, is given by:

$$A_q = N_s \int a_q^{(2)}(\Omega) f(\Omega) d\Omega \tag{3.4}$$

where N_s is the surface density of molecules, $\boldsymbol{a}_q$ is the oscillator strength of a single mode, and $f(\Omega)$ is an orientation distribution function over a set of orientational angles that describes a transformation between the laboratory and molecular coordinate system.[22] The amplitude $\boldsymbol{a}_q$ can be understood as:

$$a_q \propto \frac{\partial \vec{\mu}}{\partial Q_q} \otimes \frac{\partial \alpha^{(1)}}{\partial Q_q} \tag{3.5}$$

where $\partial\vec{\mu}/\partial Q_q$ and $\partial\alpha^{(1)}/\partial Q_q$ are the infrared dipole and Raman polarizability derivatives with respect to Q_q, the classical normal coordinate of the q^{th} vibrational mode.[22,23] These equations demonstrate that a vibrational resonance is SFG active when it is both IR and Raman active, and it must be ordered (i.e., a mode that has a random geometrical distribution does not produce a resonant response according to the integral in eq 3).[24,25] The physical interpretation of the SFG spectra presented here is: due to specific interactions between the peptide and the surface (i.e., hydrophobic or electrostatic), certain vibrational modes become ordered at an interface, and those modes are seen in the SFG spectra.

3.3. Results and Discussion

3.3.1. CD Measurements. CD spectra for the LK, AK, AR, and FR peptides are presented in Figure 3.2. The CD spectrum of LK_{14} shows that it has a predominantly α-helical structure in solution (strong residual ellipticity at 208 and 222 nm). The LK_7 α peptide shows partial helical content. All of the other peptides examined in this study had a random coil structure under the solution concentrations used here. The nominal chain length necessary for secondary structure formation is 4 residues for β-strand formation and 14 residues for α-helix formation.[8] Short peptides have many more degrees of conformational freedom than proteins, and it is unusual for a peptide to adopt a single predominant solution structure.[26] Degrado and Lear have shown that the LK_{14} peptide aggregates to form tetramers in solution, which stabilizes the helical structure. Their LK_7 β peptide showed secondary structure in Tris·HCl buffer, whereas we found random coil structure in PBS.[8] It has been shown that, for LK_{14} concentrations below 0.01 mM, the peptide is primarily a random coil.[8,27,28] It is possible that the critical concentration for secondary structure formation for the AK, AR, and FR peptides is higher than the concentrations used in this study.

3.3.2. QCM Measurements. QCM adsorption data were collected for the 14- and 7-amino acid peptides adsorbed onto PS and SiO_2 surfaces. The results summarized in Table 1 show the absolute magnitude of the change in frequency upon adsorption, $|\Delta f|$, normalized to the third overtone, the corresponding Sauerbrey mass, and the solution concentration used in the experiment. The tabulated $|\Delta f|$ data was measured from a single QCM experiment (instrument sensitivity = ± 0.3 Hz). QCM measurements were

obtained at least two times for each the peptides. The peptides all showed monotonic adsorption behavior on polystyrene. The LK_{14} peptide showed multistep adsorption on SiO_2, while the other peptides adsorbed monotonically.[20] It was observed that the least soluble peptides adsorbed the greatest peptide mass on polystyrene and likely have a stronger driving force for interaction with the hydrophobic surface. For example, FR_{14} of solubility ~100 μg/mL produced the largest change in frequency ($|\Delta f|$ = 12 Hz), while highly soluble AR_{14} (1.5 mg/mL) showed less adsorption ($|\Delta f|$ = 5 Hz). A direct comparison of the adsorbate concentration as a function of amino acid chain length is difficult due to the reduced solubility of the shorter-chain peptides. Where QCM experiments could be performed at identical concentration (i.e., AK_{14} and AK_7), it was observed that the longer 14-amino acid peptide adsorbed twice the mass of the 7-amino acid peptide ($|\Delta f|$ = 6 and $|\Delta f|$ = 3 Hz, respectively). All of the 14-amino acid peptides

Table 3.1: QCM Results: Frequency Change and Mass Adsorbed on Polystyrene and Silica

	PS		SiO_2		
peptide	$\lvert\Delta f\rvert$ (Hz)	mass (ng/cm^{-2})	$\lvert\Delta f\rvert$ (Hz)	mass (ng/cm^{-2})	solution concentration (mg/mL)
LK_{14}	8	140	16	280[a]	1.0
AK_{14}	5	90	9	160	1.0
AR_{14}	8	140	13	230	1.5
FR_{14}	15	270	12	210	0.1
LK_7	1	20	0.5	10	0.1
AK_7	3	50	2	40	1.0
AR_7	6	100	12	200	1.0
FR_7	5	90	2	90	0.05

[a] *Sauerbrey mass underestimates actual adsorbed mass here.*[19,20]

adsorbed on SiO_2, but of the 7-amino acid peptides, only AR_7 showed significant adsorption.

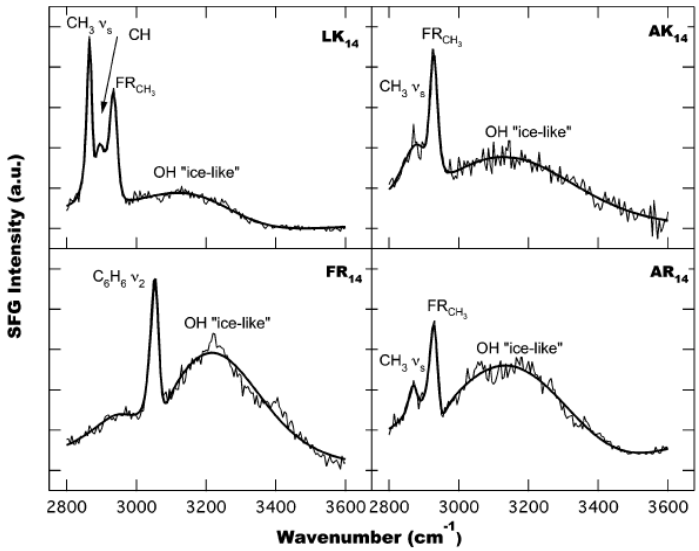

Figure 3.3 *SFG spectra of LK_{14}, AK_{14}, AR_{14}, and FR_{14} (clockwise from top left) on PS-d_8. The LK_{14} peptide shows three distinct modes associated with the leucine side chain: 2870 cm^{-1}, assigned to CH_3 υ_s, 2895 cm^{-1}, assigned to a CH stretch or CH_2 F.R., and 2935 cm^{-1}, assigned to CH_3 F.R. The AR_{14} and AK_{14} peptides show two distinct modes associated with the alanine side chain: 2870 cm^{-1}, assigned to CH_3 υ_s, and a mode around 2930 cm^{-1}, assigned to CH_3 F.R. The FR_{14} peptide shows a mode at 3050 cm^{-1}, assigned to the υ_2 phenyl ring stretch of the phenylalanine side chain.*

3.3.3. SFG Adsorption Studies.

3.3.3.1. Adsorption Studies on Polystyrene. To investigate the effects of side chain character on adsorption, we have studied amphiphilic peptides with a range of nonpolar side chain hydrophobicities: alanine, phenylalanine, and leucine. The SFG spectra of the 14-amino acid peptides adsorbed on deuterated polystyrene are shown in Figure 3.3. The solid lines in each figure are the results of fitting the spectra to eq. 3.3, where the intensity units are arbitrary and different for each peptide. Peptide modes are visible for

all of the peptides adsorbed on hydrophobic polystyrene surfaces. As we have previously demonstrated, LK_{14} shows three distinct modes on PS-d_8: 2870 cm^{-1}, assigned to a methyl symmetric stretch, 2895 cm^{-1}, assigned to a CH stretch or CH_2 Fermi resonance, and 2935 cm^{-1}, assigned to a Fermi resonance of a methyl mode.[20] The AK_{14} shows similar results: 2870 cm^{-1}, assigned to symmetric stretch of the methyl side chain of alanine, and the 2925 cm^{-1} mode, assigned to a Fermi resonance of the methyl side chain of alanine. The SFG spectrum of the AR_{14} peptide is similar to AK_{14}, with the two modes observed at 2870 and 2930 cm^{-1}. The FR_{14} peptide shows a strong resonance at 3050 cm^{-1}, assigned to the symmetric phenyl stretch, υ_2, of the phenylalanine side chains. This is in contrast to Kim et al., who observed two CH_2 modes at 2855 and 2935 cm^{-1} for phenylalanine amino acid adsorbed on a glassy carbon electrode.[29] This is likely due to the fact that the electric field present at an electrode induces a different molecular orientation of the adsorbate than an uncharged hydrophobic surface does.

The spectral results observed here are very similar to the previous results of SFG investigations of several amino acids at the oil-water[30] and air-water[31] interface. This demonstrates that these 14-amino acid peptides show SFG spectra characteristic of their hydrophobic amino acid side chains. The amphiphilic nature of these peptides may allow for the hydrophobic side chains to interact with hydrophobic polystyrene surface, while the charged hydrophilic chains face the bulk water interface. The adsorption of the 14-amino acid peptides on polystyrene seems to be controlled by the hydrophobic character of the side chains and shows a spectroscopic signature for the alanine, leucine, and phenyalanine side chains. The 7-amino acid peptides show the same trend for LK and FR peptides. The SFG spectra of the 7-amino acid (β-strand sequences) peptides adsorbed on

polystyrene are shown in Figure 3.4. The SFG spectrum of LK_7 shows three resonances: 2870 cm^{-1}, again a symmetric stretch of a methyl group, 2910 cm^{-1}, CH stretch or CH_2 Fermi resonance, and 2935 cm^{-1}, a methyl Fermi resonance. A peak at 3050 cm^{-1} in the SFG spectrum in FR_7 is attributed to the symmetric ring stretch, υ_2, of phenylalanine. In contrast, there are no peptide and little hydrogen-bonded water modes visible in the SFG spectrum of AK_7. The SFG spectrum of AR_7 does not show modes associated with

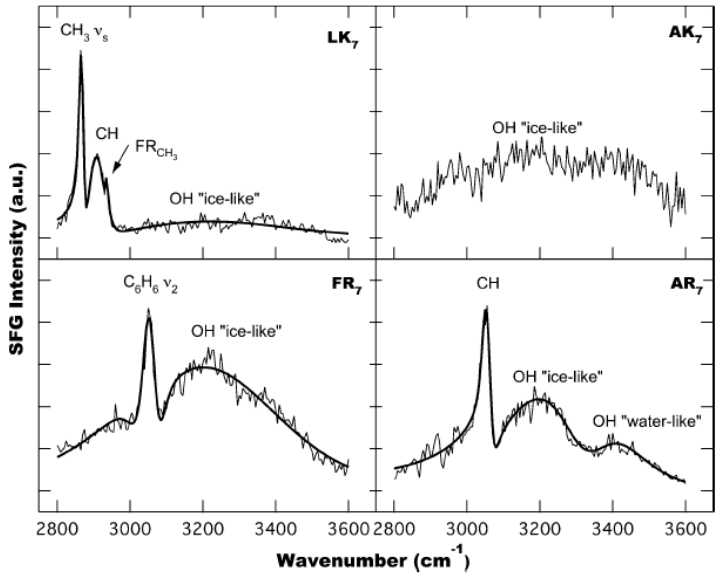

Figure 3.4 *SFG spectra of LK_7, AK_7, AR_7, and FR_7 (clockwise from top left) on PS-d_8. The LK_7 spectra was fit with three resonances: 2870 cm^{-1}, assigned to CH_3 υ_s, 2910 cm^{-1}, assigned to a CH stretch or CH_2 F.R., and 2935 cm^{-1}, assigned to CH_3 F.R. The AK_7 peptide shows no modes associated with the peptide. The AR_7 peptide shows a mode at 3030 cm^{-1}, assigned to a CH mode of the arginine side chain. The FR_7 peptide shows a mode at 3050 cm^{-1}, assigned to the υ_2 phenyl ring stretch of the phenylalanine side chains. Comparison of Figures 3.3 and 3.4 shows that the molecular orientation of alanine is more sensitive to sequence and chain length than leucine or phenylalanine.*

alanine, but a strong CH stretching mode at 3030 cm^{-1}. Previous work of Larsson has assigned a CH mode at 3030 cm^{-1} to the arginine side chain.[32,33]

To directly compare the effects of peptide sequence, a 7-amino acid peptide with identical amino acid composition to LK_7 was synthesized. The peptide had a sequence Ac-LKKLLKL-NH_2 (LK_7 α) and was designed to form a helical structure at an apolar interface (compared to the LK_7 β with sequence LKLKLKL). The LK_7 α and LK_7 β peptides produce slightly different SFG spectra on PS-d_8. Figure 3.5 shows the SFG spectra of the two 7-amino acid LK peptides with α and β sequences. The LK_7 α and LK_7 β spectra have three similar modes: 2870 cm^{-1}, assigned to the symmetric stretch of the methyl groups in the leucine side-chains, 2898 cm^{-1}, CH resonance or CH_2 Fermi resonance, and 2935 cm^{-1}, a Fermi resonance of a methyl group. The subtle differences in the relative intensity of the three CH modes observed in the SFG spectra indicate a slightly different average orientation of the methyl groups at the PS-d_8 surface. Another slight difference in the spectra is in the water arrangement at the interface: there is almost no structured water in the spectrum of LK_7 β, whereas the water peak centered at 3150 cm^{-1} for LK_7 α is similar to the peak in the spectrum of LK_{14} on PS-d_8. A comparison between the LK_{14}, LK_7 β, and LK_7 α peptides on PS-d_8 demonstrates the importance of peptide length and sequence in its adsorption properties. The LK_{14} is twice the length of the LK_7 α. This difference in length causes different ordering of leucine moieties at the hydrophobic PS-d_8 interface. Conversely, LK_7 α and LK_7 β have different sequences but similar length and molecular weight. The similarities in the SFG signal between the LK_7 α and LK_7 β suggest that the influence of sequence on adsorption is smaller than that of chain length.

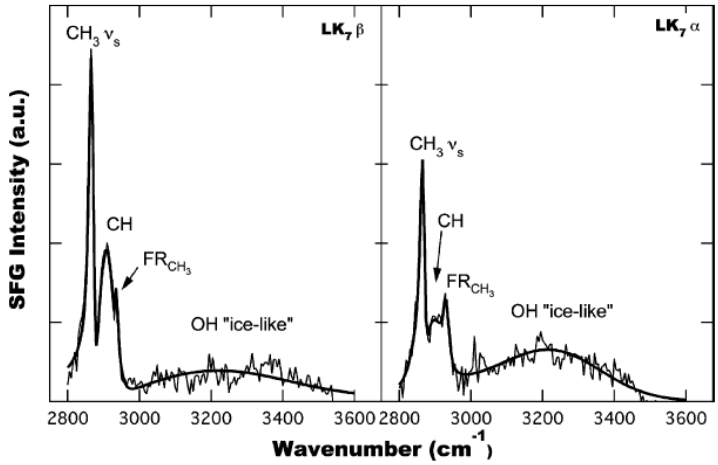

Figure 3.5 *Comparison of the effect of sequence on the SFG spectra observed for the β-strand sequence, LK_7 β (LKLKLKL) (left) vs the α-helical sequence peptide, LK_7 α (LKKLLKL) (right). Qualitatively similar spectra are observed, with modes in both peptides are assigned to: 2870 cm^{-1}, CH_3 υ_s, 2900 cm^{-1}, CH stretch or CH_2 F.R., and 2930 cm^{-1}, CH_3 F.R.*

The effect of chain length is also observed in the case of the AR and AK peptides. In the case of AR_{14} and AR_7 peptides, drastically different SFG spectra are observed at the polystyrene interface. AK_{14} shows a very similar spectrum to AR_{14}, whereas the AK_7 shows no SFG signal on PS-d_8. The similarities in the CH modes observed for both AK_{14} and AR_{14} imply that the SFG spectra observed are characteristic of the hydrophobic alanine side chain and not governed by the hydrophilic residues (R or K). The frequencies of the resonances (2870 and 2930 cm^{-1} of AK_{14} and AR_{14}) are similar to that observed by Kim et al., who studied polyalanine at the air-water interface and observed two modes of similar relative intensity at 2878 and 2942 cm^{-1}, respectively.[34]

In addition to CH resonances from the peptides, we observed a large peak centered at 3200 cm^{-1} and a weaker peak at 3400 cm^{-1} from hydrogen-bonded water molecules at the liquid-polystyrene interface. These water OH modes have been assigned to tetrahedrally coordinated ("icelike") and hydrogen-bonded ("liquidlike"), respectively.[13,35,36] The polystyrene surface is sensitive to contamination, so differences in the OH region of the peptide SFG spectra may be due to differences in sample impurities as well as adsorbed peptide structure.[37] However, the arginine-containing peptides always show more intensity than the lysine-containing peptides in the 3200 cm^{-1} mode, which may be attributed to differences in the side chain acidities of lysine (pK_a = 10.8) and arginine (pK_a = 12.5).

Some interesting trends become apparent when considering all of the data. The FR peptides (FR_{14} and FR_7), which are the least soluble, show no difference in interfacial SFG signal upon adsorption. The LK peptides, the next least soluble, show very little differences between the 14- and 7-amino acid peptides and even less between the LK_7 β and LK_7 α peptides. The alanine peptides, AK and AR, are readily soluble and show large differences in spectra of the 14- and 7-amino acid peptides. In summary, the less-soluble LK and FR peptides show alignment of the nonpolar side chains of the peptide on hydrophobic surfaces that are largely independent of chain length and sequence, while the adsorbed orientation of the relatively soluble AK and AR peptides is affected more by variables such as the amino acid sequence and chain length. This trend correlates with the nonpolar nature of the amino acids alanine, leucine, and phenylalanine.

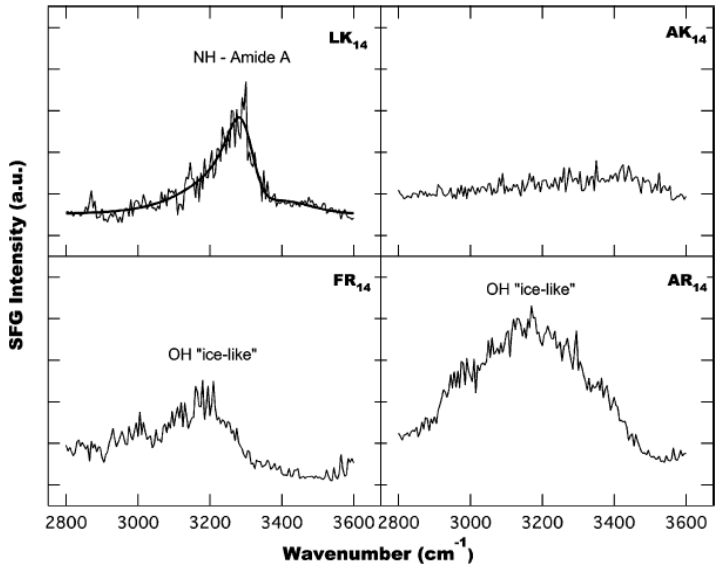

Figure 3.6 *SFG spectra of LK_{14}, AK_{14}, AR_{14}, and FR_{14} (clockwise from top left) on SiO_2. The peak centered at 3300 cm^{-1} in the LK_{14} spectrum is assigned to an amide A N-H stretching mode.*

3.3.3.2. Adsorption Studies on Silica.

The SFG spectra for the LK, AK, AR, and FR peptides adsorbed on SiO_2 are plotted in Figure 3.6. The SFG spectrum of LK_{14} on SiO_2 is the only spectrum that yields an NH mode (at 3300 cm^{-1}). The spectra of AK_{14}, AR_{14}, and FR_{14} only result in OH modes present upon adsorption, similar to the studies of BSA on silica.[38] QCM data confirms that the 14-amino acid peptides all adsorb onto SiO_2 (Table 1). These peptides are random coil in solution and do not produce a net orientation upon adsorption required to produce SFG active peptide modes. The results presented in this work (alignment of the hydrophobic residues at a hydrophobic surface and lack of alignment of any peptide modes at a hydrophilic interface) are in agreement with previous SFG studies of proteins.[25,39]

The 7-amino acid peptides do not generate a SFG signal due to the peptide (data not shown). The QCM data shows weak but measurable adsorption for LK_7, AK_7, and FR_7 peptides on SiO_2. LK_7 and FR_7 have very low solubility, which may contribute to weak adsorption. AK_7 is highly soluble, but shows a low affinity for the SiO_2 surface. QCM data for AR_7 shows a large adsorbed mass, but no SFG signal is detected on SiO_2, indicating a lack of a specific orientation of SFG active vibrational modes at the surface.

The NH stretch on SiO_2 observed following LK_{14} adsorption is assigned to the amide A mode of the peptide backbone. This mode has been previously been observed in SFG studies of helical peptides and proteins.[15,16,40,41] CD data for LK_{14} peptide indicate that this peptide is α-helical in solution. The presence of this backbone mode suggests that LK_{14} maintains its solution-phase helical structure to some degree upon adsorption and demonstrates that the SFG spectra of peptides on silica are sensitive to molecular-scale peptide secondary structure adsorption.

3.4. Conclusions

We have observed similar spectroscopic results for adsorption of model amphiphilic peptides on PS that are independent of the secondary structure of the polypeptide backbone. The amino acids of these peptides were found to act as individual chromophores and produce unique SFG signatures when adsorbed on hydrophobic polystyrene surfaces. For example, LK_{14}, LK_7 β, and LK_7 α show similar SFG spectra due to ordering of leucine side chains at the polystyrene surface. The SFG spectra of peptides containing alanine amino acid are more sensitive to changes in chain length and sequence. The forces driving surface orientation at the hydrophobic polystyrene surface

appear to be local hydrophobic interactions and are determined primarily by the properties of the peptide amino acid side chains.

SFG spectra of LK, AK, AR, and FR peptides adsorbed on SiO_2 do not show vibrational modes associated with the peptides, except for an amide A (NH mode at 3300 cm^{-1}) observed following LK_{14} adsorption. CD studies show that only LK_{14} peptide has predominantly α-helical conformation in solution. The amide A band observed in the SFG spectrum indicates that we measure a molecular scale secondary structure interaction with the silica surface in contrast to the local interaction measured for adsorbed peptides on polystyrene.

References

(1) Kasemo, B. *Surface Science* **2002**, *500*, 656-677.

(2) Ratner, B. D. *Journal of Molecular Recognition* **1996**, *9*, 617-625.

(3) Gopel, W. *Biosensors and Bioelectronics* **1998**, *13*, 723-728.

(4) *Proteins at Interfaces II: Fundamentals and Applications*; Horbett, T. A.; Brash, J. L., Eds.; American Chemical Society: Washington D. C., 1995.

(5) Kasemo, B. *Current Opinion in Solid State and Materials Science* **1998**, *3*, 451-459.

(6) Castner, D. G.; Ratner, B. D. *Surface Science* **2002**, *500*, 28-60.

(7) Mermut, O.; York, R. L.; Phillips, D. C.; McCrea, K. R.; Ward, R. S.; Somorjai, G. A. *Biointerphases* **2006**, *1*, P5-P11.

(8) Degrado, W. F.; Lear, J. D. *Journal of the American Chemical Society* **1985**, *107*, 7684-7689.

(9) Ringstad, L.; Schmidtchen, A.; Malmsten, M. *Langmuir* **2006**, *22*, 5042-5050.

(10) Singh, N.; Husson, S. M. *Langmuir* **2006**, *22*, 8443-8451.

(11) Kim, J.; Somorjai, G. A. *Journal of the American Chemical Society* **2003**, *125*, 3150-3158.

(12) Chen, X. Y.; Clarke, M. L.; Wang, J.; Chen, Z. *International Journal of Modern Physics B* **2005**, *19*, 691-713.

(13) Shen, Y. R.; Ostroverkhov, V. *Chemical Reviews* **2006**, *106*, 1140-1154.

(14) Degrado, W. F.; Wasserman, Z. R.; Lear, J. D. *Science* **1989**, *243*, 622-628.

(15) Wang, J.; Chen, X. Y.; Clarke, M. L.; Chen, Z. *Journal of Physical Chemistry B* **2006**, *110*, 5017-5024.

(16) Clarke, M. L.; Wang, J.; Chen, Z. *Journal of Physical Chemistry B* **2005**, *109*, 22027-22035.

(17) King, D. S.; Fields, C. G.; Fields, G. B. *International Journal of Peptide and Protein Research* **1990**, *36*, 255-266.

(18) Sauerbrey, G. *Zeitschrift fuer Physik* **1959**, *155*, 206-222.

(19) Hook, F.; Rodahl, M.; Brzezinski, P.; Kasemo, B. *Langmuir* **1998**, *14*, 729-734.

(20) Mermut, O.; Phillips, D. C.; York, R. L.; McCrea, K. R.; Ward, R. S.; Somorjai, G. A. *Journal of the American Chemical Society* **2006**, *128*, 3598-3607.

(21) Westerberg, S.; Wang, C.; Chou, K.; Somorjai, G. A. *Journal of Physical Chemistry B* **2004**, *108*, 6374-6380.

(22) Wei, X.; Hong, S. C.; Zhuang, X. W.; Goto, T.; Shen, Y. R. *Physical Review E* **2000**, *62*, 5160-5172.

(23) Superfine, R.; Huang, J. Y.; Shen, Y. R. *Chemical Physics Letters* **1990**, *172*.

(24) Doyle, A. W.; Fick, J.; Himmelhaus, M.; Eck, W.; Graziani, I.; Prudovsky, I.; Grunze, M.; Maciag, T.; Neivandt, D. J. *Langmuir* **2004**, *20*, 8961-8965.

(25) Wang, J.; Buck, S. M.; Chen, Z. *Journal of Physical Chemistry B* **2002**, *106*, 11666-11672.

(26) Marqusee, S.; Baldwin, R. L. *Proceedings of the National Academy of Sciences of the United States of America* **1987**, *84*, 8898-8902.

(27) Dieudonné, D.; Gericke, A.; Flach, C. R.; Jiang, X.; Farid, R. S.; Mendelsohn, R. *Journal of the American Chemical Society* **1998**, *120*, 792-799.

(28) Long, J. R.; Oyler, N.; Drobny, G. P.; Stayton, P. S. *Journal of the American Chemical Society* **2002**, *124*, 6297-6303.

(29) Kim, J.; Chou, K. C.; Somorjai, G. A. *Journal of Physical Chemistry B* **2002**, *106*, 9198-9200.

(30) Watry, M. R.; Richmond, G. L. *Journal of Physical Chemistry B* **2002**, *106*, 12517-12523.

(31) Ji, N.; Shen, Y. R. *Journal of Chemical Physics* **2004**, *120*, 7107-7112.

(32) Larsson, L. *Acta Chem. Scand.* **1950**, *4*, 27.

(33) Garfinkel, D. *Journal of the American Chemical Society* **1958**, *80*.

(34) Kim, G.; Gurau, M.; Kim, J.; Cremer, P. S. *Langmuir* **2002**, *18*, 2807-2811.

(35) Du, Q.; Freysz, E.; Shen, Y. R. *Science* **1994**, *264*, 826-828.

(36) Scatena, L. F.; Richmond, G. L. *Chemical Physics Letters* **2004**, *383*, 491-495.

(37) Seo, Y. S.; Satija, S. *Langmuir* **2006**, *22*, 7113-7116.

(38) Kim, J.; Cremer, P. S. *ChemPhysChem* **2001**, *2*, 543-546.

(39) Wang, J.; Buck, S. M.; Even, M. A.; Chen, Z. *Journal of the American Chemical Society* **2002**, *124*, 13302-13305.

(40) Jung, S. Y.; Lim, S. M.; Albertorio, F.; Kim, G.; Gurau, M. C.; Yang, R. D.; Holden, M. A.; Cremer, P. S. *Journal of the American Chemical Society* **2003**, *125*, 12782-12786.

(41) Knoesen, A.; Pakalnis, S.; Wang, M.; Wise, W. D.; Lee, N.; Frank, C. W. *IEEE Journal of Selected Topics in Quantum Electronics* **2004**, *10*, 1154-1163.

Chapter 4

The Influence of Ionic Strength on the Adsorption of a Model Peptide on Hydrophilic Silica and Hydrophobic Polystyrene Surfaces: Insights from SFG Vibrational Spectroscopy

Sum frequency generation (SFG) vibrational spectroscopy has been used to study the influence of ionic strength of a solution on the interfacial structure of a model amphiphilic peptide. The ionic strength of the solution is controlled by changing the salt concentration of the solution. This peptide (called LK_{14}) contains fourteen amino acids and is composed of hydrophobic leucine (L) and hydrophilic lysine (K) residues. LK_{14} is shown to be an alpha helix in solution at high ionic strength and a random coil at low ionic strength. On a hydrophilic silica surface, an N-H mode from LK_{14} is observed at high ionic strength that is no longer observed when the peptide is adsorbed at low ionic strengths. Instead, strong interfacial water signal is measured at low ionic strength conditions. The N-H mode that appears at high salt concentrations is only seen when the peptide has a stable secondary structure. On a hydrophobic polystyrene surface, C-H modes are observed that are independent of the ionic strength of the solution. However, the intensity of the water modes observed upon peptide adsorption increases with decreasing ionic strength. In contrast, in the absence of peptide (i.e. the polystyrene/buffer interface), there is no change in the intensity of the water modes with changing ionic strength. This implies that C-H modes observed on hydrophobic surfaces in peptide SFG studies are independent of the secondary structure of the biomolecule in

solution, and that the adsorption of a peptide can induce ordering of interfacial water molecules.

4.1 Introduction

Through his understanding of non-linear optical processes, Professor Eisenthal has inspired a generation of surface scientists. Among his many accomplishments, the 1992 study[1] with Ong and Zhao that related the interfacial potential of the silica-water interface to the second harmonic signal holds special significance. In this study, we examine how changing the ionic strength (and hence interfacial potential) of a solution influences the interfacial structure of an adsorbed peptide at both hydrophobic and hydrophilic surfaces.

The study of how biological molecules adsorb onto surfaces is an active area of research.[2] Understanding how proteins adsorb onto surfaces hold particular interest for the rational design of biomedical implants.[3] Our experimental[4] and philosophical[5] approach to understanding this problem has recently been published and involves the adsorption of model peptides of varying chain length on hydrophobic and hydrophilic surfaces. In this chapter, we extend our earlier study of a model amphiphilic LK_{14} peptide (where L = leucine and K = lysine) to understand how the ionic strength of the solution influences the solution and interfacial structure. The solution and interfacial structure were monitored by Circular Dichroism (CD) and Sum Frequency Generation (SFG) Vibrational Spectroscopy, respectively. The LK_{14} peptide was first synthesized by Degrado and Lear, who showed that the LK_{14} was an alpha helix under certain solvent conditions.[6] Degrado and Lear also characterized the structure of this peptide at the apolar/water interface.[6] Since then, there have been several studies of the interfacial structure of this peptide.[7] Recently, we have characterized the interfacial structure of LK_{14} peptide at hydrophobic polystyrene/water and hydrophilic silica/water interfaces

using SFG, Atomic Force Microscopy (AFM) and Quartz Crystal Microbalance (QCM).[4] In this work, we will demonstrate how changing the ionic strength of the solution can influence both the solution structure (monitored by CD) and the interfacial structure of a peptide at surface (monitored by SFG).

4.2 Experimental

Details about peptide synthesis, and other experimental details, can be found elsewhere.[4] The sequence of the peptide studied here is Ac-LKKLLKLLKKLLKL-NH_2.

4.2.1 Substrate Preparation

Fused quartz windows (Esco Products) were cleaned by soaking in NOCHROMIX (Godax Laboratories) solution and rinsing with deionized water. Polystyrene thin films (200 nm) were prepared by spin-casting (Specialty Coating Systems, P-6000) a 3 wt% solution of deuterated polystyrene (PS-d_8, 255K MW, Polymer Source, Inc., Montreal, Canada) in toluene onto the fused silica windows and annealing at 110 °C for 12 hours. Deuterated polystyrene was used in this study to avoid spectral confusion between the polymer surface and the adsorbed peptide.

Phosphate Buffered Saline (PBS) was obtained from Sigma-Aldrich (Cat. No. P-5368). A solution was prepared by dissolving 1 packet of PBS salt into 1 liter of ultrapure water (Millipore, Milli-Q water with at least 18 MΩ·cm resistivity). This made a solution of 0.01 M phosphate buffered saline, 0.138 M NaCl, and 0.0027 M KCl. This solution had a pH of 7.4. We refer to this solution as 1X PBS buffer. The 10X PBS buffer was prepared by dissolving a packet of PBS salt into 100 mL. Serial dilution of the 1X PBS buffer was used to create solutions of lower ionic strengths (0.1X PBS buffer, 0.05X PBS

buffer, 0.01X PBS buffer, 0.001X PBS buffer, and 0.0001X PBS buffer). Table 4.1 summarizes the ionic strength of the solutions used in this study.

Name	Concentration of phosphate buffered saline (M)	Concentration of Sodium Chloride (M)	Concentration of Potassium Chloride (M)
10X	0.1	1.38	0.027
1X	0.01	0.138	0.0027
0.1X	0.001	0.0138	0.00027
0.05X	0.0005	0.0069	0.000135
0.01X	0.0001	0.00138	0.000027

Table 4.1. *The names and ionic strengths of solutions used in these experiments.*

4.2.2 Circular Dichroism

CD measurements were carried out on an Aviv 62DS spectrometer. The CD was monitored in 1 nm steps from 190 nm to 240 nm, averaging each point for at least one second. CD studies were performed using 0.1 mg/mL solution of peptide in a 1-mm strain-free (Aviv) cuvette. The high ionic strength solutions, 1X PBS buffer and 10X PBS buffer, showed strong adsorption below 200 nm. Therefore, the 1X PBS buffer and 10X PBS buffer are only shown above 195 nm and 200 nm, respectively.

4.2.3 SFG Vibrational Spectroscopy

SFG spectra were obtained using a mode-locked Nd:YAG laser (Leopard D-20, Continuum, Santa Clara, CA). The 1064 nm light (20 ps pulse width, 20 Hz repetition rate) was sent to an optical parametric generator/amplifier (OPG/OPA) stage (LaserVision, Bellevue, WA) described previously.[8] The tunable infrared beam and the 532 nm visible beam were combined at the sample interface at incident angles of ca. 64 and 57 degrees, respectively, with respect to the surface normal. The SFG signal generated from the sample was collected by a photomultiplier tube, sent to a gated

integrator, and stored digitally. For each scan, data was collected with 200 shots/data point in 5 cm^{-1} increments in the 2800 -3600 cm^{-1} range. SFG measurements were typically repeated at least two times for each presented spectra. All spectra presented here are in the *ssp* polarization combination.

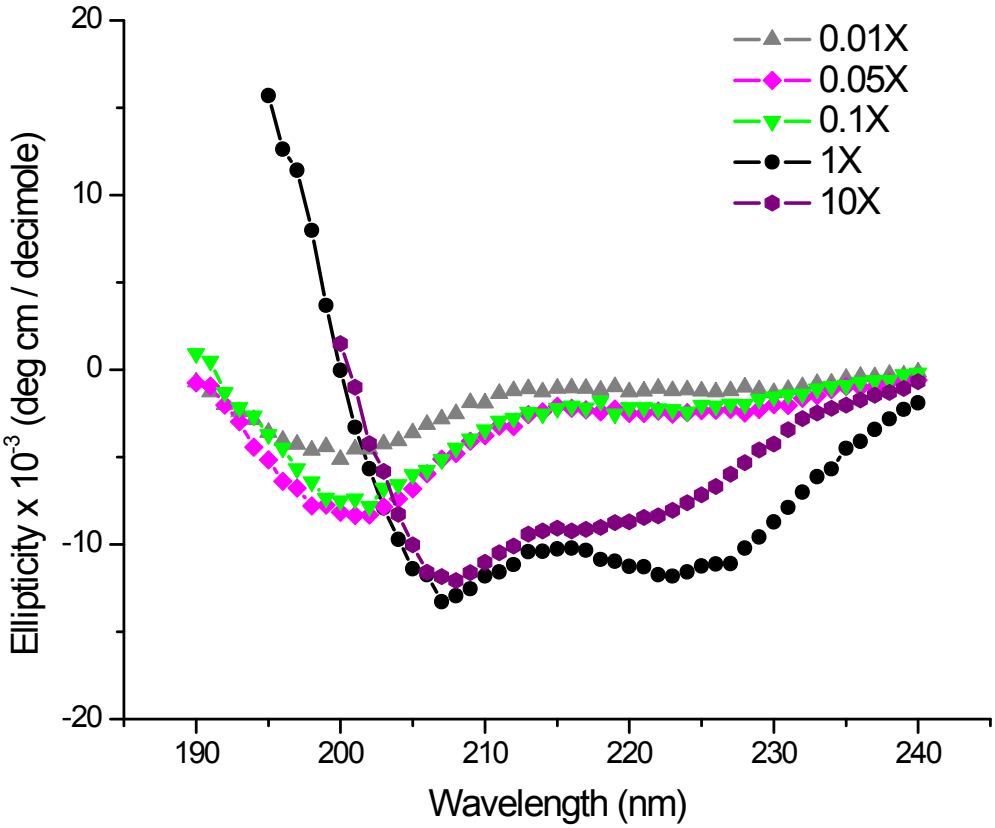

Figure 4.1. *CD Spectra of 0.1 mg/mL LK_{14} peptide. The 1X and 10X PBS Buffer show characteristic α-helical absorption at 208 nm and 222 nm. The LK_{14} peptide is a random coil when dissolved in solutions of lower ionic strength, as demonstrated by the CD spectra.*

The theory of sum frequency generation has been presented elsewhere[4,9-11]. Our spectra are fit to the equation:

$$\left|\chi^{(2)}\right|^2 = \left|\chi_{NR}^{(2)} + \sum_q \frac{A_q}{\omega_{IR} - \omega_q + i\Gamma_q}\right|^2, \quad (1)$$

where $\chi_{NR}^{(2)}$ is the non-resonant part of the surface nonlinear susceptibility, $\chi^{(2)}$; ω_{IR} is the frequency of the infrared beam; and ω_q and Γ_q are the frequency and damping constant of the q^{th} vibrational mode, respectively. The strength of a vibrational mode, $\mathbf{A}_q$, is given by:

$$A_q = N_s \int a^{(2)}(\Omega) f(\Omega) d\Omega, \quad (2)$$

where N_s is the surface density of molecules, $\mathbf{a}_q$ is the amplitude of a molecular vibration, $f(\Omega)$ is an orientation distribution function over Ω, a set of orientational angles that describes a transformation between the laboratory and molecular coordinate system. $\mathbf{a}_q$ can be understood has:

$$\mathbf{a}_q \propto \frac{\partial \vec{\mu}}{\partial Q_q} \otimes \frac{\partial \alpha^{(1)}}{\partial Q_q}, \quad (3)$$

where $\partial\vec{\mu}/\partial Q_q$ and $\partial\alpha^{(1)}/\partial Q_q$ are the infrared dipole derivative and Raman polarizability derivative with respect to Q_q, the classical normal coordinate of the q^{th} vibrational mode, respectively. The previous equations show what modes are measured in a sum frequency experiment: a mode must be IR and Raman active, and it must be ordered (i.e. a mode which has a random geometrical distribution does not produce a resonant response, as seen by the integral in eq. 2). Thus the physical interpretation of the SFG spectra presented here becomes clear: due to specific interactions between the peptide and surface (i.e. hydrophobic or electrostatic) certain vibrational modes will become ordered at an interface, and those modes are seen in the SFG spectra.

4.3 Results

4.3.1 Circular Dichroism of LK_{14} in solution as a function of ionic strength

The CD spectrum of 0.1 mg/mL LK_{14} is presented as a function of ionic strength in Figure 4.1. When dissolved in the 1X PBS buffer and 10X PBS buffer LK_{14} shows that it has a predominantly α-helical structure in solution, with the characteristic features for α-helicility at 208 and 222 nm. The same peptide dissolved in the the 0.1X PBS buffer, 0.05X PBS buffer, and 0.01X PBS buffer show a CD spectra typical of a random coil This is in qualitative agreement with Degrado and Lear, who showed that the α-helical

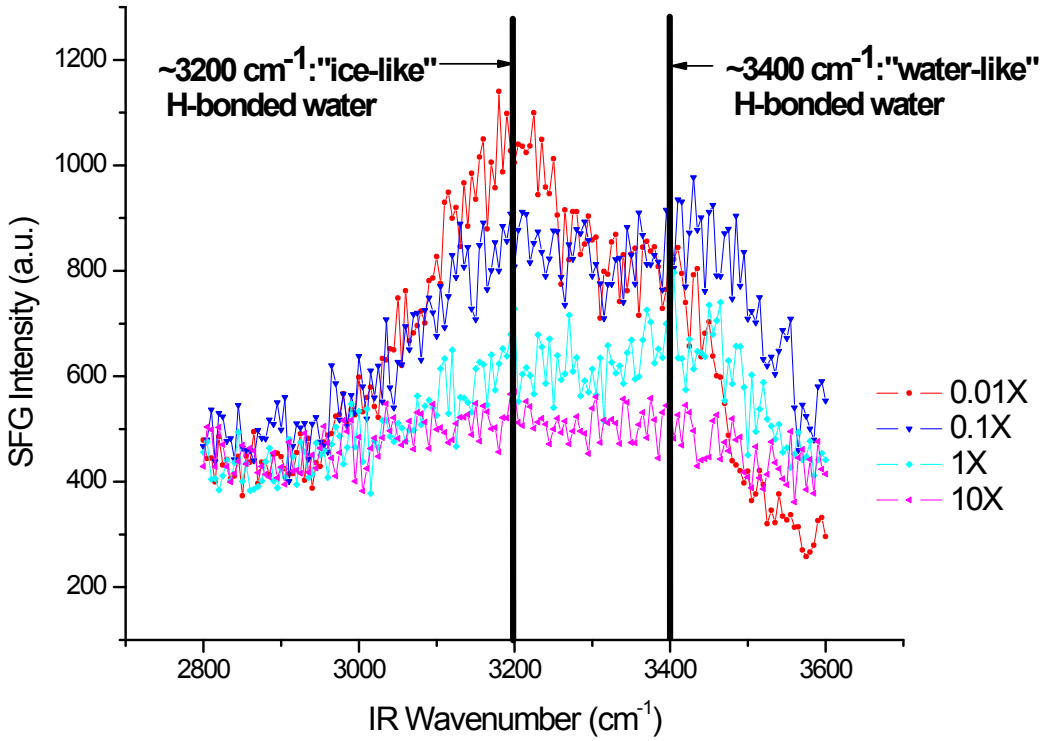

Figure 4.2. *SFG spectra of the silica/buffer interface. The modes observed are 3200 cm^{-1} and 3400 cm-1, both attributed to interfacial hydrogen bonded water.*

a)

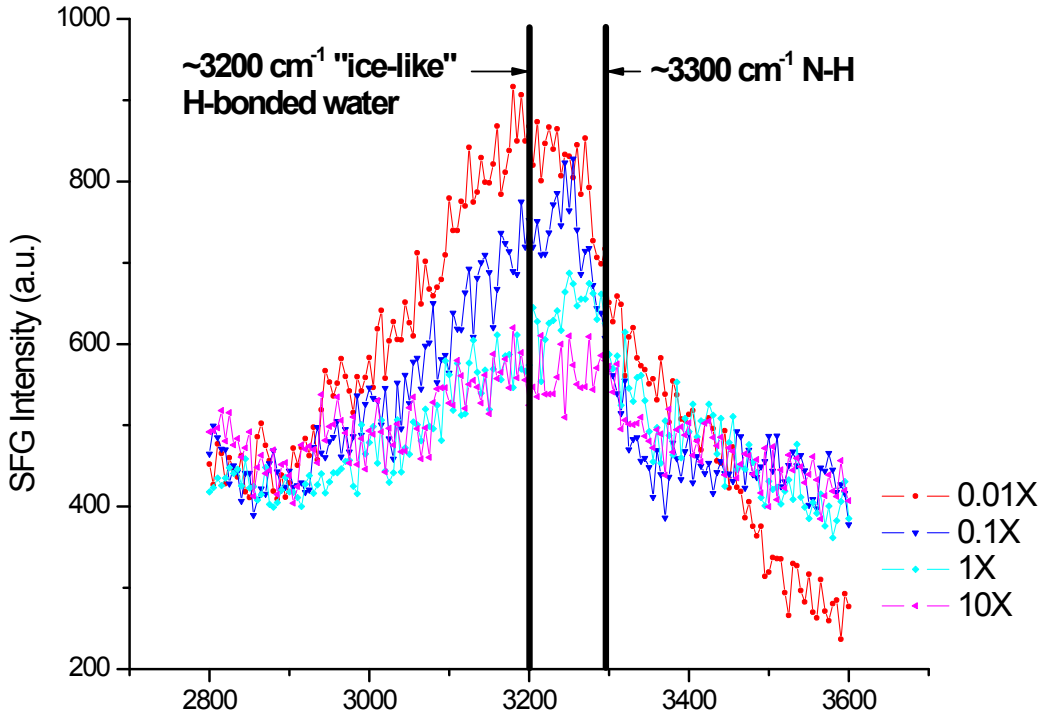
~3200 cm-1 "ice-like"
H-bonded water
~3300 cm-1 N-H
SFG Intensity (a.u.)
IR Wavenumber (cm-1)
0.01X
0.1X
1X
10X

b)

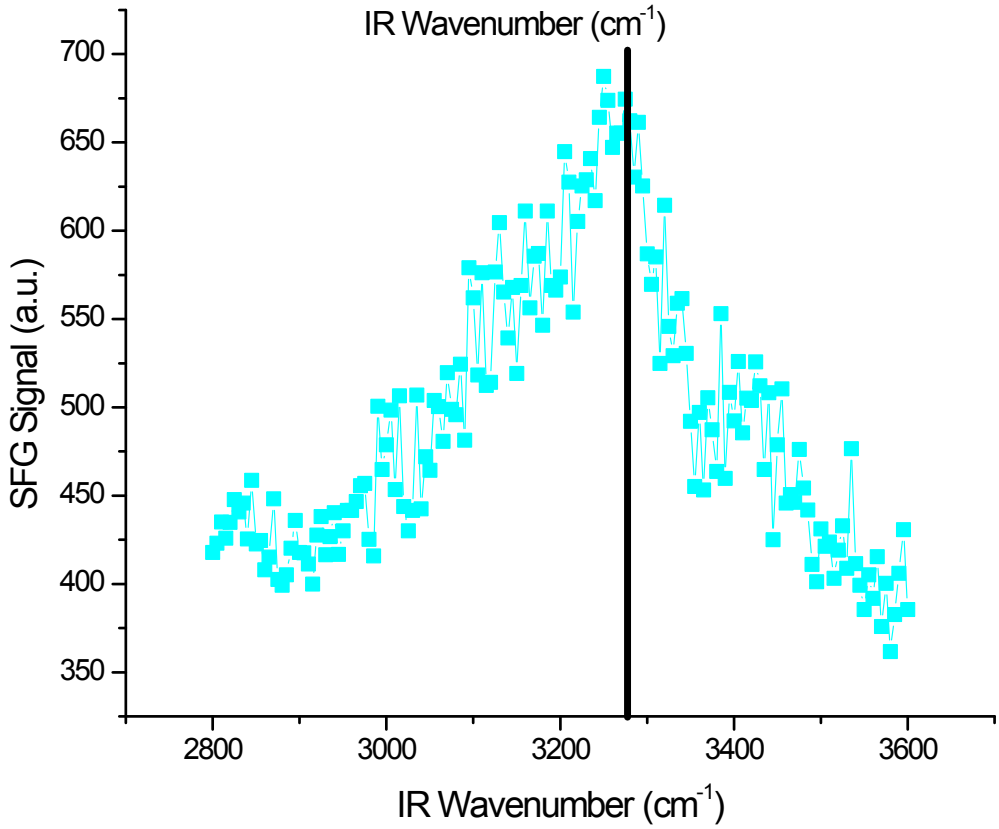
SFG Signal (a.u.)
IR Wavenumber (cm-1)

Figure 4.3. *a) SFG spectra of the 0.1 mg/mL LK_{14} at the silica/buffer interface as a function of ionic strength. These spectra show a NH mode at high ionic strengths. This mode is not observed in the low ionic strength solutions. b) The 1X PBS buffer spectrum from part a plotted by itself.*

propensity of this peptide is dependent on the peptide and chloride concentration in solution.[6]

4.3.2 Sum Frequency Generation Vibrational Spectroscopy of LK_{14} adsorption on silica and PS-d_8 surfaces at different ionic strengths

The SFG spectra from the hydrophilic silica/buffer interface as a function of the ionic strength is presented in Figure 4.2. The spectra show interfacial water modes at ~3200 cm^{-1} and ~3400 cm^{-1} at low ionic strengths. These modes are attributed to tetrahedredrally coordinated hydrogen bonded water (ice-like) and less than tetrahedrally coordinated hydrogen bonded water (liquid-like), respectively.[12] At higher ionic strengths the intensity of both modes decreases. This behavior is similar to what has been observed previously by Ong et. al., who looked at the second harmonic signal of the silica/water interface as a function of electrolyte concentration.[1] The 10X PBS buffer/silica interface shows relatively little SFG signal; however, some intensity from both O-H modes in the region between ~3200 cm^{-1} and 3400 cm^{-1} is observed. The SFG spectra of 0.1 mg/mL LK_{14} peptide adsorbed on SiO_2 from different concentrations of PBS solution are shown in Figure 4.3. We have previously reported that an N-H mode attributed to the adsorbed peptide is present at ~3300 cm^{-1} in the 1X PBS Solution.[4] Using a 10 fold higher concentration of PBS gives a similar SFG spectrum, with the N-H intensity of the ~3300

cm^{-1} mode of the peptide decreasing only slightly relative to the 1X PBS spectrum. At the 0.01X PBS

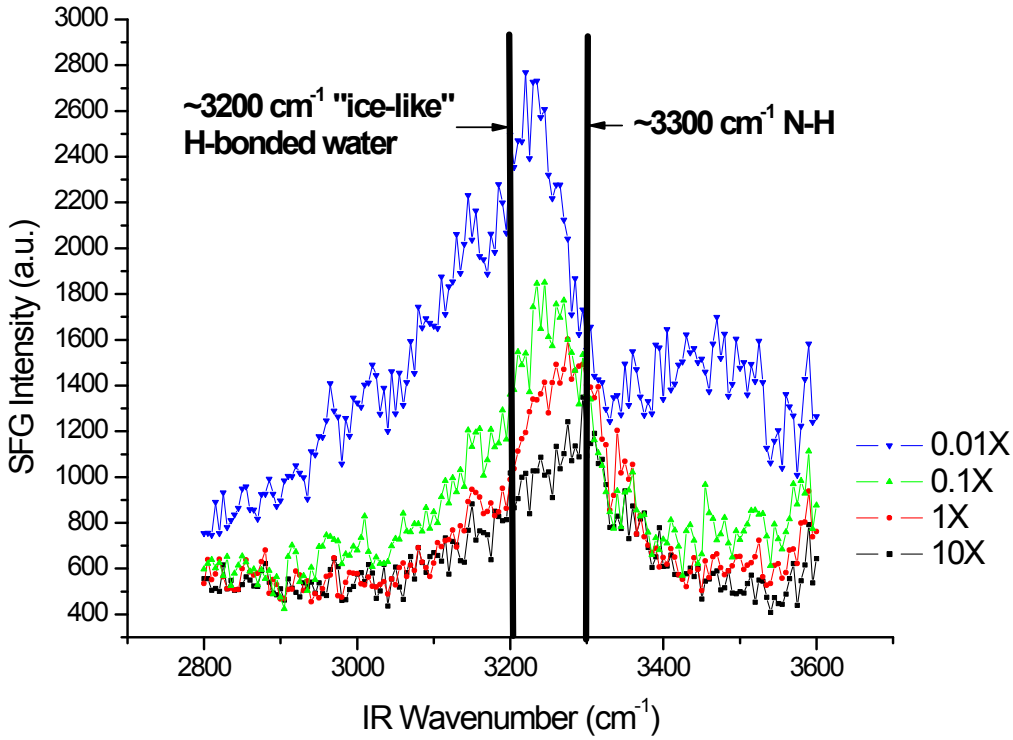

Figure 4.4. *SFG spectra of the 1 mg/mL LK_{14} at the silica/buffer interface as a function of ionic strength.*

buffer/silica interface and in the presence of peptide, the peptide N-H mode is no longer observed, and an O-H (structured water) mode grows in at 3200 cm^{-1} (with a slight growth of the 3400 cm^{-1} O-H mode). This experiment was repeated at a higher peptide concentration, namely 1 mg/mL, to illustrate the evolution of the interfacial vibrational spectra as a function of ionic strength (Figure 4.4). The trend is identical to the 0.1 mg/mL case: little water signal and a N-H mode at ~3300 cm^{-1} at high ionic strengths to strong water signal and no clear N-H mode at low ionic strengths.

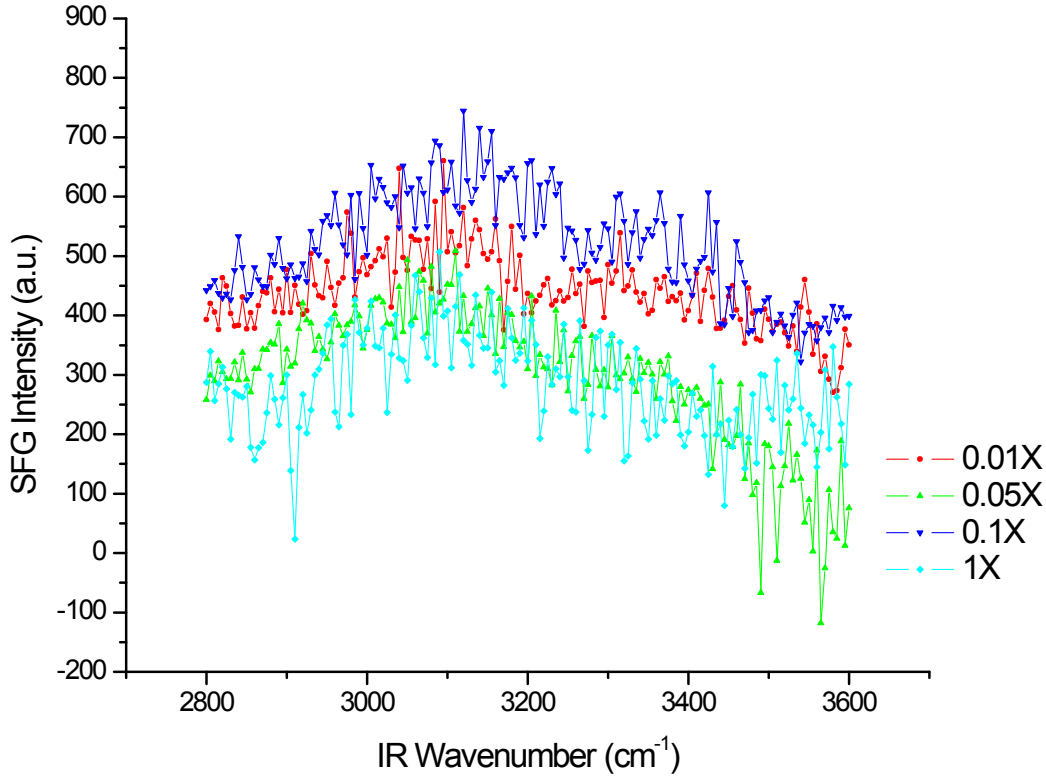

Figure 5.5. *SFG spectra of the d_8-PS/buffer interface. Little SFG signal is seen at any ionic strength.*

The background spectrum of the hydrophobic PS-d_8/buffer interface (in the absence of adsorbed peptide) is shown in Figure 5.5. Unlike the silica/buffer interface, **t**here is little dependence of the interfacial vibrational spectra on the ionic strength of solution for the hydrophobic PS-d_8/buffer interface. After injection of 0.1 mg/mL LK_{14} peptide, however, the strength of the vibrational modes of interfacial water molecules shows a strong dependence on ionic strength as seen in Figure 5.6. At low ionic strengths, water modes at 3200 cm^{-1} and 3400 cm^{-1} are observed (again assigned to ice-like and water-like hydrogen bonded water, respectively). At higher ionic strengths, these modes decrease in intensity. The 1X PBS buffer/d8-PS spectrum, which has a higher ionic

strength, indicates similar water structure to our previously reported results. The C-H modes (attributed to the peptide side chains[4]) present in the SFG spectra are not perturbed by changing of the ionic strength of the solution.

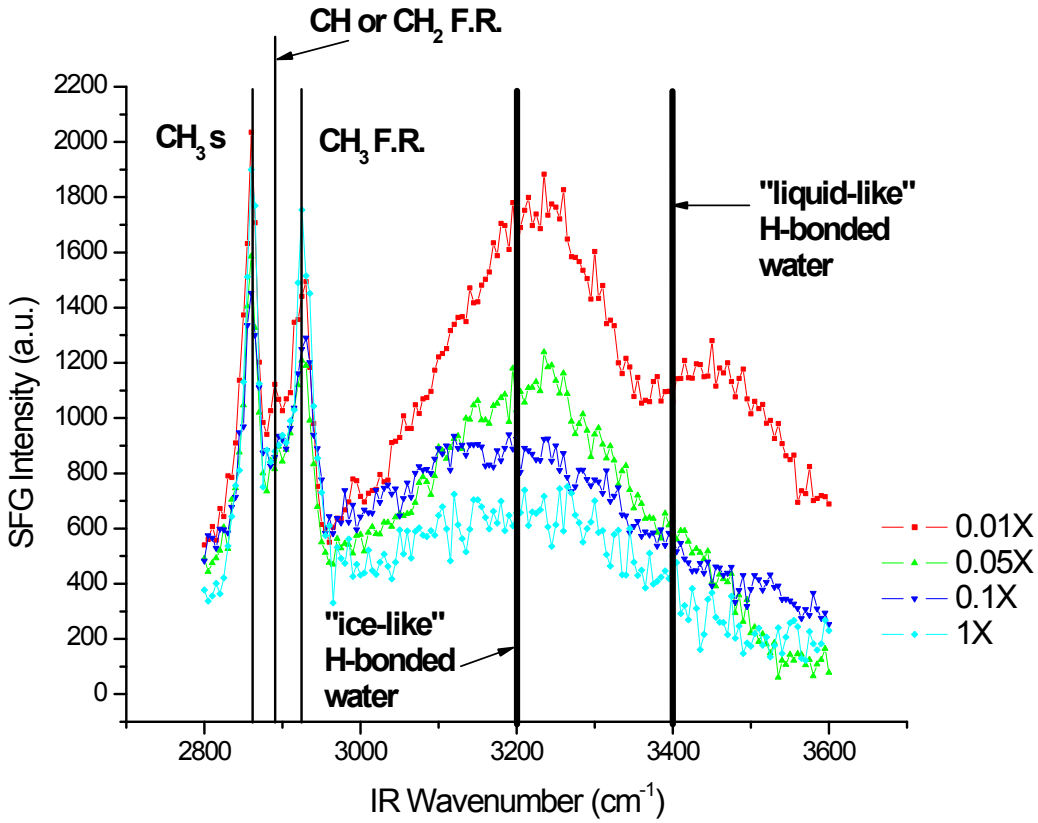

Figure 5.6. *SFG spectra of the 0.1 mg/mL LK_{14} at the d_8-PS/buffer interface as a function of ionic strength. These spectra show three C-H modes from the hydrophobic leucine side chains which we have assigned previously. Additionally, water structure at approximately 3200 cm^{-1} and 3400 cm^{-1} are observed at low ionic strengths. At higher ionic strengths, the 3400 cm^{-1} peak disappears and the 3200 cm^{-1} decreases in intensity and is red-shifted.*

4.4. Discussion

When LK_{14} peptide is adsorbed from 1X and 10X PBS buffer solution, an N-H mode is present. Below these buffer concentrations, the N-H mode disappears. CD studies of the solution structure at these same concentrations reveal the loss of secondary structure of LK_{14} in PBS buffer solutions of below 0.1X PBS buffer. Salt is known to

stabilize secondary structure in peptides and proteins, but is likely too dilute in PBS solutions below 0.01 M to induce secondary structure in the LK_{14} peptide.[6] The N-H stretch of the peptide on SiO_2 observed following LK_{14} adsorption has previously been reported. First observed for human plasma fibrinogen on silica, this mode was assigned to the hydrophilic side chains of lysine and arginine amino acids.[13] More recently, this mode has been observed for fibrinogen at the hydrophobic polystyrene interface.[14] In this work, the authors note the same time dependence of Amide I and N-H stretch (at ~3300 cm^{-1}), and suggest that this implies the N-H is not from side chains of the amino acids of the protein, but instead is from the amide groups of the peptide backbone. In our previous work, we assigned the N-H mode to either the hydrophilic amine side chains of the lysine residues or the backbone Amide A mode.[4] Here, the fact that this N-H mode is only observed for the LK_{14} peptide when this peptide has a alpha helical structure suggests that this mode is likely from the backbone Amide A. If this mode is from the positively charged side chains, the secondary structure of the peptide should be relatively unimportant, and alignment of the positively charged side chains would be driven by an electrostatic interaction of the positively charged lysine amino acid with the negatively charged silica. Further studies of isosequential peptides show no N-H mode (and recognizing these peptides are random coils in solution) further leads to the conclusion that the secondary structure of the LK_{14} peptide at high ionic strength is correlated to the appearance of this N-H mode.[9] However, the positively charged lysine side-chains of the LK_{14} peptide can not be ruled out as the source of this N-H mode, since there is a possibility that the loss of α-helicity leads to a different (i.e. random) orientation of the lysine side-chains. Nonetheless, the presence of this N-H mode suggests that the LK_{14}

peptide maintains its solution phase helical structure upon adsorption on silica. Others have reported that this helical structure is stable on polystyrene.[7]

The results of these experiments on polystyrene demonstrate two important points. One, the intensity and orientation of C-H modes of the peptide side chains on hydrophobic surfaces are independent of ionic strength and secondary structure of a peptide in solution. This likely arises from the fact that the driving force for adsorption of an amphiphilic peptide onto a hydrophobic surface is related to the rearrangement of water molecules around both the peptide and the surface (i.e. commonly referred to as hydrophobic effect). It has been suggested that the rearrangement of solvating water molecules around a solute upon adsorption should be largely independent of the secondary structure of the peptide, and primarily dependent on the size of the solute (peptide).[15] Two, these results demonstrate that the adsorption of a peptide on a surface can induce ordering in interfacial water molecules. That is, although there is no dependence of the water structure on ionic strength in the absence of peptide, adsorption of the peptide can cause alignment of interfacial water molecules (at low ionic strengths). The observation that there is a strong dependence of the intensity of the water vibrational modes on the ionic strength of the solution in the presence of peptide, but no such dependence in the absence of peptide, suggests that the polystyrene/peptide/buffer interface is quite similar to the silica/buffer and silica/peptide/buffer interface. This is because the static electric field that aligns water molecules at the silica interface is also present at the polystyrene/peptide/buffer interface. It is likely that the charged lysine residues, or perhaps ionic impurities left over from the peptide synthesis, create a charged surface upon peptide adsorption. This charged surface, much like the silica/buffer

surface, creates an interfacial potential which aligns water molecules at low ionic strengths. However, the polystyrene-buffer interface seems quite different and does not appear to be influenced by electrostatics.

4.5. Conclusion

The adsorption of the LK_{14} peptide has been studied as a function of the ionic strength of the solution on a hydrophilic silica and hydrophobic PS-d_8. CD shows that this peptide is a random coil in solution in low ionic strengths, and the peptide is a α-helix in solution at high ionic strengths. Our SFG results show that the N-H mode from the adsorbed peptide onto silica at high ionic strengths is no longer observed at low ionic strengths. This, in conjunction with our concurrent studies of isosequential peptides on silica,[9] demonstrates that the NH mode is only observed when this peptide has stable secondary structure. On hydrophobic polystyrene, we observe that the C-H modes of the leucine side chains are independent of the ionic strength. This is in contrast to the water modes, which show a strong dependence on both the ionic strength and the presence of the peptide.

Appendix 4.A: A More Detailed Sum Frequency Picture

In this section, we outline a more detailed interpretation, the so-called $\chi^{(3)}$ model,[1,16-19] of the sum frequency spectra presented at charged interfaces. In this model, the intensity of light at the sum frequency is not just proportional to the square of the second-order hyperpolarizability, $\chi^{(2)}$, but also the square of the third-order hyperpolarizability, $\chi^{(3)}$:

$$I_{SFG} = E_{SFG}^2 \propto \left|\chi^{(2)} E_{vis} E_{IR} + \chi^{(3)} E_{vis} E_{IR} E_0\right|^2 \qquad (4.A.1)$$

where E_{vis} the electric field due to the visible beam, E_{IR} is the electric field due to the infrared beam, and E_0 is a static electric field due to a charged interface. Since all of the water molecules subject to the static field E_0, which extends into the bulk solution, will contribute to the sum frequency response, we include their contribution by integrating from the interface at $z = 0$ to $z = \infty$ [1]. Thus we obtain the following:

$$E_0 = \int_0^\infty E_0(z)dz = -[\Phi(\infty) - \Phi(0)] = \Phi(0) \tag{4.A.2}$$

where $\Phi(z)$ is the electric potential at position z and $\Phi(0)$ is the electric potential at the surface (the potential very far from the interface is hence zero). Eq. 4.A.2 assumes that the density of water molecules does not change significantly from the vicinity of the silica/aqueous solution interface to the solution far from the interface. The electric potential at the surface is related to the total bulk electrolyte concentration, C, through the Gouy-Chapman model:

$$\Phi(0) = \frac{2kT}{e}\sinh^{-1}\left(\sigma_0\sqrt{\frac{\pi}{2C\varepsilon kT}}\right) \tag{4.A.3}$$

where k is Boltzmann's constant, T is the temperature, e is the electric charge, σ_0 is the surface charge density, and ε is the bulk dielectric constant. Insertion of eq. 4.A.3 into eq. 4.A.1 and 4.A.2 yields an equation that relates the total bulk electrolyte concentration to the sum frequency signal with three adjustable parameters, $\chi^{(2)}$, $\chi^{(3)}$, and σ_0. We have attempted to fit the data from the silica/buffer interface (Figure 4.2) to this model, but were unable to find a set of parameters that were both physically reasonable and allowed for a good fit. We believe that the primary reason that this model fails is due to the fact that this model treats $\chi^{(2)}$ (and also $\chi^{(3)}$) as adjustable parameters. When the strength of

an electric field at an interface changes the alignment of water molecules at that interface will also change, as seen in eq. 4.2. This is not accounted for in this model.

References

(1) Ong, S.; Zhao, X.; Eisenthal, K. B. *Chemical Physics Letters* **1992**, *191*, 327-335.

(2) Castner, D. G.; Ratner, B. D. *Surface Science* **2002**, *500*, 28-60.

(3) Ratner, B. D.; Bryant, S. J. *Annual Review of Biomedical Engineering* **2004**, *6*, 41-75.

(4) Mermut, O.; Phillips, D. C.; York, R. L.; McCrea, K. R.; Ward, R. S.; Somorjai, G. A. *Journal of the American Chemical Society* **2006**, *128*, 3598-3607.

(5) Mermut, O.; York, R. L.; Phillips, D. C.; McCrea, K. R.; Ward, R. S.; Somorjai, G. A. *Biointerphases* **2006**, *1*, P5-P11.

(6) Degrado, W. F.; Lear, J. D. *Journal of the American Chemical Society* **1985**, *107*, 7684-7689.

(7) Long, J. R.; Oyler, N.; Drobny, G. P.; Stayton, P. S. *Journal of the American Chemical Society* **2002**, *124*, 6297-6303.

(8) Westerberg, S.; Wang, C.; Chou, K.; Somorjai, G. A. *Journal of Physical Chemistry B* **2004**, *108*, 6374-6380.

(9) Phillips, D. C.; York, R. L.; Mermut, O.; McCrea, K. R.; Ward, R. S.; Somorjai, G. A. *Journal of Physical Chemistry B* **in press**.

(10) Wei, X.; Hong, S. C.; Zhuang, X. W.; Goto, T.; Shen, Y. R. *Physical Review E* **2000**, *62*, 5160-5172.

(11) Shen, Y. R. In *Frontiers in Laser Spectroscopy*; Hansch, T. W., Inguscio, M., Eds. North Holland, Amsterdam, 1994, p 139-165.

(12) Shen, Y. R.; Ostroverkhov, V. *Chemical Reviews* **2006**, *106*, 1140-1154.

(13) Jung, S. Y.; Lim, S. M.; Albertorio, F.; Kim, G.; Gurau, M. C.; Yang, R. D.; Holden, M. A.; Cremer, P. S. *Journal of the American Chemical Society* **2003**, *125*, 12782-12786.

(14) Wang, J.; Chen, X. Y.; Clarke, M. L.; Chen, Z. *Journal of Physical Chemistry B* **2006**, *110*, 5017-5024.

(15) Chandler, D. *Nature* **2005**, *437*, 640-647.

(16) Xiao, X. D.; Vogel, V.; Shen, Y. R. *Chemical Physics Letters* **1989**, *163*, 555-559.

(17) Xiao, X. D.; Vogel, V.; Shen, Y. R.; Marowsky, G. *Journal of Chemical Physics* **1991**, *94*, 2315-2323.

(18) Zhao, X.; Ong, S.; Eisenthal, K. B. *Chemical Physics Letters* **1993**, *202*, 513-520.

(19) Gragson, D. E.; Richmond, G. L. *Journal of Physical Chemistry B* **1998**, *102*, 3847-3861.

Chapter 5

How Does the Chain Length of a Peptide Influence its Interfacial Ordering? Amino Acids and Homopeptides at Hydrophobic and Hydrophilic Interfaces Studied by Sum Frequency Generation

We have studied the interfacial structure of lysine amino acid, poly-L-lysine, poly-L-proline, and proline amino acid at both the hydrophobic deuterated polystyrene/phosphate buffered saline (PBS buffer) and fused silica/PBS buffer interfaces using sum frequency generation vibrational spectroscopy (SFG). Both biomolecules at the silica/liquid interface and amino acids at the solid/liquid interface have proven difficult to study with SFG due to the poor signal-to-noise ratio of these systems. We have measured the abovementioned SFG spectra using near total internal reflection geometry (nTIR-SFG). We present a new thin film model to describe the optical effects of changing geometry on the SFG spectrum. We have found that peptide side chain ordering is stronger for longer peptides on hydrophobic surfaces. Additionally, the behavior of the hydrophilic lysine homopeptide is found to differ from earlier studied amphiphilic peptides for both the hydrophobic solid/PBS buffer and the hydrophilic/PBS buffer interface.

5.1. Introduction

The study of biomolecules, especially proteins and peptides, at interfaces remains an active area of study for both the surface science and biomedical communities.[1-3] In recent years, the surface-specific technique of Sum Frequency Generation (SFG) Vibrational Spectroscopy has been applied to the study of adsorbed proteins and peptides at the solid-liquid interface.[4,5] Of the several interfaces studied in the literature, two stand out has being quite difficult to study: biomolecules at the silica (SiO_2)/liquid interface and amino acids (at physiological pH) at any solid/liquid interface.[6] These two systems have proven challenging due to the fact that C-H modes are not observed in the SFG spectrum. The cause of these phenomena is not known a priori, but postulated to be because of the absence of amino acid side chain ordering. In the case of biomolecules at the silica/buffer interface, both the solvent and the surface are hydrophilic; a peptide or protein contains side chains that are more hydrophobic. Apparently, these hydrophobic side chains have no driving force to order at the hydrophilic silica/buffer interface. This has been demonstrated for various chain-lengths of biomolecules: amino acids, small and longer peptides, and large proteins.[6-8] Amino acids, the individual building blocks of proteins, have been studied with SFG before by Watry and Richmond,[9] who have examined several amino acids at the oil/water interface; Ji and Shen,[10] who quantitatively studied leucine at the air/water interface; and Kim et al.,[11] who studied phenylalanine at the glassy carbon electrode. In the case of amino-acids at the hydrophobic solid/liquid interface, no C-H mode ordering has been observed in the literature (with the exception of electrochemical interfaces). The reason for this is unclear; ordered C-H modes of

proteins and peptides have been observed at the hydrophobic solid/buffer interface previously.

In this report, we show that the previously unseen C-H modes discussed above can be observed using near Total Internal Reflection SFG (nTIR-SFG). Total Internal Reflection SFG (TIR-SFG) has been shown to be a promising technique for obtaining SFG spectra when the SFG signal is weak. First demonstrated by Hatch et al. in 1992,[12] this technique is now used by several groups.[13-32] Although the benefits of using TIR-SFG are clear, the interpretation of TIR-SFG spectra can be complicated, especially at the water/solid interface.[33,34] This is due to the fact that the index of refraction of water undergoes a signifigant change (~25%) as the infrared is tuned over the spectral region of interest.[35] Additionally, the imaginary component of the index of refraction of water should not be ignored in the analysis of TIR-SFG spectra.

Herein, we provide a detailed spectral analysis of the nTIR geometry employed in this experiment and demonstrate that it does not significantly alter the spectral features observed in the SFG spectrum. Our analysis shows that SFG signal can be greatly increased with the choice of nTIR geometry (surprisingly, our analysis shows that an nTIR geometry can even enhance SFG signal more than a TIR geometry). We show the SFG spectrum of lysine amino acid and proline amino acid at the deuterated polystyrene (d_8-PS)/buffer interface; additionally, we present the SFG spectrum of polylysine at the silica/buffer interface. We also compare how length influences the interfacial structure of lysine and proline peptides at both hydrophobic and hydrophilic surfaces. Finally, we compare the interfacial structure of homopeptides to amphiliphilic peptides at both hydrophobic and hydrophilic surfaces.

5.2. Experimental

Details about substrate preparation and the type of PBS buffer employed in this experiment can be found elsewhere.[36]

5.2.1. Chemicals. Lysine amino acid (K_1) was obtained from Sigma-Aldrich (cat. no. L5501) and poly-L-lysine (PLL) was also obtained from Sigma-Aldrich (cat. no. P2658). The concentration of K_1 used in these experiments was 16.5 mg/mL and the concentration of 12.5 mg/mL. Proline amino acid (P_1) was obtained from Sigma-Aldrich (cat. no. P5607) and poly-L-proline (PLP) was also obtained from Sigma-Aldrich (cat. no. P2254). The concentration of P_1 used was 500 mg/mL and the concentration of PLP was 0.5 mg/mL. All concentrations were chosen to maximize SFG signal while still maintaining solubility. In all cases the monomeric concentration of side chains was higher for the amino acid than the polypeptide.

5.2.2. SFG Theory. In vibrational SFG, a visible beam at 532 nm (ω_{VIS}) is mixed with a tunable (2800 cm^{-1}-3600 cm^{-1}) IR beam (ω_{IR}) to produce a coherent beam at the sum frequency of the two incoming beams (ω_{SFG}). The intensity of this the light at the sum frequency (I_{SFG}) is measured as a function of ω_{IR}. I_{SFG} is proportional to the macroscopic second order hyperpolarizability, $\chi^{(2)}$, which contains the relevant chemical information about the interfacial adsorbates. We present a model here that allows the extraction of $\chi^{(2)}$ from the measured I_{SFG}, which is based on the pioneering work of Bloembergen.[37]

Our model is based on a thin film of sum frequency active molecules (representing an interfacial layer) sandwiched between a solid surface (called surface 1) and an isotropic solution of these molecules (called surface 2). It is well known that the

sum-frequency response from an achiral isotropic solution is zero under the dipole approximation. Although most biomolecules are chiral, it has been established that the chiral sum-frequency response is orders of magnitude smaller than the interfacial achiral response, and we assume that the chiral sum-frequency signal from isotropic solutions is zero. Our model is for the *ssp* polarization combination.

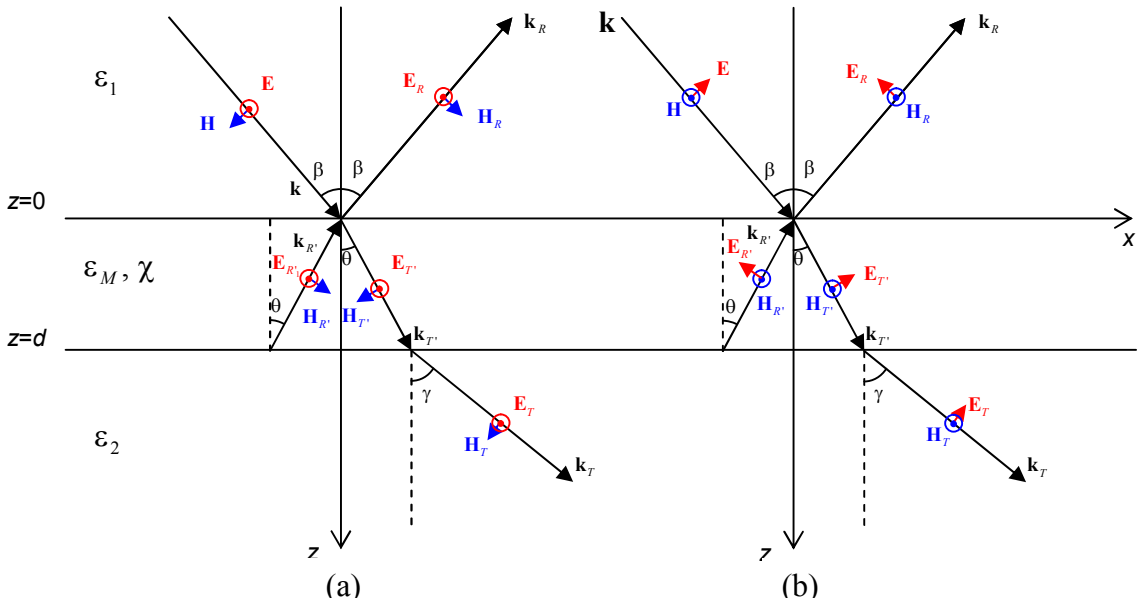

Figure 5.1. *A schematic diagram of the thin film model. Here, a non-linear thin-film is sandwiched between two linear materials. Material 1 in our experiments is the solid substrate, and material 2 is water. The s-polarized visible light is shown on the left (a) and the p-polarized infrared light is shown on the right (b). Incoming light comes into the film at angle* β *with respect to the surface normal. It is refracted into the film at angle* θ *with respect to the surface normal. At the interface between the film and material 2 (water), the light is both reflected at angle* θ *and refracted into material 2 (water) at angle* γ .

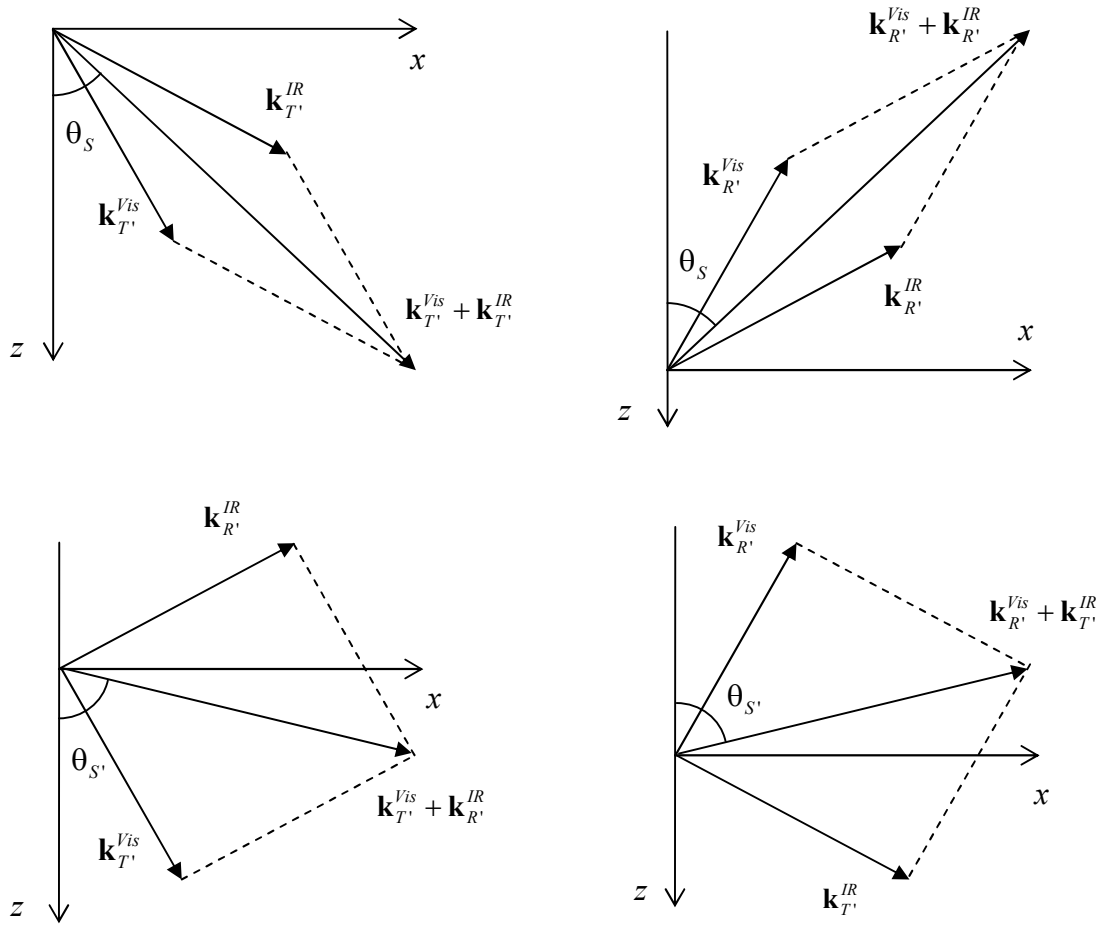

Figure 5.2. *A schematic diagram showing how the transmitted and reflected fundamental light shown in Figure 1 can mix in the non-linear thin film. The four diagrams correspond to the four source terms in equation 1.*

Two incident lights $\mathbf{E}^{Vis}\exp i(\mathbf{k}^{Vis}\cdot\mathbf{r}-\omega_{Vis}t)$ and $\mathbf{E}^{IR}\exp i(\mathbf{k}^{IR}\cdot\mathbf{r}-\omega_{IR}t)$ meet at a interfacial layer. In the interfacial layer, the refracted lights are $\mathbf{E}_{T'}^{Vis}\exp[i(\mathbf{k}_{T'}^{Vis}\cdot\mathbf{r}-\omega_{Vis}t)]$ and $\mathbf{E}_{T'}^{IR}\exp i(\mathbf{k}_{T'}^{IR}\cdot\mathbf{r}-\omega_{IR}t)$, respectively, and the reflected waves are $\mathbf{E}_{R'}^{Vis}\exp[i(\mathbf{k}_{R'}^{Vis}\cdot\mathbf{r}-\omega_{Vis}t)]$ and $\mathbf{E}_{R'}^{IR}\exp i(\mathbf{k}_{R'}^{IR}\cdot\mathbf{r}-\omega_{IR}t)$, respectively (see Figure 5.1). Four second-order nonlinear polarizations can be induced in the interfacial layer with a nonlinear medium (Figure 5.2),

$$\begin{aligned}\mathbf{P}^{NLS}(\omega_s) &= \chi^{(2)}(\omega_s):\{\mathbf{E}^{Vis}_{T'}\mathbf{E}^{IR}_{T'}\exp i[(\mathbf{k}^{Vis}_{T'}+\mathbf{k}^{IR}_{T'})\cdot\mathbf{r}-\omega_s t)] \\ &\quad +\mathbf{E}^{Vis}_{T'}\mathbf{E}^{IR}_{R'}\exp i[(\mathbf{k}^{Vis}_{T'}+\mathbf{k}^{IR}_{R'})\cdot\mathbf{r}-\omega_s t)] \\ &\quad +\mathbf{E}^{Vis}_{R'}\mathbf{E}^{IR}_{T'}\exp i[(\mathbf{k}^{Vis}_{R'}+\mathbf{k}^{IR}_{T'})\cdot\mathbf{r}-\omega_s t)] \\ &\quad +\mathbf{E}^{Vis}_{R'}\mathbf{E}^{IR}_{R'}\exp i[(\mathbf{k}^{Vis}_{R'}+\mathbf{k}^{IR}_{R'})\cdot\mathbf{r}-\omega_s t)]\}\end{aligned} \tag{1}$$

In the above equation, $\omega_s = \omega_{Vis} + \omega_{IR}$ is the sum-frequency. In the case where the incident lights are s-polarized visible and p-polarized infrared,

$$\mathbf{E}^{Vis} = E^{Vis}\mathbf{e}_y, \text{ and } \mathbf{E}^{IR} = E^{IR}(\cos\beta_{IR}\mathbf{e}_x - \sin\beta_{IR}\mathbf{e}_z), \tag{2}$$

then, in the interfacial layer, the refracted lights are:

$$\mathbf{E}^{Vis}_{T'} = E^{Vis}_{T'}\mathbf{e}_y, \text{ and } \mathbf{E}^{IR}_{T'} = E^{IR}_{T'}(\cos\theta_{IR}\mathbf{e}_x - \sin\theta_{IR}\mathbf{e}_z), \tag{3}$$

and the reflected lights are (Figure 1):

$$\mathbf{E}^{Vis}_{R'} = E^{Vis}_{R'}\mathbf{e}_y, \text{ and } \mathbf{E}^{IR}_{R'} = E^{IR}_{R'}(-\cos\theta_{IR}\mathbf{e}_x - \sin\theta_{IR}\mathbf{e}_z). \tag{4}$$

Remembering that only for an azimuthally isotropic surface s-polarized visible light and p-polarized infrared light can only access the yyz element of $\chi^{(2)}$,[38] equation 1.1 can be rewritten as:

$$\begin{aligned}\mathbf{P}^{NLS}(\omega_s) = -\chi^{(2)}_{yyz}(\omega_s)\sin\theta_{IR}\{&E^{Vis}_{T'}E^{IR}_{T'}\exp i[(\mathbf{k}^{Vis}_{T'}+\mathbf{k}^{IR}_{T'})\cdot\mathbf{r}-\omega_s t)] \\ &+E^{Vis}_{T'}E^{IR}_{R'}\exp i[(\mathbf{k}^{Vis}_{T'}+\mathbf{k}^{IR}_{R'})\cdot\mathbf{r}-\omega_s t)] \\ &+E^{Vis}_{R'}E^{IR}_{T'}\exp i[(\mathbf{k}^{Vis}_{R'}+\mathbf{k}^{IR}_{T'})\cdot\mathbf{r}-\omega_s t)] \\ &+E^{Vis}_{R'}E^{IR}_{R'}\exp i[(\mathbf{k}^{Vis}_{R'}+\mathbf{k}^{IR}_{R'})\cdot\mathbf{r}-\omega_s t)]\}\mathbf{e}_y\end{aligned} . \tag{5}$$

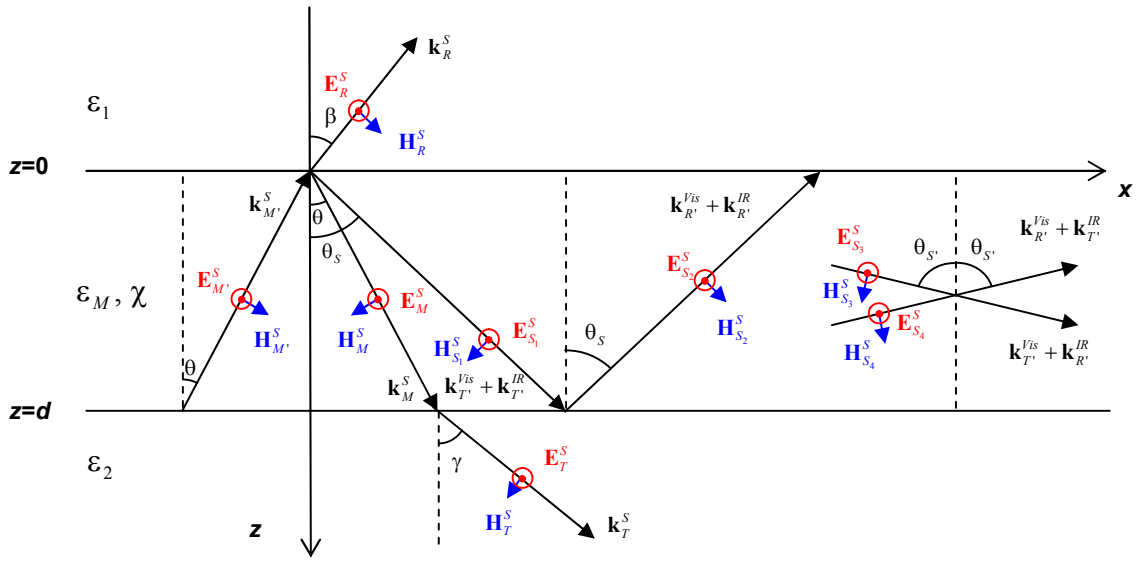

Figure 3. *A Schematic diagram of the sum-frequency beams in the non-linear thin film. There are four source beams created from the transmitted and reflected fundamental beams (see figure 2) and the sum-frequency light that is created by the source SF beams that leaves the medium in the transmitted and reflected directions.*

The induced source nonlinear polarizations can further induce SFG waves in the system (Figure 3).[37] As shown in Figure 3, all SFG-related quantities are indicated by a superscript "S". The IR and visible electric fields in the interfacial layer can be determined by the boundary conditions for the thin film model (see Appendix A for details).

After solving the non-linear wave equation[39] for the sum frequency wave in the interfacial layer,

$$-\nabla^2\mathbf{E}^S+\nabla(\nabla\cdot\mathbf{E}^S)+\frac{\varepsilon_M(\omega_s)}{c^2}\frac{\partial^2\mathbf{E}^S}{\partial t^2}=-\frac{4\pi}{c^2}\frac{\partial^2[\mathbf{P}^{NLS}(\mathbf{r},t)]}{\partial t^2} \qquad (6)$$

under the condition

$$(\mathbf{k}_{T'}^{Vis}+\mathbf{k}_{T'}^{IR})\cdot\mathbf{P}^{NLS}(\mathbf{r},t)=(\mathbf{k}_{T'}^{Vis}+\mathbf{k}_{R'}^{IR})\cdot\mathbf{P}^{NLS}(\mathbf{r},t)$$
$$=(\mathbf{k}_{R'}^{Vis}+\mathbf{k}_{T'}^{IR})\cdot\mathbf{P}^{NLS}(\mathbf{r},t)=(\mathbf{k}_{R'}^{Vis}+\mathbf{k}_{R'}^{IR})\cdot\mathbf{P}^{NLS}(\mathbf{r},t)=0 \quad ,$$

we can have:

$$\begin{aligned}\mathbf{E}^{S}&=\mathbf{E}_{M}^{S}\exp i(\mathbf{k}_{M}^{S}\cdot\mathbf{r}-\omega_{s}t)+\mathbf{E}_{M'}^{S}\exp i(\mathbf{k}_{M'}^{S}\cdot\mathbf{r}-\omega_{s}t)\\&+\mathbf{E}_{S}^{S}(\mathbf{r},t)\end{aligned} \tag{7}$$

with $\mathbf{E}_{S}^{S}(\mathbf{r},t)$ is the particular solution due to the nonlinear polarization (the subscript "S" refers to the source terms),

$$\begin{aligned}\mathbf{E}_{S}^{S}(\mathbf{r},t)&=4\pi\sin\theta_{2}\chi_{yyz}^{(2)}(\omega_{s})\\&\{\frac{1}{\varepsilon_{M}(\omega_{s})-\varepsilon_{S}(\omega_{s})}[E_{T'}^{Vis}E_{T'}^{IR}\exp i((\mathbf{k}_{T'}^{Vis}+\mathbf{k}_{T'}^{IR})\cdot\mathbf{r}-\omega_{s}t)\\&+E_{R'}^{Vis}E_{R'}^{IR}\exp i((\mathbf{k}_{R'}^{Vis}+\mathbf{k}_{R'}^{IR})\cdot\mathbf{r}-\omega_{s}t))]\\&+\frac{1}{\varepsilon_{M}(\omega_{s})-\varepsilon_{S'}(\omega_{s})}[E_{T'}^{Vis}E_{R'}^{IR}\exp i((\mathbf{k}_{T'}^{Vis}+\mathbf{k}_{R'}^{IR})\cdot\mathbf{r}-\omega_{s}t)\\&+E_{R'}^{Vis}E_{T'}^{IR}\exp i((\mathbf{k}_{R'}^{Vis}+\mathbf{k}_{T'}^{IR})\cdot\mathbf{r}-\omega_{s}t)]\}\mathbf{e}_{y}\end{aligned} \tag{8}$$

where

$$\varepsilon_{M}(\omega_{s})=\frac{c^{2}}{\omega_{s}^{2}}(k_{M}^{S})^{2}=\frac{c^{2}}{\omega_{s}^{2}}\mathbf{k}_{M}^{S}\cdot\mathbf{k}_{M}^{S}=\frac{c^{2}}{\omega_{s}^{2}}\mathbf{k}_{M'}^{S}\cdot\mathbf{k}_{M'}^{S} \tag{9}$$

$$\begin{aligned}\varepsilon_{S}(\omega_{s})&=\frac{c^{2}}{\omega_{s}^{2}}\left(k_{S}^{S}\right)^{2}=\frac{c^{2}}{\omega_{s}^{2}}(\mathbf{k}_{T'}^{Vis}+\mathbf{k}_{T'}^{IR})\cdot(\mathbf{k}_{T'}^{Vis}+\mathbf{k}_{T'}^{IR})\\&=\frac{c^{2}}{\omega_{s}^{2}}(\mathbf{k}_{R'}^{Vis}+\mathbf{k}_{R'}^{IR})\cdot(\mathbf{k}_{R'}^{Vis}+\mathbf{k}_{R'}^{IR})\end{aligned} \quad . \tag{10}$$

$$\begin{aligned}\varepsilon_{S'}(\omega_{s})&=\frac{c^{2}}{\omega_{s}^{2}}\left(k_{S'}^{S}\right)^{2}=\frac{c^{2}}{\omega_{s}^{2}}(\mathbf{k}_{T'}^{Vis}+\mathbf{k}_{R'}^{IR})\cdot(\mathbf{k}_{T'}^{Vis}+\mathbf{k}_{R'}^{IR})\\&=\frac{c^{2}}{\omega_{s}^{2}}(\mathbf{k}_{R'}^{Vis}+\mathbf{k}_{T'}^{IR})\cdot(\mathbf{k}_{R'}^{Vis}+\mathbf{k}_{T'}^{IR})\end{aligned} \tag{11}$$

For the sum frequency waves in the medium 1 and 2, there is no nonlinear polarization so the waves are

$$\mathbf{E}_1^S = E_R^S \exp i(\mathbf{k}_R^S \cdot \mathbf{r} - \omega_s t)\mathbf{e}_y \tag{12}$$

and

$$\mathbf{E}_2^S = E_T^S \exp i(\mathbf{k}_T^S \cdot \mathbf{r} - \omega_s t)\mathbf{e}_y \tag{13}$$

where

$$\varepsilon_1(\omega_s) = \frac{c^2}{\omega_s{}^2}(k_R^S)^2 = \frac{c^2}{\omega_s{}^2}\mathbf{k}_R^S \cdot \mathbf{k}_R^S, \text{ and } \varepsilon_2(\omega_s) = \frac{c^2}{\omega_s{}^2}(k_T^S)^2 = \frac{c^2}{\omega_s{}^2}\mathbf{k}_T^S \cdot \mathbf{k}_T^S \tag{14}$$

The magnetic fields in the three regions can be obtained by using the Maxwell equation $\nabla \times \mathbf{E} = -\frac{1}{c}\frac{\partial \mathbf{H}}{\partial t}$. They are:

$$\mathbf{H}_1^S = \frac{c}{\omega_s}\mathbf{k}_R^S \times \mathbf{E}_R^S \exp i(\mathbf{k}_R^S \cdot \mathbf{r} - \omega_s t)\,, \tag{15}$$

$$\mathbf{H}_2^S = \frac{c}{\omega_s}\mathbf{k}_T^S \times \mathbf{E}_T^S \exp i(\mathbf{k}_T^S \cdot \mathbf{r} - \omega_s t)\,, \tag{16}$$

and

$$\begin{aligned}\mathbf{H}^S = \frac{c}{\omega_s}[&\mathbf{k}_M^S \times \mathbf{E}_M^S \exp i(\mathbf{k}_M^S \cdot \mathbf{r} - \omega_s t) + \mathbf{k}_{M'}^S \times \mathbf{E}_{M'}^S \exp i(\mathbf{k}_{M'}^S \cdot \mathbf{r} - \omega_s t) \\ &+ \mathbf{H}_S^S(\mathbf{r}, t)]\end{aligned}, \tag{17}$$

where

$$\begin{aligned}\mathbf{H}_S^S(\mathbf{r},t) = 4\pi\frac{c}{\omega_s}&\sin\theta_2 \chi_{yyz}^{(2)}(\omega_s) \\ &\{\frac{1}{\varepsilon_M(\omega_s) - \varepsilon_S(\omega_s)}[(\mathbf{k}_{R'}^{Vis} + \mathbf{k}_{R'}^{IR})E_{T'}^{Vis}E_{T'}^{IR}\exp i((\mathbf{k}_{T'}^{Vis} + \mathbf{k}_{T'}^{IR})\cdot\mathbf{r} - \omega_s t) \\ &+ (\mathbf{k}_{R'}^{Vis} + \mathbf{k}_{R'}^{IR})E_{R'}^{Vis}E_{R'}^{IR}\exp i((\mathbf{k}_{R'}^{Vis} + \mathbf{k}_{R'}^{IR})\cdot\mathbf{r} - \omega_s t))] \\ &+ \frac{1}{\varepsilon_M(\omega_s) - \varepsilon_{S'}(\omega_s)}[(\mathbf{k}_{T'}^{Vis} + \mathbf{k}_{R'}^{IR})E_{T'}^{Vis}E_{R'}^{IR}\exp i((\mathbf{k}_{T'}^{Vis} + \mathbf{k}_{R'}^{IR})\cdot\mathbf{r} - \omega_s t) \\ &+ E_{R'}^{Vis}E_{T'}^{IR}(\mathbf{k}_{R'}^{Vis} + \mathbf{k}_{T'}^{IR})\exp i((\mathbf{k}_{R'}^{Vis} + \mathbf{k}_{T'}^{IR})\cdot\mathbf{r} - \omega_s t)]\}\times\mathbf{e}_y\end{aligned} \tag{18}$$

Now imposing the boundary conditions:

$$\mathbf{e}_y \cdot (\mathbf{E}_1^S - \mathbf{E}^S) = 0 \text{ and } \mathbf{e}_x \cdot (\mathbf{H}_1^S - \mathbf{H}^S) \tag{19}$$

at $z = 0$ and

$$\mathbf{e}_y \cdot (\mathbf{E}^S - \mathbf{E}_2^S) = 0 \text{ and } \mathbf{e}_x \cdot (\mathbf{H}^S - \mathbf{H}_2^S) \tag{20}$$

at $z = d$, we can have:

$$k_R^S \sin\beta = k_M^S \sin\theta = k_T^S \sin\gamma = k_S^S \sin\theta_S = k_{S'}^S \sin\theta_{S'} = k^{Vis} \sin\beta_{Vis} + k^{IR} \sin\beta_{IR}. \tag{21}$$

Here we have taken $k_{T',y}^{Vis} = k_{T',y}^{IR} = k_y^{Vis} = k_y^{IR} = 0$ as shown in Figure 2. All angles in Eq.(21) can be calculated since k_R^S, k_M^S, k_T^S, k_S^S, and $k_{S'}^S$ are known from Eq.(9)-(11) and (14); and $k^{Vis} \sin\beta_{Vis} + k^{IR} \sin\beta_{IR} = \frac{\varepsilon_1(\omega_{Vis})\omega_{Vis}}{c} \sin\beta_{Vis} + \frac{\varepsilon_1(\omega_{IR})\omega_{IR}}{c} \sin\beta_{IR}$. Here, β_{Vis} and β_{IR} are the incident angles of the two incident lights, respectively. As shown in Appendix B, we can obtain the electric field of SFG from the boundary conditions Eq.(19) and Eq.(20). Using Eq.(A.30), the electric field is given as:

$$E_R^S \overset{k_T \cdot d \to 0}{\approx} 2\pi i d \chi_{yyz}(\omega_s) \frac{\omega_s}{c} \frac{\sec\beta}{\varepsilon_1^{1/2}(\omega_s)} \sin\gamma_{IR} L^S L_T^{Vis} L_T^{IR} E^{Vis} E^{IR} \frac{\varepsilon_2(\omega_{IR})}{\varepsilon_M(\omega_{IR})} \tag{22}$$

here

$$L^S = \frac{2\varepsilon_1^{1/2}(\omega_s)\cos\beta}{\varepsilon_2^{1/2}(\omega_s)\cos\gamma + \varepsilon_1^{1/2}(\omega_s)\cos\beta} \tag{23}$$

$$\begin{aligned} L_T^{Vis} &= \frac{E_T^{Vis}}{E^{Vis}} \\ &= \frac{2\varepsilon_1^{1/2}(\omega_{Vis})\cos\beta_{Vis}}{\varepsilon_2^{1/2}(\omega_{Vis})\cos\gamma_{Vis} + \varepsilon_1^{1/2}(\omega_{Vis})\cos\beta_{Vis}} \end{aligned} \tag{24}$$

$$\begin{aligned} L_T^{IR} &= \frac{E_T^{IR}}{E^{IR}} \\ &= \frac{2\varepsilon_1^{1/2}(\omega_{IR})\cos\beta_{IR}}{\varepsilon_2^{1/2}(\omega_{IR})\cos\beta_{IR} + \varepsilon_1^{1/2}(\omega_{IR})\cos\gamma_{IR}} \end{aligned} \tag{25}$$

The intensity of the reflected wave is given by

$$\begin{aligned} I^{SFG} &= \frac{c}{8\pi}\mathrm{Re}[\mathbf{E}_1^S \times (\mathbf{H}_1^S)^*] \\ &= \frac{c}{8\pi}\mathrm{Re}[\varepsilon_1^{1/2}(\omega_s)]\,|\,E_R^S\,|^2 \\ &= I_0^{SFG}\left|\frac{\varepsilon_2(\omega_{IR})}{\varepsilon_M(\omega_{IR})}\right|^2 \end{aligned} \tag{26}$$

here

$$\begin{aligned} I_0^{SFG} = \frac{32\pi^3 d^2 \omega_s^{\,2}}{c^3} &\frac{\mathrm{Re}[\varepsilon_1^{1/2}(\omega_s)]}{|\,\varepsilon_1(\omega_s)\,|\,\mathrm{Re}[\varepsilon_1^{1/2}(\omega_{Vis})\varepsilon_1^{1/2}(\omega_{IR})]} \\ &\times |\,\chi_{yyz}(\omega_s)\sec\beta\,\sin\gamma_{IR} L^S L_T^{Vis} L_T^{IR}\,|^2\; I^{Vis} I^{IR} \end{aligned} \tag{27}$$

is the SFG intensity from the model without taking account the effect of the nonlinear polarizations induced by the reflected waves in the interfacial layer. Eq.(27) is more complex and general than the formula found in literatures. It can be applied to the cases involving complex refractive indices. In the example that we will discuss later, the medium 2 is water which has a frequency-dependent complex refractive index.

The macroscopic quantity $\chi_{yyz}^{(2)}$ is comprised of two components: resonant terms ($\chi_{yyz,R}^{(2)}$) and a non-resonant term ($\chi_{yyz,NR}^{(2)}$). As the IR is scanned over the spectral range of interest, the IR can have the same frequency as a molecular vibrational excitation and an SFG spectrum is obtained. This is expressed as:

$$\chi_{yyz}^{(2)} = \chi_{yyz,NR}^{(2)} + \sum_q \chi_{yyz,R,q}^{(2)} = \chi_{yyz,NR}^{(2)} + \sum_q \frac{A_q}{\omega_{IR} - \omega_q + i\Gamma_q} \tag{28}$$

where A_q, ω_q, and Γ_q are the strength, frequency, and phenomenological damping factor of the q^{th} vibrational mode. The assumption here is that the peaks arise in a Lorenztian line shape, from perturbation theory. A better approximation is that the peak shapes are a

convolution of a Lorenztian line shape and a Gaussian line shape, due to inhomogeneous line broadening in condensed phases:

$$\chi_{yyz}^{(2)} = \chi_{yyz,NR}^{(2)} + \sum_q \chi_{yyz,R,q}^{(2)} = \chi_{yyz,NR}^{(2)} + \sum_q \int d\omega_q \frac{A_q}{\omega_{IR} - \omega_q + i\Gamma_q} * \exp\left[-\frac{(\omega_q - \omega_{q_0})^2}{\Delta_q^2} \right] \quad (29)$$

where ω_{q_0} is the central frequency and Δ_q is the width of the Gaussian profile of the q^{th} vibrational mode. The spectra presented are fit to this equation.

The macroscopic quantity $\chi_{yyz,R,q}^{(2)}$ is related to the microscopic second order non-linear susceptibility, $\alpha_{yyz,R.q}^{(2)}$, through the equation

$$\chi_{yyz,R,q}^{(2)} = N \int f(\Omega) \alpha_{yyz,R,q}^{(2)} d\Omega \quad (30)$$

Where N is the number density of a vibrational mode on the surface and $f(\Omega)$ represents an orientation distribution function over Ω, which denotes a set of orientation angles that describe a transformation between the laboratory and molecular coordinate system.[40] The integral above demonstrates how molecular ordering and orientation influences SFG signal.[36]

The non-linear response of interfacial molecules can be related to their linear optical properties through the relation:

$$a_q \propto \frac{\partial \mu}{\partial Q_q} \otimes \frac{\partial \alpha^{(1)}}{\partial Q_q} \quad (31)$$

Where $\partial\mu/\partial Q_q$ and $\partial\alpha^{(1)}/\partial Q_q$ are the infrared dipole derivative and the first-order Raman polaizability derivative with respect to Q_q, the classical normal coordinate of the q^{th} vibrational mode, respectively.

SFG Experiment. Due to the small SFG signal from amino acids at the solid/liquid interface, and biomolecules at the SiO_2/liquid interface, we have chosen a different experimental geometry than our previous experiments.[36] A schematic of our "slab" geometry and "prism" geometry is shown in Figure 4. The prism geometry we have chosen allows for the infrared to be below critical angle. We chose this geometry for two reasons: (i) by increasing the angle of incidence, we could increase the SFG signal, and (ii) by staying slightly below TIR, we could avoid the complications associated with this geometry.[33,34] Since our studies are qualitative in nature, our goal was not just to maximize SFG signal, but rather to allow relative comparisons between K_1 and PLL, and qualitatively compare that to the previous results reported for other peptides.[8,36,41]

a)

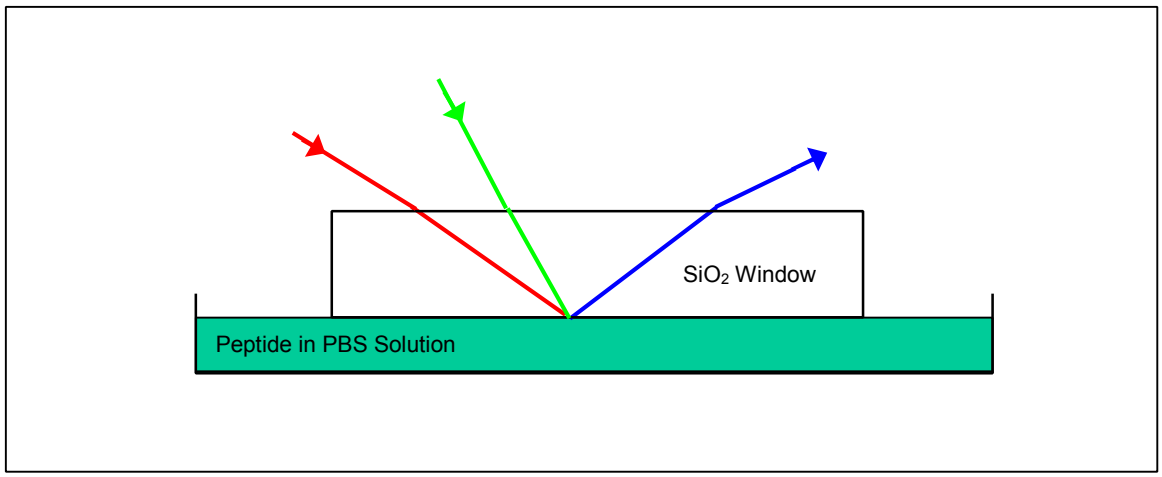

b)

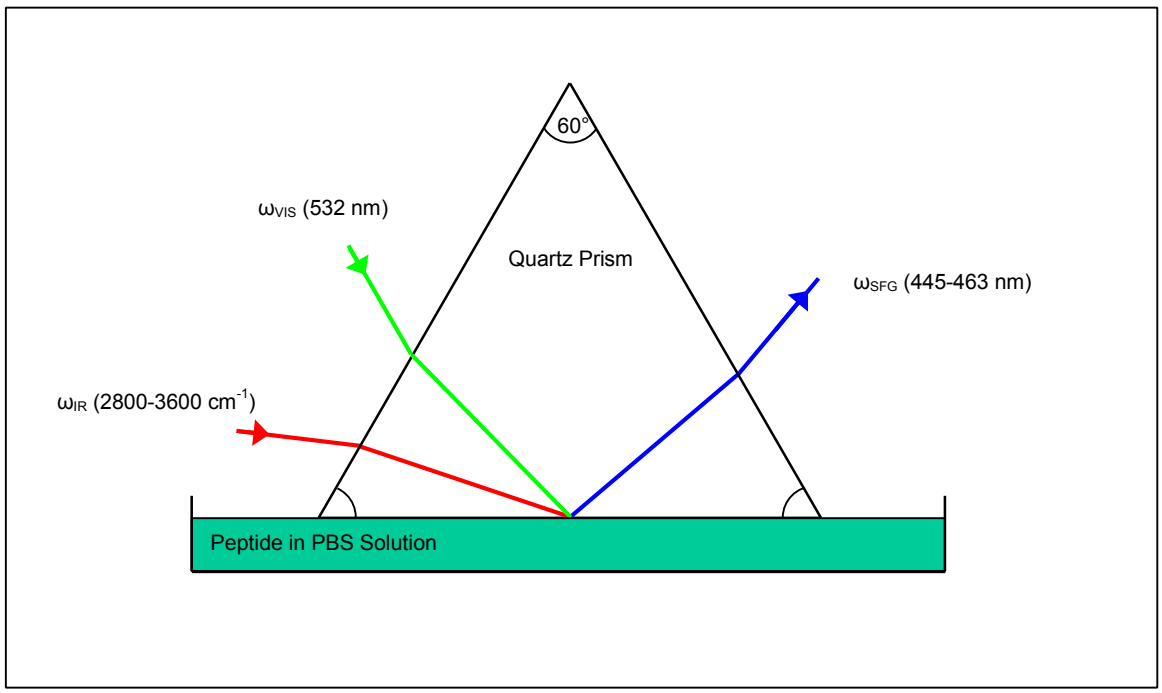

Figure 4. *a) a scheme of the "slab" geometry we have previously used in our experiments. b) a scheme of the "prism" geometry we employ in this work.*

The thin film model for the SSP SFG intensity. To understand the origin of the SFG intensity changes due to the different geometries and the complications associated with this n-TIR geometry, we have performed simulations of the SSP SFG intensity on a silica/thin film/water interface using our thin film model (see Figures 5 and 6). In the simulations, the refractive index of silica, $\varepsilon_1^{1/2}$, is equal to 1.46 for the visible light and the SFG light, and 1.41 for the IR light. For the visible light and the SFG light, the refractive index of water, $\varepsilon_2^{1/2}$, is equal to 1.34; while, for the IR light in region of 2800 cm^{-1} to 3600 cm^{-1}, the refractive index of water is a function of the IR frequency obtained from a fitting of experimental data.[35] Since we do not know the refractive index of the thin film, we have tentatively set $\varepsilon_M^{1/2}$ to be 1.40 for the visible light and 1.38 for the IR light. The three geometries, slab, prism 1, and prism 2, used for comparison are shown in Table 5.1.

Table 5.1: *Incident angles for different geometries.*

Geometry	Slab	Prism 1	Prism 2
β_{Vis}	35.5°	57.1°	56.6°
β_{IR}	38.8°	63.6°	70.6°

To investigate the SFG intensity enhancement by the n-TIR or TIR geometry, we first look at the geometric factor $G(\beta_{Vis}, \beta_{IR})$ defined as

$$G(\beta_{Vis}, \beta_{IR}) = \left| \sec\beta \sin\gamma_{IR} L^S L_T^{Vis} L_T^{IR} \right|^2 . \quad (32)$$

This factor includes all terms in the SFG intensity expression that depend on incident angles, β_{Vis} and β_{IR}, thus the ratio between this factors for two geometries is equal to the

SFG intensity ratio between the two geometries. Fig. 5(a) shows the factors at three IR frequencies as a function of the average of two incident angles, $(\beta_{IR} + \beta_{Vis})/2$ with the difference, $\beta_{IR} - \beta_{Vis}$, fixed to 6^o. In Fig. 5(a), the trends of the SFG intensity enhancement (or the increase of G) is clear when the incident angles become close to the TIR limits, and the extent of enhancement at different IR frequencies can be quite different.

The geometric factor depends on the IR frequency because L_T^{IR} in Eq. (32) is a function of the IR-frequency-dependent refractive index of water.Fig. 5(b) shows the IR-frequency dependence of the SFG intensities for two prism geometries normalized by the SFG intensity of the slab geometries. As the geometry becomes more close to the TIR region, the IR-frequency dependence is more prominent. Thus, caution must be taken when we make quantitative analysis of the SFG signal from the TIR experiment, since the frequency dependence of the SFG signal is not only coming from the second order susceptibility but also from the geometric factor when some mediums involved are IR active in the frequency range of concern.

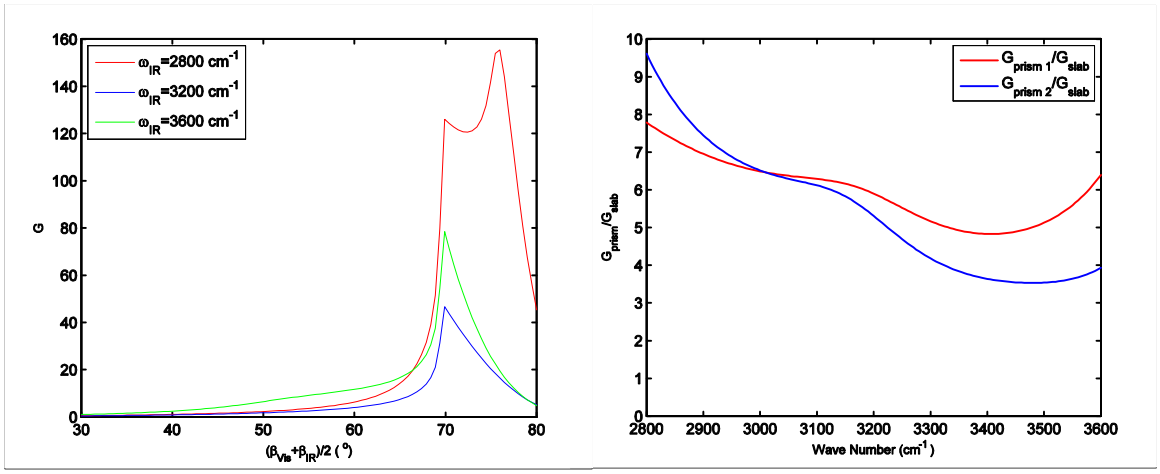

(a) (b)

Figure 5. The optical effect of changing geometry on the SFG intensity: (a) the geometric factor $G(\beta_{Vis}, \beta_{IR})$ *as a function of the average of two incident angles* $(\beta_{Vis} + \beta_{IR})/2$ *with the difference* $\beta_{IR} - \beta_{Vis}$ *fixed at* $6°$*.The enhancement of the SFG intensities by the TIR geometries is shown for three IR frequencies. (b) The IR frequency dependence of the geometric factors for two prism geometries (see Table 1). The geometric factors have been normalized by the geometric factor for the slab geometry.*

To further investigate the origin of the enhancement by the TIR geometry, we decomposes the geometric factor into three factors,

$$G(\beta_{Vis}, \beta_{IR}) = F_{SFG} F_{Vis} F_{IR} \tag{33}$$

here

$$F_{Vis} = |L_T^{Vis}|^2,\ F_{IR} = |\sin\gamma_{IR} L_T^{IR}|^2,\ \text{and}\ F_{SFG} = |\sec\beta_{SFG} L^S|^2 \tag{34}$$

From the derivations from Eq.(B.56) to Eq.(B.66), we can see that F_{Vis} is proportional to the electric field of the visible light in the interfacial layer, and that F_{IR} is proportional to the z component of the IR electric field in the interfacial layer. F_{SFG} takes care of the

optical effect purely due to the reflection of the SFG light. Fig.6 shows the incident-angle dependence of these three factors at the IR wave number of 3200 cm^{-1}. The maximal increase of $F_{IR}^{\ 2}$ is about a factor of 2 when the average of two incident angles is about 60^{o}. The maximal increases of $F_{Vis}^{\ 2}$ and $F_{SFG}^{\ 2}$ are about 4 and 18 times at the average angle around 70^{o}. For the Prism 1 geometry, the average of two incident angles is about 60^{o} and Fig.6 shows that the main contribution to the enhancement of the SFG intensity comes from the increase of F_{SFG}.

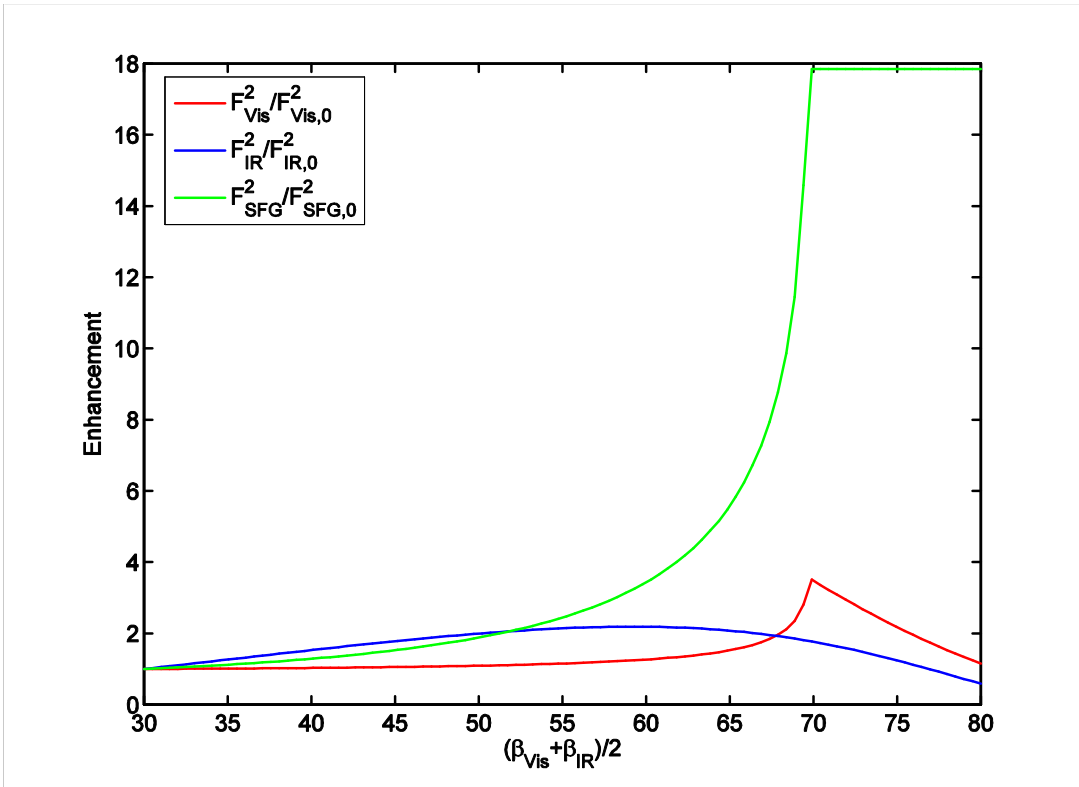

Figure 6. The optical effect of changing geometry on the SFG intensity: the factors defined in Eq.(34) *as functions of the average of two incident angles* $(\beta_{Vis}+\beta_{IR})/2$ *with*

the difference $\beta_{IR} - \beta_{Vis}$ *fixed at* $6°$. *The normalization quantities* $F_{Vis,0}$, $F_{IR,0}$, and $F_{SFG,0}$ *are the values of these factors at* $(\beta_{Vis} + \beta_{IR})/2 = 30°$.

Experimental Comparisons of Different Geometries

In order to confirm the theoretical derivation provided above, we have performed a number of experiments in two of the geometries described above (Slab and Prism1, referred to as "Prism" in this section). Figure 7 compares the SFG spectra of the h_8-PS/air interface in the two geometries. As can be seen, the overall signal is much greater in the prism geometry. Indeed, modes not seen above the noise level in the slab are clearly apparent in the prism geometry. This would suggest that a nTIR (or TIR) geometry would be beneficial *even when SFG signal can be seen far from TIR.*

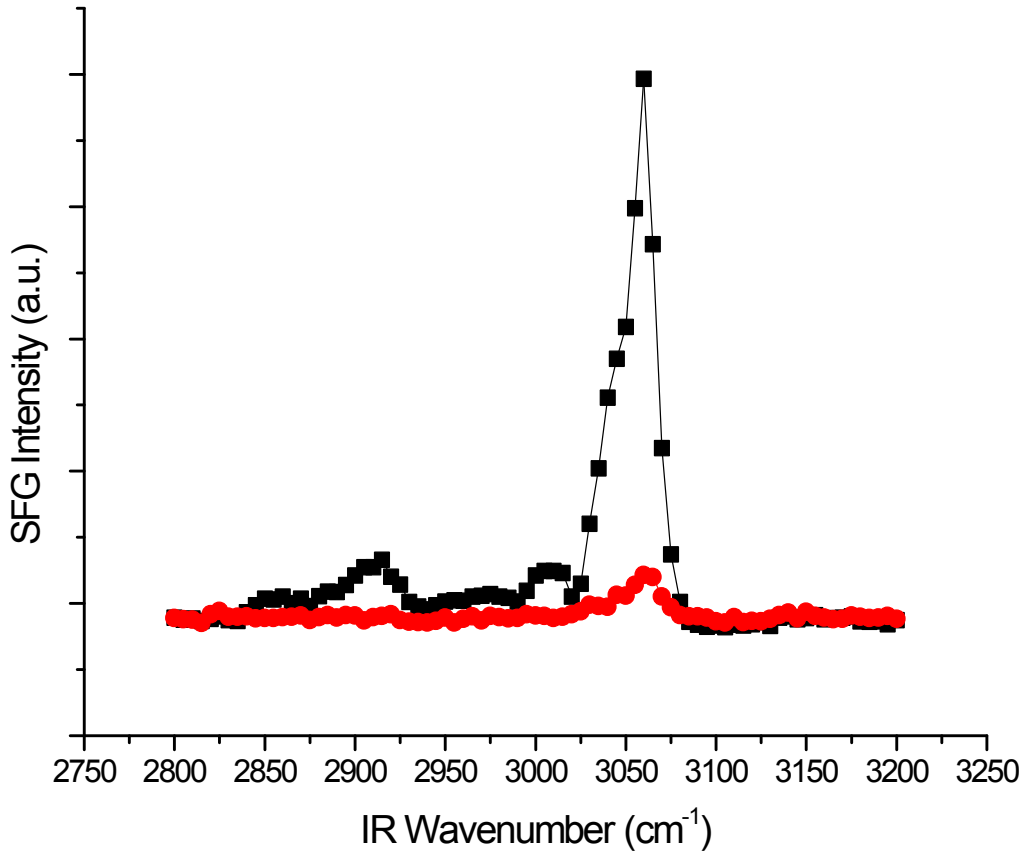

Figure 7. *The SFG spectra of h8-PS in the slab (red circle) and prism (black squares) geometries. Note the increase in the SFG signal in the prism geometry. Additionally, vibrational modes not seen in the slab geometry (due to the low signal-to-noise ratio) are clearly present in the prism geometry (e.g. the mode around 2915 cm^{-1}).*

In order to quantitatively compare experiment with theory, we have measured the SFG spectra of the fused silica/pure water (no buffer) interface in two geometries as seen in Figure 8. For a quantitative comparison, we have subtracted all residual visible intensity from the spectra. The error bars shown are from the average of 5 scans of 200 shots per data point (for the prism) and 8 scans of 200 shots per data point (for the slab).

Figure 9 shows a ratio of the intensities of the two geometries (prism/slab) as a function of infrared energy. This quantity should be independent of χ^2 and only contain geometric variables. This is compared to the ratio of G s from Figure 5(b) (Prism1/Slab). The theory agrees reasonably well with the experiment (within the experimental error), showing approximately an order of magnitude increase in signal from slab to prism. Below 2900 cm^{-1}, the theory overestimates the ratio, and above 2900 cm^{-1}, the theory underestimates the ratio. Interestingly, most of the SFG signal below 2900 cm^{-1} is from non-resonant signal, and most of the signal above 2900 cm^{-1} is from resonant enhancement from interfacial water molecules. This may imply that an improved model would need to incorporate local field effects such as dipolar coupling.

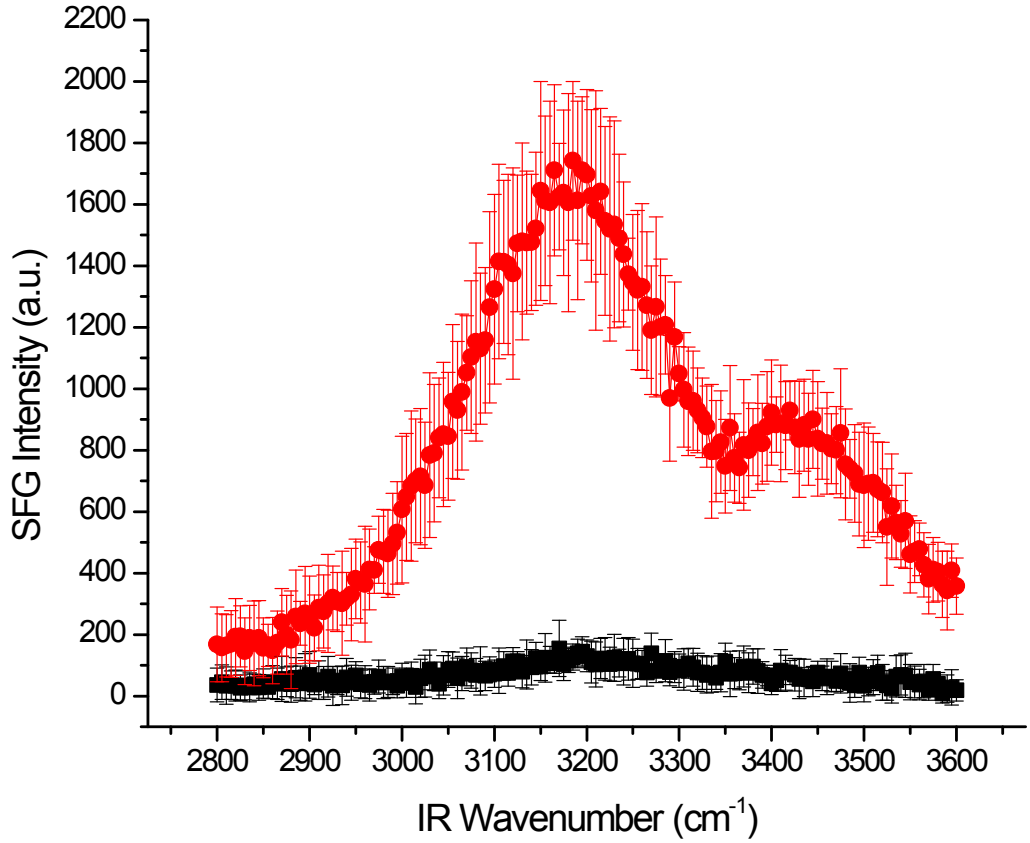

Figure 8. *SFG spectra of the pure water/silica interface for both the prism (red circles) and slab (black squares). Error bars come from the average of 5 scans of 200 shots per data point (for the prism) and 8 scans of 200 shots per data point (for the slab).*

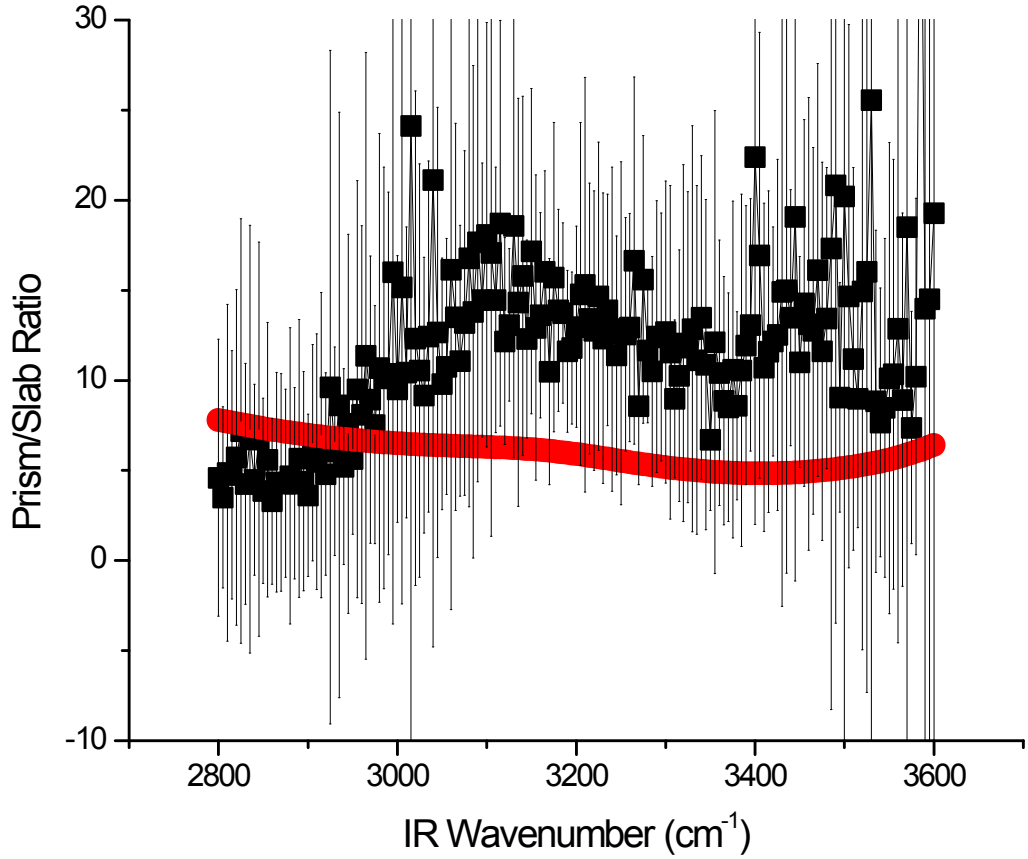

Figure 9. *The ratio of the prism geometry to the slab geometry (from Figure 8) is plotted in black squares with associated error bars. The red circles are the ratio of the square of F(prism) to F(slab) (see figure 6 (d)). The theory shows weak infrared wavelength dependence and approximately an order of magnitude increase in signal from slab to prism. Note that the theory slightly underestimates the magnitude of the increase, but is within the experimental error of our measurement.*

Results and Discussion

The SFG spectrum of K_1 on d_8-PS is shown in Figure 7. There are two peaks

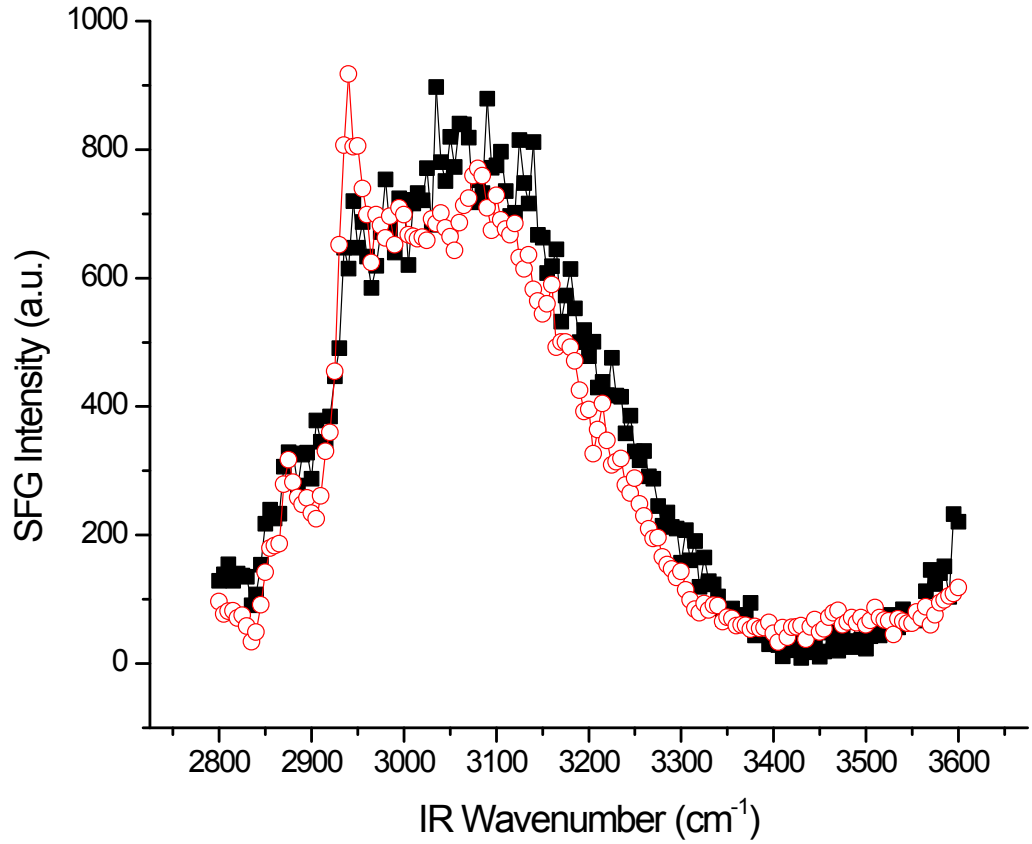

Figure 7. *The SFG spectra of the PBS buffer/d_8-PS interface (black squares) and the K_1/d_8-PS interface (open red circles). The concentration of K_1 was 16.5 mg/mL. The broad peak centered on ~3100 cm^{-1} is attributed to interfacial water. Upon adsorption of K_1, the water structure is not perturbed but two modes of smaller intensity are observed at 2870 cm^{-1} and 2935 cm^{-1}. These modes can be assigned to CH3 (s) and CH3 (as), respectively.*

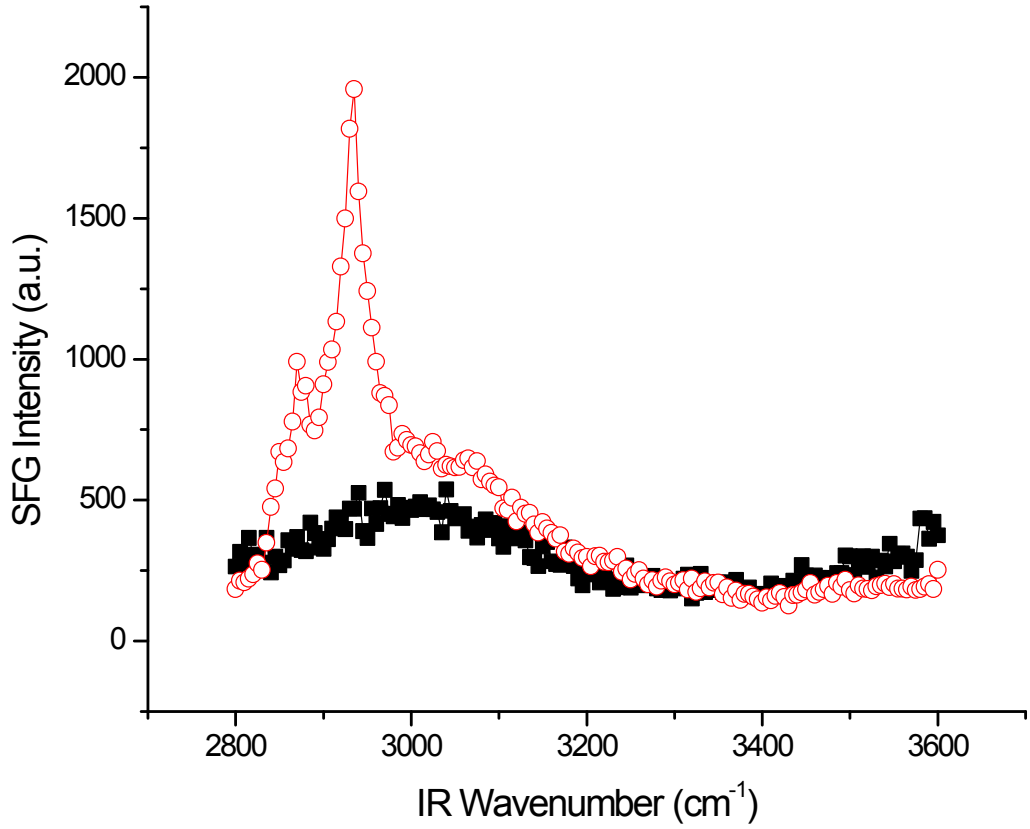

Figure 8. *The SFG spectra of the PBS buffer/d_8-PS interface (black squares) and the PLL/d_8-PS interface (open red circles). The concentration of PLL was 12.5 mg/mL. The broad peak centered on ~3100 cm^{-1} is attributed to interfacial water. Upon adsorption, two intense peaks are seen at 2870 cm^{-1} and 2935 cm^{-1}. These two modes are assigned to CH_2 (s) and CH_2 (as) respectively. The SFG intensity in the water region is slightly increased in the presence of adsorbed PLL.*

apparent in the SFG spectra: 2870 cm^{-1}, assigned to CH_2 (s); and 2935 cm^{-1}, assigned to CH_2 (as).[9] These peaks are also apparent in the SFG spectrum of PLL on d_8-PS with much greater intensity (Figure 8). The SFG spectrum (Figure 9) of PLP on d_8-PS shows three intense modes at 2875 cm^{-1}, 2935 cm^{-1}, and 2980 cm^{-1}. The mode at 2875 cm^{-1} is

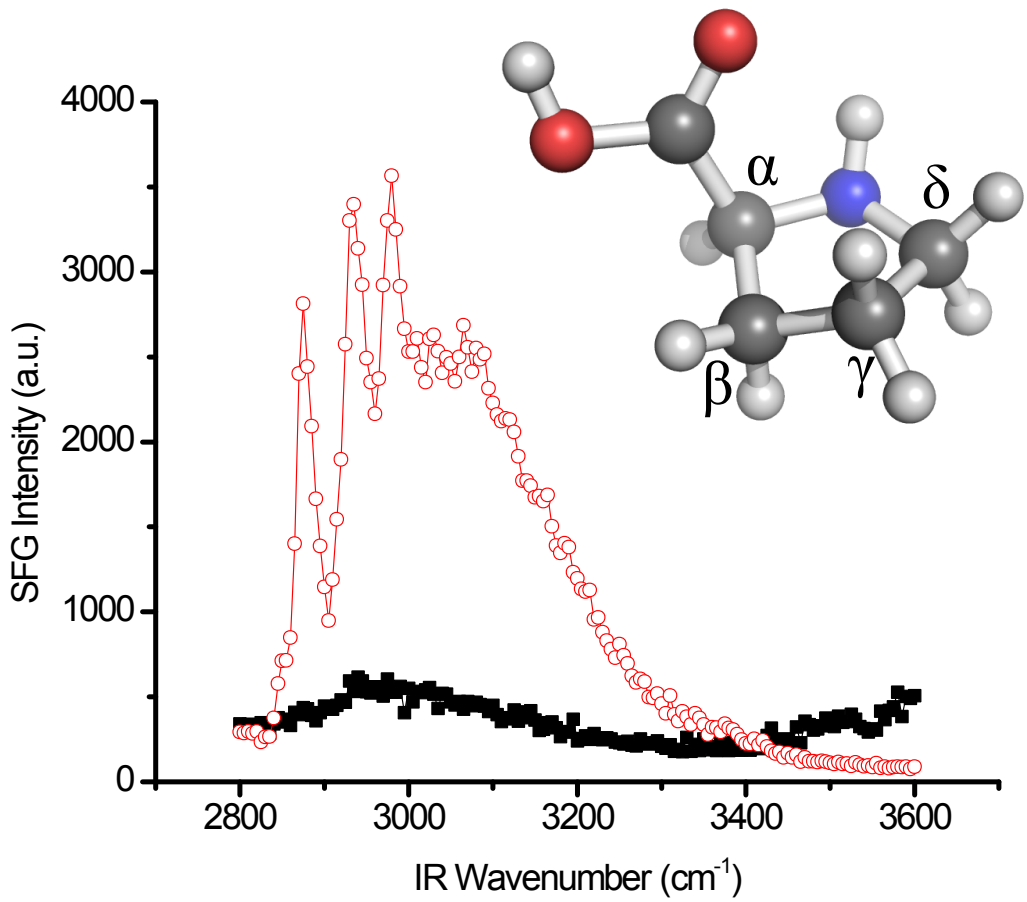

Figure 9. *The SFG spectra of the PBS buffer/d_8-PS interface (black squares) and the PLP/d_8-PS interface (open red circles). The concentration of PLP was 0.5 mg/mL. The broad peak centered on ~3100 cm^{-1} is attributed to interfacial water, and increases upon peptide adsorption. Three intense peaks are seen at 2875 cm^{-1}, 2935 cm^{-1}, and 2980 cm^{-1}. These three modes are assigned to a combination of $C_\delta H_2$ (s), $C_\beta H_2$ (s), and $C_\gamma H_2$ (s); a combination of $C_\gamma H_2$ (s) and $C_\beta H_2$ (s); and a combination of $C_\gamma H_2$ (as) and $C_\beta H_2$ (as), respectively. The inset shows proline amino acid with labeled carbons.*

assigned to a combination of $C_\delta H_2$ (s), $C_\beta H_2$ (s), and $C_\gamma H_2$ (s) (see Figure 9 for details on the nomenclature).[42] The mode at 2935 cm^{-1} is assigned to a combination of $C_\gamma H_2$ (s) and

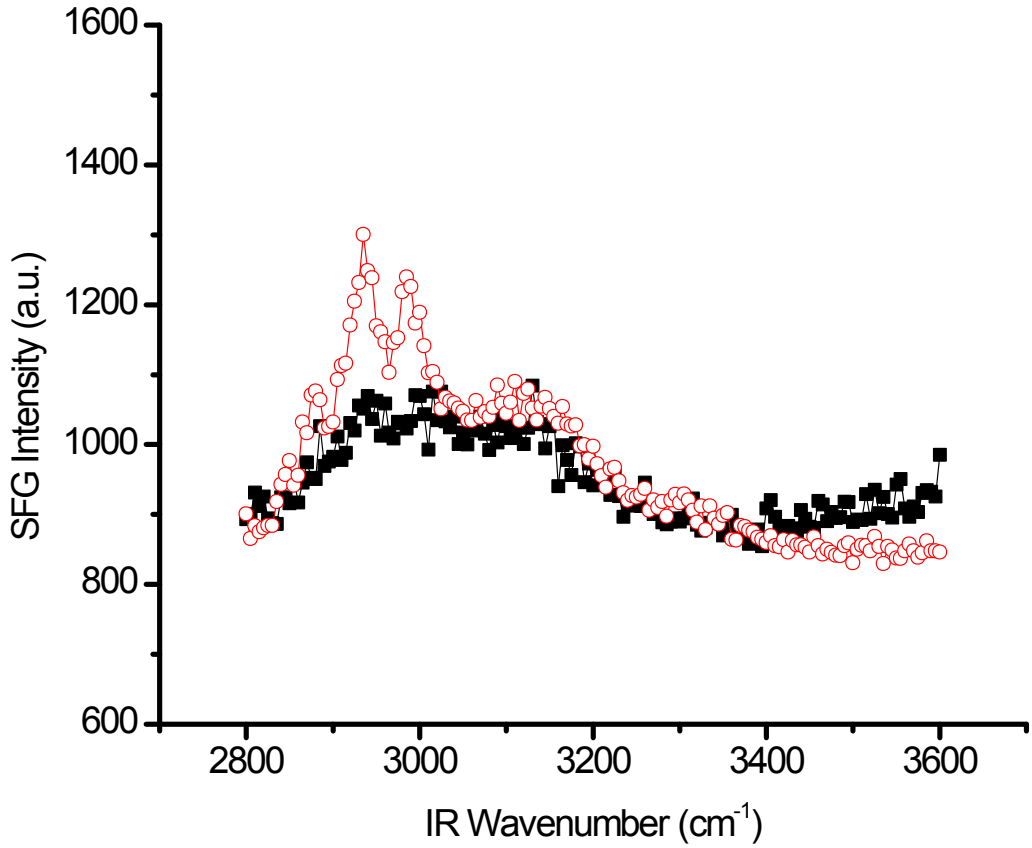

Figure 10. *The SFG spectra of the PBS buffer/d_8-PS interface (black squares) and the P_1/d_8-PS interface (open red circles). The concentration of P_1 was 500 mg/mL. The broad peak centered on ~3100 cm^{-1} is attributed to interfacial water, and is constant with amino acid adsorption. Three peaks are seen at 2875 cm^{-1}, 2935 cm^{-1}, and 2980 cm^{-1}. These three modes are assigned to a combination of $C_\delta H_2$ (s), $C_\beta H_2$ (s), and $C_\gamma H_2$ (s); a combination of $C_\gamma H_2$ (s) and $C_\beta H_2$ (s); and a combination of $C_\gamma H_2$ (as) and $C_\beta H_2$ (as), respectively.*

$C_\beta H_2$ (s).[42] Finally the vibration at 2980 cm^{-1} is assigned to a combination of $C_\gamma H_2$ (as) and $C_\beta H_2$ (as).[42] These modes are also clearly observed in the SFG spectra of P_1 on d_8-PS (Figure 10), albeit with much less intensity. The results presented here demonstrate the

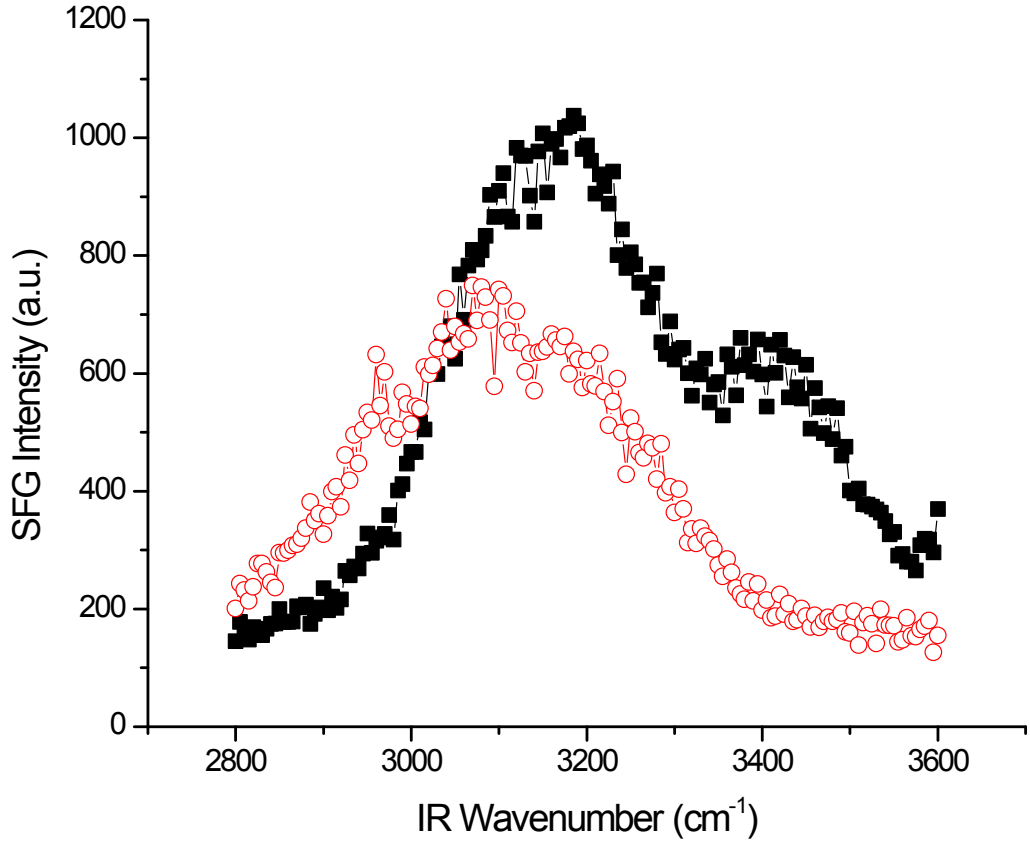

Figure 11. *The SFG spectra of the PBS buffer/silica interface (black squares) and the PLL/silica interface (open red squares). The concentration of PLL was 12.5 mg/mL. The buffer/silica interface water structure shows two very large peaks around ~3200 cm^{-1} and ~3400 cm^{-1}, attributed to tetrahedrally and less than tetrahedrally coordinated hydrogen bonded water, respectively. Upon adsorption of PLL, the overall SFG intensity in the water region is reduced, especially around 3400 cm^{-1}. The C-H mode seen around ~2960 cm^{-1} is attributed the methylene groups of the adsorbed PLL.*

effect of molecular weight (peptide chain length) on the interfacial SF signal. Even though the bulk concentration of the amino acid (both K_1 and P_1) is much higher than the concentration of polypeptide (three orders of magnitude in the case of proline!), the

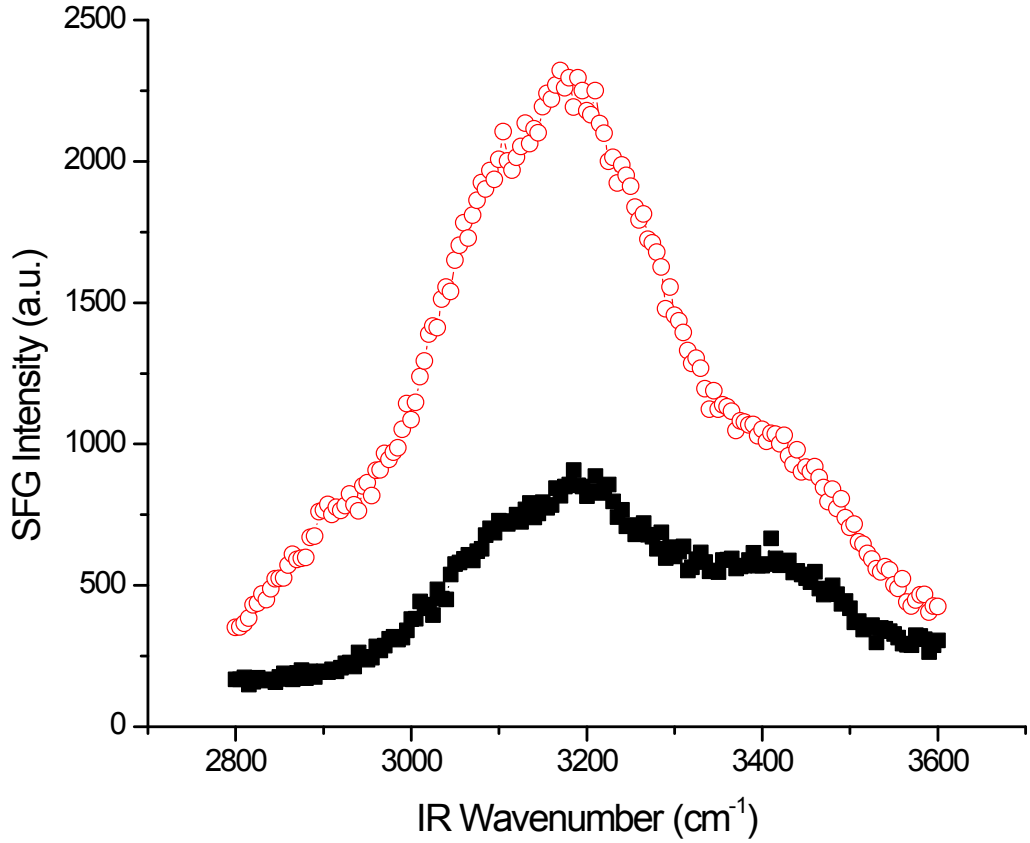

Figure 12. *The SFG of the PBS Buffer/Silica interface (black squares) and the K_1/silica interface (open red circles). The solution concentration of K_1 is 16.5 mg/mL. The water structure shows two very large peaks around ~3200 cm^{-1} and ~3400 cm^{-1}, attributed to tetrahedrally and less than tetrahedrally coordinated hydrogen bonded water, respectively. Note the increase in water signal upon K_1 adsorption.*

longer peptide shows more SFG signal attributable to the peptide. This is interpreted in terms of increased ordering of longer peptides (relative to shorter peptides) adsorbed on hydrophobic surfaces.

The SFG spectrum of PLL on SiO_2 is presented in Figure 11 and the SFG spectrum of K_1 on SiO_2 is presented in Figure 12. One small mode is observed at 2960

cm^{-1}. The assignment of this peak is non-trivial: there is no evidence for a vibrational

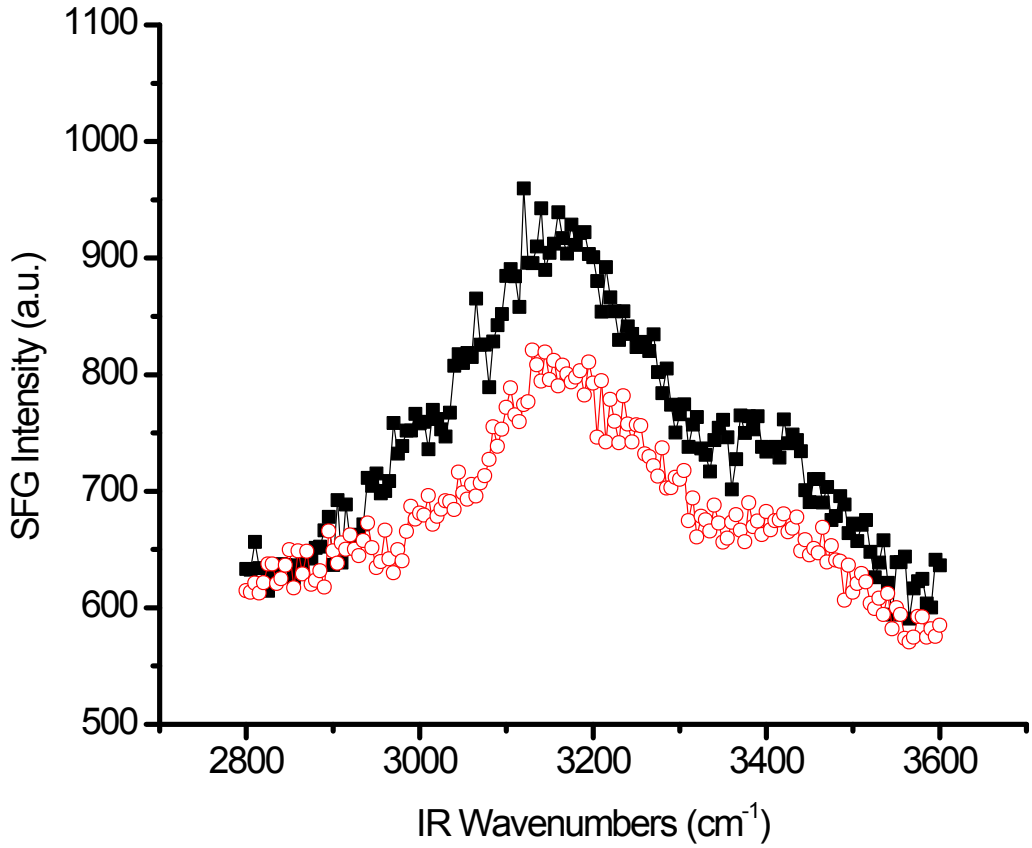

Figure 13. *The SFG of the PBS Buffer/Silica interface (black squares) and the PP/silica interface (open red circles). The solution concentration of PP is 0.5 mg/mL. The water structure shows two very broad peaks around ~3200 cm^{-1} and ~3400 cm^{-1}, attributed to tetrahedrally and less than tetrahedrally coordinated hydrogen bonded water, respectively. There is little change in the water signal upon PP adsorption.*

mode of lysine at this energy. This mode is tentatively assigned to CH_2 (as) that is strongly perturbed due to a strong electrostatic interaction between the positively charged amine groups on the lysine side-chains and the negatively charged surface of the silica. The interfacial SFG spectra of PLP and P_1 at the SiO_2/buffer interface are shown in

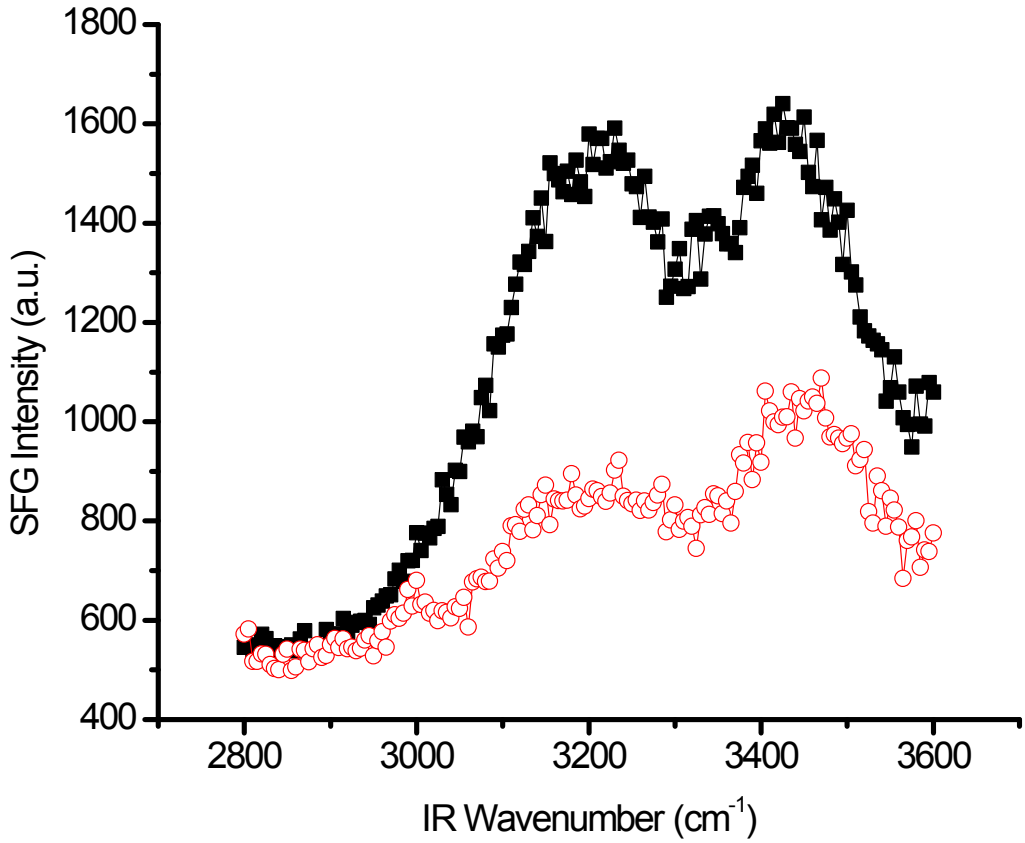

Figure 14. *The SFG of the PBS Buffer/Silica interface (black squares) and the P_1/silica interface (open red circles). The solution concentration of P_1 is 0.5 mg/mL. The water structure shows two very broad peaks around ~3200 cm^{-1} and ~3400 cm^{-1}, attributed to tetrahedrally and less than tetrahedrally coordinated hydrogen bonded water, respectively. There is a decrease in the water signal upon P_1 adsorption.*

figures 13 and 14, respectively. The high concentration P_1 may show a small mode around 3000 cm^{-1}, attributed to $C_\gamma H_2$ (as) and $C_\beta H_2$ (as), possibly shifted due to interactions with the highly charged surface.

The structure of water at interfaces remains an active area of research.[34] The interfacial water structure at the d_8-PS/buffer interface (in the absence of adsorbed

biomolecules) shows one large continuum of weak intensity centered around 3100 cm^{-1}. The largely featureless spectrum (no free O-H mode, little intensity around ~3400 cm^{-1}) and sensitivity to contamination[43] make understanding water structure at this interface difficult. Certainly, water structure present at the d_8-PS/buffer interface is quite different than "model" hydrophobic surfaces, such as the air/water[44] and OTS/water interfaces.[45] The SFG spectrum of the d_8-PS/buffer interface is quite similar to the dichloromethane-water interface that has been studied by Richmond and co-workers.[46,47] They determined that the water structure is a consequence of increased water penetration in the organic phase (something that is not likely here)[47] and general disorder at the interface.[46] Interestingly, the water structure is not perturbed by the presence of adsorbed K_1, despite the high solution concentration of amino acid. This is in contrast to PLL which slightly increased the water signal. In the case of PLP, however, the interfacial water signal is greatly enhanced; this is in opposition to the adsorbed P_1, which showed nearly no change in interfacial water signal upon amino acid adsorption.

On SiO_2, the water signal is much more intense, showing two modes centered around ~3200 cm^{-1} and ~3400 cm^{-1}. These can be attributed to ice-like tetrahedrally coordinated and water-like less than tetrahedrally coordinated hydrogen bonded water molecules, respectively.[33,34] Interestingly, the water signal is greatly enhanced when K_1 is adsorbed to the silica surface; this is in contrast to PLL, which shows a decrease in the water signal upon adsorption. The origin of this behavior is not clear: electrostatic effects should be minimized by the high ionic strength of the solution. Both PLP and P_1 show a decrease in overall water signal intensity upon biomolecule adsorption.

The PLL and K_1 results presented here are in stark contrast to our previous studies on amphiphilic peptides adsorbed on hydrophobic and hydrophilic surfaces.[5,6,8,36,41] There, on hydrophobic d_8-PS, the hydrophobic portion of the peptide was ordered and observed in the SFG spectra.[8] Here, we see the opposite: hydrophilic K_1 and PLL having ordered hydrocarbon chains on d_8-PS.

We have previously shown that an N-H mode is observed in SFG spectrum of the α-helical amphiphilic LK_{14} peptide on a hydrophilic surface.[36] This mode was attributed to either the backbone Amide A of a α-helix or the terminal amine on the hydrophilic, positively charged lysine side chains. This mode is not obviously apparent in the SFG spectra of K_1, PLL, PLP, or P_1 on SiO_2. In fact, a C-H mode is observed in the SFG spectrum of PLL and P_1 on SiO_2. These results demonstrate that the ordered parts of adsorbed peptides are strongly dependent on the amphiphilicity, or more generally, the chemical nature of the peptide.

Conclusions

We have demonstrated the feasibility of using a new experimental geometry to study amino acids at the solid/liquid interface and biomolecules at the silica/water interface. We have developed a new thin film model to understand the effect of geometry on our experimental sum frequency results. Our results demonstrate that ordering of lysine amino acid side chains occur at the d_8-PS/buffer interface. Additionally, we have observed ordering of polylysine side chains at the silica/buffer interface. On both hydrophobic and hydrophilic surfaces, longer peptides showed more SFG attributed to the adsorbed peptide. We interpret this as increased ordering among longer peptides.

These results at both hydrophobic and hydrophilic surfaces are significantly different than our previous studies of amphiphilic peptides.

Acknowledgements

This work was supported by UC Discovery Grant BioSTAR 01-10132, and the Director, Office of Science, Office of Advanced Scientific Computing Research, Office of Basic Energy Sciences, Materials Science and Engineering Division, of the U.S. Department of Energy under Contract No. DE-AC02-05CH11231. We would like to thank Dr. Ozzy Mermut and Dr. Diana C. Phillips for earlier work on this project, and Dr. Sasha J. Kweskin for inspiration to experiment with TIR-SFG.

Appendix A: The refractive and reflective light in the interfacial layer

In this appendix, we derive the Fresnel's coefficients for the refractive and reflective light induced by incident light in the interfacial layer. Derivations are provided in two cases for the s-polarized and p-polarized incident light.

For the s-polarized incident light (see Figure 1(b)):

In medium 1, the light wave is described by

$$\mathbf{E}_1 = [E\exp i(\mathbf{k}\cdot\mathbf{r}-\omega t) + E_R\exp i(\mathbf{k}_R\cdot\mathbf{r}-\omega t)]\mathbf{e}_y \tag{A.1}$$

$$\begin{aligned}\mathbf{H}_1 &= E(\mathbf{k}\times\mathbf{e}_y)\exp i(\mathbf{k}\cdot\mathbf{r}-\omega t) + E_R(\mathbf{k}_R\times\mathbf{e}_y)\exp i(\mathbf{k}_R\cdot\mathbf{r}-\omega t)\\ &= kE(-\cos\beta\,\mathbf{e}_x+\sin\beta\,\mathbf{e}_z)\exp i(\mathbf{k}\cdot\mathbf{r}-\omega t) + k_R E_R(\cos\beta\,\mathbf{e}_x+\sin\beta\,\mathbf{e}_z)\exp i(\mathbf{k}_R\cdot\mathbf{r}-\omega t)\end{aligned} \tag{A.2}$$

with

$$\mathbf{k}_R = k_x\mathbf{e}_x + k_y\mathbf{e}_y - k_z\mathbf{e}_z \text{ and } k_R = k = \frac{\varepsilon_1^{1/2}(\omega)\omega}{c}; \tag{A.3}$$

In the interfacial layer, the wave is described by

$$\mathbf{E}_M = [E_{T'}\exp i(\mathbf{k}_{T'}\cdot\mathbf{r}-\omega t) + E_{R'}\exp i(\mathbf{k}_{R'}\cdot\mathbf{r}-\omega t)]\mathbf{e}_y \tag{A.4}$$

$$\begin{aligned}\mathbf{H}_M &= E_{T'}(\mathbf{k}_{T'}\times\mathbf{e}_y)\exp i(\mathbf{k}_{T'}\cdot\mathbf{r}-\omega t)+E_{R'}(\mathbf{k}_{R'}\times\mathbf{e}_y)\exp i(\mathbf{k}_{R'}\cdot\mathbf{r}-\omega t)\\ &= k_{T'}E_{T'}(-\cos\theta\,\mathbf{e}_x+\sin\theta\,\mathbf{e}_z)\exp i(\mathbf{k}_{T'}\cdot\mathbf{r}-\omega t)+k_{R'}E_{R'}(\cos\theta\,\mathbf{e}_x+\sin\theta\,\mathbf{e}_z)\exp i(\mathbf{k}_{R'}\cdot\mathbf{r}-\omega t)\end{aligned} \tag{A.5}$$

with

$$\mathbf{k}_{R'}=k_{T',x}\mathbf{e}_x+k_{T',y}\mathbf{e}_y-k_{T',z}\mathbf{e}_z \text{ and } k_{R'}=k_{T'}=\frac{\varepsilon_M^{1/2}(\omega)\omega}{c}; \tag{A.6}$$

In medium 2, the light wave is described by

$$\mathbf{E}_2=E_T\exp i(\mathbf{k}_T\cdot\mathbf{r}-\omega t)\mathbf{e}_y \tag{A.7}$$

$$\begin{aligned}\mathbf{H}_2 &= E_T(\mathbf{k}_T\times\mathbf{e}_y)\exp i(\mathbf{k}_T\cdot\mathbf{r}-\omega t)\\ &= k_T E_T(-\cos\gamma\,\mathbf{e}_x+\sin\gamma\,\mathbf{e}_z)\exp i(\mathbf{k}_T\cdot\mathbf{r}-\omega t)\end{aligned} \tag{A.8}$$

with

$$k_T=\frac{\varepsilon_2^{1/2}(\omega)\omega}{c}. \tag{A.9}$$

After imposing the boundary conditions at $z=0$, we have

$$k_{T'}\sin\theta=k\sin\beta \tag{A.10}$$

$$E+E_R=E_{T'}+E_{R'} \tag{A.11}$$

$$-kE\cos\beta+k_R E_R\cos\beta=-k_{T'}E_{T'}\cos\theta+k_{R'}E_{R'}\cos\theta\ . \tag{A.12}$$

The boundary conditions at $z=d$ give

$$k_{T'}\sin\theta=k_T\sin\gamma \tag{A.13}$$

$$E_{T'}\exp i(k_{T'}d\cos\theta)+E_{R'}\exp i(-k_{R'}d\cos\theta)=E_T\exp i(k_T d\cos\gamma) \tag{A.14}$$

$$\begin{aligned}&-k_{T'}E_{T'}\cos\theta\exp i(k_{T'}d\cos\theta)+k_{R'}E_{R'}\cos\theta\exp i(-k_{R'}d\cos\theta)\\ &=-k_T E_T\cos\gamma\exp i(k_T d\cos\gamma)\end{aligned} \tag{A.15}$$

From Eq.(A.11), (A.12), (A.14) and (A.15), we have

$$E_{T'} = 2D^{-1}\varepsilon_1^{1/2}(\omega)\cos\beta\,(\varepsilon_M^{1/2}(\omega)\cos\theta + \varepsilon_2^{1/2}(\omega)\cos\gamma)E$$
$$\overset{k_{T'}d\to 0}{\approx} \frac{2\varepsilon_1^{1/2}(\omega)\cos\beta}{\varepsilon_1^{1/2}(\omega)\cos\beta + \varepsilon_2^{1/2}(\omega)\cos\gamma}\frac{\varepsilon_M^{1/2}(\omega)\cos\theta + \varepsilon_2^{1/2}(\omega)\cos\gamma}{2\varepsilon_M^{1/2}(\omega)\cos\theta}E, \tag{A.16}$$

$$E_{R'} = 2D^{-1}\varepsilon_1^{1/2}(\omega)\cos\beta\,(\varepsilon_M^{1/2}(\omega)\cos\theta - \varepsilon_2^{1/2}(\omega)\cos\gamma)e^{2ik_{T'}d\cos\theta}E$$
$$\overset{k_{T'}d\to 0}{\approx} \frac{\varepsilon_1^{1/2}(\omega)\cos\beta}{\varepsilon_1^{1/2}(\omega)\cos\beta + \varepsilon_2^{1/2}(\omega)\cos\gamma}\frac{\varepsilon_M^{1/2}(\omega)\cos\theta - \varepsilon_2^{1/2}(\omega)\cos\gamma}{\varepsilon_M^{1/2}(\omega)\cos\theta}E \tag{A.17}$$

Here

$$D = \varepsilon_M^{1/2}(\omega)\cos\theta\,(\varepsilon_1^{1/2}(\omega)\cos\beta + \varepsilon_2^{1/2}(\omega)\cos\gamma)(1+e^{2ik_{T'}d\cos\theta})$$
$$+(\varepsilon_1^{1/2}(\omega)\varepsilon_2^{1/2}(\omega)\cos\beta\cos\gamma + \varepsilon_M(\omega)\cos^2\theta)(1-e^{2ik_{T'}d\cos\theta}). \tag{A.18}$$
$$\overset{k_{T'}d\to 0}{\approx} 2\varepsilon_M^{1/2}(\omega)\cos\theta\,(\varepsilon_1^{1/2}(\omega)\cos\beta + \varepsilon_2^{1/2}(\omega)\cos\gamma)$$

From Eq.(A.16) and (A.17), we can obtain the Fresnel's coefficients for the refractive and reflective light in the interfacial layer as

$$L_{T'} \equiv \frac{E_{T'}}{E}$$
$$\overset{k_{T'}d\to 0}{\approx} \frac{2\varepsilon_1^{1/2}(\omega)\cos\beta}{\varepsilon_1^{1/2}(\omega)\cos\beta + \varepsilon_2^{1/2}(\omega)\cos\gamma}\frac{\varepsilon_M^{1/2}(\omega)\cos\theta + \varepsilon_2^{1/2}(\omega)\cos\gamma}{2\varepsilon_M^{1/2}(\omega)\cos\theta}, \tag{A.19}$$

and

$$L_{R'} \equiv \frac{E_{R'}}{E}$$
$$\overset{k_{T'}d\to 0}{\approx} \frac{\varepsilon_1^{1/2}(\omega)\cos\beta}{\varepsilon_1^{1/2}(\omega)\cos\beta + \varepsilon_2^{1/2}(\omega)\cos\gamma}\frac{\varepsilon_M^{1/2}(\omega)\cos\theta - \varepsilon_2^{1/2}(\omega)\cos\gamma}{\varepsilon_M^{1/2}(\omega)\cos\theta}, \tag{A.20}$$

respectively.

For the p-polarized incident light (see Figure 1(b)):

In medium 1, the light wave is described by

$$\mathbf{E}_1 = E(\cos\beta\,\mathbf{e}_x - \sin\beta\,\mathbf{e}_z)\exp i(\mathbf{k}\cdot\mathbf{r} - \omega t)$$
$$+ E_R(-\cos\beta\,\mathbf{e}_x - \sin\beta\,\mathbf{e}_z)\exp i(\mathbf{k}_R\cdot\mathbf{r} - \omega t) \tag{A.21}$$

$$\begin{aligned}\mathbf{H}_1 &= E\mathbf{k}\times(\cos\beta\mathbf{e}_x-\sin\beta\mathbf{e}_z)\exp i(\mathbf{k}\cdot\mathbf{r}-\omega t)\\ &\quad+E_R\mathbf{k}_R\times(-\cos\beta\mathbf{e}_x-\sin\beta\mathbf{e}_z)\exp i(\mathbf{k}_R\cdot\mathbf{r}-\omega t)\\ &=[kE\exp i(\mathbf{k}\cdot\mathbf{r}-\omega t)+k_RE_R\exp i(\mathbf{k}_R\cdot\mathbf{r}-\omega t)]\mathbf{e}_y\end{aligned} \tag{A.22}$$

with

$$\mathbf{k}_R=k_x\mathbf{e}_x+k_y\mathbf{e}_y-k_z\mathbf{e}_z \text{ and } k_R=k=\frac{\varepsilon_1^{1/2}(\omega)\omega}{c}; \tag{A.23}$$

In the interfacial layer, the wave is described by

$$\begin{aligned}\mathbf{E}_M &= E_{T'}(\cos\theta\mathbf{e}_x-\sin\theta\mathbf{e}_z)\exp i(\mathbf{k}_{T'}\cdot\mathbf{r}-\omega t)\\ &\quad+E_{R'}(-\cos\theta\mathbf{e}_x-\sin\theta\mathbf{e}_z)\exp i(\mathbf{k}_{R'}\cdot\mathbf{r}-\omega t)\end{aligned} \tag{A.24}$$

$$\begin{aligned}\mathbf{H}_M &= E_{T'}\mathbf{k}_{T'}\times(\cos\theta\mathbf{e}_x-\sin\theta\mathbf{e}_z)\exp i(\mathbf{k}_{T'}\cdot\mathbf{r}-\omega t)\\ &\quad+E_{R'}\mathbf{k}_{R'}\times(-\cos\theta\mathbf{e}_x-\sin\theta\mathbf{e}_z)\exp i(\mathbf{k}_{R'}\cdot\mathbf{r}-\omega t)\\ &=[k_{T'}E_{T'}\exp i(\mathbf{k}_{T'}\cdot\mathbf{r}-\omega t)+k_{R'}E_{R'}\exp i(\mathbf{k}_{R'}\cdot\mathbf{r}-\omega t)]\mathbf{e}_y\end{aligned} \tag{A.25}$$

with

$$\mathbf{k}_{R'}=k_{T',x}\mathbf{e}_x+k_{T',y}\mathbf{e}_y-k_{T',z}\mathbf{e}_z \text{ and } k_{R'}=k_{T'}=\frac{\varepsilon_M^{1/2}(\omega)\omega}{c}; \tag{A.26}$$

In medium 2, the light wave is described by

$$\mathbf{E}_2=E_T(\cos\gamma\,\mathbf{e}_x-\sin\gamma\,\mathbf{e}_z)\exp i(\mathbf{k}_T\cdot\mathbf{r}-\omega t) \tag{A.27}$$

$$\begin{aligned}\mathbf{H}_2 &= E_T\mathbf{k}_T\times(\cos\gamma\,\mathbf{e}_x-\sin\gamma\,\mathbf{e}_z)\exp i(\mathbf{k}_T\cdot\mathbf{r}-\omega t)\\ &=k_TE_T\exp i(\mathbf{k}_T\cdot\mathbf{r}-\omega t)\mathbf{e}_y\end{aligned} \tag{A.28}$$

with

$$k_T=\frac{\varepsilon_2^{1/2}(\omega)\omega}{c}. \tag{A.29}$$

After imposing the boundary conditions at $z=0$, we have

$$k_{T'}\sin\theta=k_T\sin\gamma \tag{A.30}$$

$$E\cos\beta-E_R\cos\beta=E_{T'}\cos\theta-E_{R'}\cos\theta \tag{A.31}$$

$$kE + k_R E_R = k_{T'} E_{T'} + k_{R'} E_{R'} . \tag{A.32}$$

The boundary conditions at $z = d$ give

$$k_{T'} \sin\theta = k_T \sin\gamma \tag{A.33}$$

$$\begin{aligned} &E_{T'} \cos\theta \exp i(k_{T'} d \cos\theta) - E_{R'} \cos\theta \exp i(-k_{R'} d \cos\theta) \\ &= E_T \cos\gamma \exp i(k_T d \cos\gamma) \end{aligned} \tag{A.34}$$

$$\begin{aligned} &k_{T'} E_{T'} \exp i(k_{T'} d \cos\theta) + k_{R'} E_{R'} \exp i(-k_{R'} d \cos\theta) \\ &= k_T E_T \exp i(k_T d \cos\gamma) \end{aligned} \tag{A.35}$$

From Eq.(A.31), (A.32), (A.34) and (A.35), we have

$$\begin{aligned} E_{T'} &= 2D^{-1} \varepsilon_1^{1/2}(\omega) \cos\beta \, (\varepsilon_M^{1/2}(\omega) \cos\gamma + \varepsilon_2^{1/2}(\omega) \cos\theta) E \\ &\overset{k_{T'} d \to 0}{\approx} \frac{2\varepsilon_1^{1/2}(\omega) \cos\beta}{\varepsilon_2^{1/2}(\omega) \cos\beta + \varepsilon_1^{1/2}(\omega) \cos\gamma} \frac{\varepsilon_M^{1/2}(\omega) \cos\gamma + \varepsilon_2^{1/2}(\omega) \cos\theta}{2\varepsilon_M^{1/2}(\omega) \cos\theta} E \end{aligned} \tag{A.36}$$

$$\begin{aligned} E_{R'} &= 2D^{-1} \varepsilon_1^{1/2}(\omega) \cos\beta \, (\varepsilon_2^{1/2}(\omega) \cos\theta - \varepsilon_M^{1/2}(\omega) \cos\gamma) e^{2ik_{T'} d \cos\theta} E \\ &\overset{k_{T'} d \to 0}{\approx} \frac{\varepsilon_1^{1/2}(\omega) \cos\beta}{\varepsilon_2^{1/2}(\omega) \cos\beta + \varepsilon_1^{1/2}(\omega) \cos\gamma} \frac{\varepsilon_2^{1/2}(\omega) \cos\theta - \varepsilon_M^{1/2}(\omega) \cos\gamma}{\varepsilon_M^{1/2}(\omega) \cos\theta} E \end{aligned} \tag{A.37}$$

Here

$$\begin{aligned} D &= \varepsilon_M^{1/2}(\omega) \cos\theta \, (\varepsilon_2^{1/2}(\omega) \cos\beta + \varepsilon_1^{1/2}(\omega) \cos\gamma)(1 + e^{2ik_{T'} d \cos\theta}) \\ &\quad + (\varepsilon_1^{1/2}(\omega) \varepsilon_2^{1/2}(\omega) \cos^2\theta + \varepsilon_M(\omega) \cos\beta \cos\gamma)(1 - e^{2ik_{T'} d \cos\theta}) . \\ &\overset{k_{T'} d \to 0}{\approx} 2\varepsilon_M^{1/2}(\omega) \cos\theta \, (\varepsilon_2^{1/2}(\omega) \cos\beta + \varepsilon_1^{1/2}(\omega) \cos\gamma) \end{aligned} \tag{A.38}$$

From Eq.(A.36) and (A.37), we can obtain the Fresnel's coefficients for the refractive and reflective light in the interfacial layer as

$$\begin{aligned} L_{T'} &\equiv \frac{E_{T'}}{E} \\ &\overset{k_{T'} d \to 0}{\approx} \frac{2\varepsilon_1^{1/2}(\omega) \cos\beta}{\varepsilon_2^{1/2}(\omega) \cos\beta + \varepsilon_1^{1/2}(\omega) \cos\gamma} \frac{\varepsilon_M^{1/2}(\omega) \cos\gamma + \varepsilon_2^{1/2}(\omega) \cos\theta}{2\varepsilon_M^{1/2}(\omega) \cos\theta} \end{aligned} \tag{A.39}$$

and

$$L_{R'} \equiv \frac{E_{R'}}{E} \overset{k_{T'}d\to 0}{\approx} \frac{\varepsilon_1^{1/2}(\omega)\cos\beta}{\varepsilon_2^{1/2}(\omega)\cos\beta + \varepsilon_1^{1/2}(\omega)\cos\gamma} \frac{\varepsilon_2^{1/2}(\omega)\cos\theta - \varepsilon_M^{1/2}(\omega)\cos\gamma}{\varepsilon_M^{1/2}(\omega)\cos\theta} \tag{A.40}$$

Appendix B: SFG intensity of a nonlinear thin film

Define $S(z) = \mathbf{e}_x \cdot \mathbf{E}_S^S(\mathbf{r} = (0,0,z), t = 0)$ and $S'(z) = \mathbf{e}_x \cdot \mathbf{H}_S^S(\mathbf{r} = (0,0,z), t = 0)$, the boundary conditions Eq.(19) and Eq.(20) can be rewritten as

$$\begin{aligned} &E_R^S = E_M^S + E_{M'}^S + S(0) \\ &\varepsilon_1^{1/2}(\omega_s)\cos\beta\, E_R^S = \varepsilon_M^{1/2}(\omega_s)\cos\theta\,(E_{M'}^S - E_M^S) + S'(0) \\ &E_T^S = E_M^S \exp(i\phi_M) + E_{M'}^S \exp(-i\phi_M) + S(d) \\ &\varepsilon_2^{1/2}(\omega_s)\cos\gamma\, E_T^S = \varepsilon_M^{1/2}(\omega_s)\cos\theta[E_M^S \exp(i\phi_M) - E_{M'}^S \exp(-i\phi_M)] + S'(d) \end{aligned} \tag{B.41}$$

here

$$\phi_M = k_M^S d\cos\theta \tag{B.42}$$

and the nonlinear source terms are given as

$$\begin{aligned} S(z) = 4\pi\chi_{yyz}^{(2)}\sin\theta_{IR}\{ &\frac{1}{\varepsilon_M(\omega_s) - \varepsilon_S(\omega_s)}[E_{T'}^{Vis}E_{T'}^{IR}\exp(izk_S\cos\theta_S) + E_{R'}^{Vis}E_{R'}^{IR}\exp(-izk_S\cos\theta_S)] \\ &+ \frac{1}{\varepsilon_M(\omega_s) - \varepsilon_{S'}(\omega_s)}[E_{T'}^{Vis}E_{R'}^{IR}\exp(iazk_{S'}\cos\theta_{S'}) + E_{R'}^{Vis}E_{T'}^{IR}\exp(-iazk_{S'}\cos\theta_{S'})]\} \end{aligned} \tag{B.43}$$

$$\begin{aligned} S'(z) = 4\pi\chi_{yyz}^{(2)}\sin\theta_{IR}\{ &\frac{\varepsilon_S^{1/2}\cos\theta_S}{\varepsilon_M - \varepsilon_S}[-E_{T'}^{Vis}E_{T'}^{IR}\exp(izk_S\cos\theta_S) + E_{R'}^{Vis}E_{R'}^{IR}\exp(-izk_S\cos\theta_S)] \\ &+ \frac{\varepsilon_{S'}^{1/2}\cos\theta_{S'}}{\varepsilon_{S'} - \varepsilon_M}[-E_{T'}^{Vis}E_{R'}^{IR}\exp(izk_{S'}\cos\theta_{S'}) + E_{R'}^{Vis}E_{T'}^{IR}\exp(-izk_{S'}\cos\theta_{S'})]\} \end{aligned} \tag{B.44}$$

with

$$\begin{aligned}\varepsilon_S(\omega_S) &= \frac{c^2}{{\omega_S}^2}(\mathbf{k}_{T'}^{Vis}+\mathbf{k}_{T'}^{IR})\cdot(\mathbf{k}_{T'}^{Vis}+\mathbf{k}_{T'}^{IR}) \\ &= \frac{\varepsilon_M(\omega_{Vis}){\omega_{Vis}}^2+\varepsilon_M(\omega_{IR}){\omega_{IR}}^2+2\varepsilon_M^{1/2}(\omega_{Vis})\varepsilon_M^{1/2}(\omega_{IR})\omega_{Vis}\omega_{IR}\cos(\theta_{Vis}-\theta_{IR})}{{\omega_S}^2}\end{aligned} \tag{B.45}$$

$$\sin\theta_S = \frac{\varepsilon_1^{1/2}(\omega_{Vis})\omega_{Vis}\sin\theta_{Vis}+\varepsilon_1^{1/2}(\omega_{IR})\omega_{IR}\sin\theta_{IR}}{\varepsilon_S^{1/2}(\omega_S)\omega_S} \tag{B.46}$$

$$\begin{aligned}\varepsilon_{S'}(\omega_S) &= \frac{c^2}{{\omega_S}^2}(\mathbf{k}_{T'}^{Vis}+\mathbf{k}_{R'}^{IR})\cdot(\mathbf{k}_{T'}^{Vis}+\mathbf{k}_{R'}^{IR}) \\ &= \frac{\varepsilon_M(\omega_{Vis}){\omega_{Vis}}^2+\varepsilon_M(\omega_{IR}){\omega_{IR}}^2-2\varepsilon_M^{1/2}(\omega_{Vis})\varepsilon_M^{1/2}(\omega_{IR})\omega_{Vis}\omega_{IR}\cos(\theta_{Vis}+\theta_{IR})}{{\omega_S}^2}\end{aligned} \tag{B.47}$$

$$\sin\theta_{S'} = \frac{\varepsilon_1^{1/2}(\omega_{Vis})\omega_{Vis}\sin\theta_{Vis}+\varepsilon_1^{1/2}(\omega_{IR})\omega_{IR}\sin\theta_{IR}}{\varepsilon_{S'}^{1/2}(\omega_S)\omega_S} \tag{B.48}$$

From Eq.(B.41), we can obtain the SFG electric fields in the interfacial layer and the reflection SFG field as

$$\begin{aligned}E_M^S = D^{-1}[&(\varepsilon_M{}^{1/2}(\omega_s)\cos\theta+\varepsilon_2{}^{1/2}(\omega_s)\cos\gamma)(S'(0)-\varepsilon_1{}^{1/2}(\omega_s)\cos\beta\,S(0))\exp(-i\phi_M) \\ &+(\varepsilon_1{}^{1/2}(\omega_s)\cos\beta-\varepsilon_M{}^{1/2}(\omega_s)\cos\theta)(S'(d)+\varepsilon_2{}^{1/2}(\omega_s)\cos\gamma\,S(d))]\end{aligned} \tag{B.49}$$

$$\begin{aligned}E_{M'}^S = -D^{-1}[&(\varepsilon_2{}^{1/2}(\omega_s)\cos\gamma-\varepsilon_M{}^{1/2}(\omega_s)\cos\theta)(S'(0)-\varepsilon_1{}^{1/2}(\omega_s)\cos\beta\,S(0))\exp(i\phi_M) \\ &+(\varepsilon_1{}^{1/2}(\omega_s)\cos\beta+\varepsilon_M{}^{1/2}(\omega_s)\cos\theta)(S'(d)+\varepsilon_2{}^{1/2}(\omega_s)\cos\gamma\,S(d))]\end{aligned} \tag{B.50}$$

$$\begin{aligned}E_R^S &= E_M^S+E_{M'}^S+S(0) \\ &= 2D^{-1}[\varepsilon_M{}^{1/2}(\omega_s)\cos\theta(\varepsilon_2{}^{1/2}(\omega_s)\cos\gamma\cos\phi_M-i\varepsilon_M{}^{1/2}(\omega_s)\cos\theta\sin\phi_M)S(0) \\ &\quad+(\varepsilon_M{}^{1/2}(\omega_s)\cos\theta\cos\phi_M-i\varepsilon_2{}^{1/2}(\omega_s)\cos\gamma\sin\phi_M)S'(0) \\ &\quad-\varepsilon_M{}^{1/2}(\omega_s)\cos\theta\varepsilon_2{}^{1/2}(\omega_s)\cos\gamma\,S(d)-\varepsilon_M{}^{1/2}(\omega_s)\cos\theta\,S'(d)]\end{aligned} \tag{B.51}$$

here

$$\begin{aligned}D &= (\varepsilon_M{}^{1/2}(\omega_s)\cos\theta+\varepsilon_2{}^{1/2}(\omega_s)\cos\gamma)(\varepsilon_M{}^{1/2}(\omega_s)\cos\theta+\varepsilon_1{}^{1/2}(\omega_s)\cos\beta)\exp(-i\phi_M) \\ &\quad+(\varepsilon_1{}^{1/2}(\omega_s)\cos\beta-\varepsilon_M{}^{1/2}(\omega_s)\cos\theta)(\varepsilon_M{}^{1/2}(\omega_s)\cos\theta-\varepsilon_2{}^{1/2}(\omega_s)\cos\gamma)\exp(i\phi_M) \\ &= 2\varepsilon_M{}^{1/2}(\omega_s)\cos\theta(\varepsilon_M{}^{1/2}(\omega_s)\cos\theta+\varepsilon_2{}^{1/2}(\omega_s)\cos\gamma)\cos\phi_M \\ &\quad-2i(\varepsilon_1{}^{1/2}(\omega_s)\cos\beta\varepsilon_2{}^{1/2}(\omega_s)\cos\gamma+\varepsilon_M(\omega_s)\cos^2\theta)\sin\phi_M\end{aligned} \tag{B.52}$$

Now take the limit $k_{T'}d \to 0$, we have

$$D \overset{k_{T'}d\to 0}{\approx} 2\varepsilon_M{}^{1/2}(\omega_s)\cos\theta\,(\varepsilon_1{}^{1/2}(\omega_s)\cos\beta + \varepsilon_2{}^{1/2}(\omega_s)\cos\gamma) \tag{B.53}$$

$$\begin{aligned}
\Delta S &= S(d) - S(0) \\
&\overset{k_{T'}d\to 0}{\approx} 4\pi i d\frac{\omega_S}{c}\chi^{(2)}_{yyz}\sin\theta_2[\frac{\varepsilon_S{}^{1/2}(\omega_s)\cos\theta_S}{\varepsilon_M(\omega_s)-\varepsilon_S(\omega_s)}(E^{Vis}_{T'}E^{IR}_{T'} - E^{Vis}_{R'}E^{IR}_{R'}) \\
&\quad + \frac{\varepsilon_{S'}{}^{1/2}(\omega_s)\cos\theta_{S'}}{\varepsilon_M(\omega_s)-\varepsilon_{S'}(\omega_s)}(E^{Vis}_{T'}E^{IR}_{R'} - E^{Vis}_{R'}E^{IR}_{T'})] \\
&= -iS'(0)
\end{aligned} \tag{B.54}$$

$$\begin{aligned}
\Delta S' &= S'(d) - S'(0) \\
&= 4\pi i d\frac{\omega_s}{c}\chi^{(2)}_{yyz}(\omega_s)\sin\theta_2[-\frac{\varepsilon_S(\omega_s)\cos^2\theta_S}{\varepsilon_M(\omega_s)-\varepsilon_S(\omega_s)}(E^{Vis}_{T'}E^{IR}_{T'} + E^{Vis}_{R'}E^{IR}_{R'}) \\
&\quad - \frac{\varepsilon_{S'}(\omega_s)\cos^2\theta_{S'}}{\varepsilon_M(\omega_s)-\varepsilon_{S'}(\omega_s)}(E^{Vis}_{T'}E^{IR}_{R'} + E^{Vis}_{R'}E^{IR}_{T'})]
\end{aligned} \tag{B.55}$$

Insert Eq.(B.53), (B.54) and (B.55) into Eq.(B.51), we have

$$\begin{aligned}
E^S_R &\overset{k_{T'}d\to 0}{\approx} -\frac{\omega_s}{c}\frac{i\varepsilon_M(\omega_s)\cos^2\theta\,S(0) + i\varepsilon_2{}^{1/2}(\omega_s)\cos\gamma\,S'(0) + \varepsilon_2{}^{1/2}(\omega_s)\cos\gamma\Delta S + \Delta S'}{\varepsilon_1{}^{1/2}(\omega_s)\cos\beta + \varepsilon_2{}^{1/2}(\omega_s)\cos\gamma} \\
&= 4\pi i d\frac{\omega_s}{c}\chi^{(2)}_{yyz}(\omega_s)\sin\theta_{IR}\frac{1}{\varepsilon_1{}^{1/2}(\omega_s)\cos\beta + \varepsilon_2{}^{1/2}(\omega_s)\cos\gamma} \\
&\quad [\frac{\varepsilon_M(\omega_s)\cos^2\theta - \varepsilon_S(\omega_s)\cos^2\theta_S}{\varepsilon_M(\omega_s)-\varepsilon_S(\omega_s)}(E^{Vis}_{T'}E^{IR}_{T'} + E^{Vis}_{R'}E^{IR}_{R'}) \\
&\quad + \frac{\varepsilon_M(\omega_s)\cos^2\theta - \varepsilon_{S'}(\omega_s)\cos^2\theta_{S'}}{\varepsilon_M(\omega_s)-\varepsilon_{S'}(\omega_s)}(E^{Vis}_{T'}E^{IR}_{R'} + E^{Vis}_{R'}E^{IR}_{T'})] \\
&= 4\pi i d\frac{\omega_s}{c}\chi^{(2)}_{yyz}(\omega_s)\sin\theta_{IR}\frac{(E^{Vis}_{T'} + E^{Vis}_{R'})(E^{IR}_{T'} + E^{IR}_{R'})}{\varepsilon_1{}^{1/2}(\omega_s)\cos\beta + \varepsilon_2{}^{1/2}(\omega_s)\cos\gamma}
\end{aligned} \tag{B.56}$$

Note that, in our SFG setting, the visible light is *s*-polarized. Using Eq.(A.19) and (A.20), we have

$$E^{Vis}_{T'} = L^{Vis}_{T'}E^{Vis}, E^{Vis}_{R'} = L^{Vis}_{R'}E^{Vis}, \tag{B.57}$$

with the Fresnel's coefficients given as

$$L_{T'}^{Vis} = \frac{2\varepsilon_1^{1/2}(\omega_{Vis})\cos\beta_{Vis}}{\varepsilon_1^{1/2}(\omega_{Vis})\cos\beta_{Vis} + \varepsilon_2^{1/2}(\omega_{Vis})\cos\gamma_{Vis}} \frac{\varepsilon_M^{1/2}(\omega_{Vis})\cos\theta_{Vis} + \varepsilon_2^{1/2}(\omega_{Vis})\cos\gamma_{Vis}}{2\varepsilon_M^{1/2}(\omega_{Vis})\cos\theta_{Vis}}, \quad \text{(B.58)}$$

and

$$L_{R'}^{Vis} = \frac{\varepsilon_1^{1/2}(\omega_{Vis})\cos\beta_{Vis}}{\varepsilon_1^{1/2}(\omega_{Vis})\cos\beta_{Vis} + \varepsilon_2^{1/2}(\omega_{Vis})\cos\gamma_{Vis}} \frac{\varepsilon_M^{1/2}(\omega_{Vis})\cos\theta_{Vis} - \varepsilon_2^{1/2}(\omega_{Vis})\cos\gamma_{Vis}}{\varepsilon_M^{1/2}(\omega_{Vis})\cos\theta_{Vis}}. \quad \text{(B.59)}$$

For the p-polarized IR light, using Eq. and , we have

$$E_{T'}^{IR} = L_{T'}^{IR} E^{IR}, E_{R'}^{IR} = L_{R'}^{IR} E^{IR}, \quad \text{(B.60)}$$

with the Fresnel's coefficients given as

$$L_{T'}^{IR} = \frac{2\varepsilon_1^{1/2}(\omega_{IR})\cos\beta_{IR}}{\varepsilon_2^{1/2}(\omega_{IR})\cos\beta_{IR} + \varepsilon_1^{1/2}(\omega_{IR})\cos\gamma_{IR}} \frac{\varepsilon_M^{1/2}(\omega_{IR})\cos\gamma_{IR} + \varepsilon_2^{1/2}(\omega_{IR})\cos\theta_{IR}}{2\varepsilon_M^{1/2}(\omega_{IR})\cos\theta_{IR}}, \quad \text{(B.61)}$$

and

$$L_{R'}^{IR} = \frac{\varepsilon_1^{1/2}(\omega_{IR})\cos\beta_{IR}}{\varepsilon_2^{1/2}(\omega_{IR})\cos\beta_{IR} + \varepsilon_1^{1/2}(\omega_{IR})\cos\gamma_{IR}} \frac{\varepsilon_2^{1/2}(\omega_{IR})\cos\theta_{IR} - \varepsilon_M^{1/2}(\omega_{IR})\cos\gamma_{IR}}{\varepsilon_M^{1/2}(\omega_{IR})\cos\theta_{IR}}. \quad \text{(B.62)}$$

Using Eq.(B.57) and (B.60), we can further rewrite Eq.(B.56) as

$$E_R^S \overset{k_{T'}d\to 0}{\approx} 2\pi i \frac{\omega_s}{c} \frac{\sec\beta}{\varepsilon_1^{1/2}(\omega_s)} \chi_{eff}(\omega_s) L^S (L_{T'}^{Vis} + L_{R'}^{Vis})(L_{T'}^{IR} + L_{R'}^{IR}) E^{Vis} E^{IR}, \quad \text{(B.63)}$$

here

$$\chi_{eff}(\omega_s) = d\chi_{yyz}^{(2)}(\omega_s)\sin\theta_{IR}, \quad \text{(B.64)}$$

$$L^S = \frac{2\varepsilon_1^{1/2}(\omega_s)\cos\beta}{\varepsilon_2^{1/2}(\omega_s)\cos\gamma + \varepsilon_1^{1/2}(\omega_s)\cos\beta}, \quad \text{(B.65)}$$

Note that

$$L_{T'}^{Vis} + L_{R'}^{Vis} = \frac{2\varepsilon_1^{1/2}(\omega_{Vis})\cos\beta_{Vis}}{\varepsilon_1^{1/2}(\omega_{Vis})\cos\beta_{Vis} + \varepsilon_2^{1/2}(\omega_{Vis})\cos\gamma_{Vis}} = L_T^{Vis}$$
$$L_{T'}^{IR} + L_{R'}^{IR} = \frac{2\varepsilon_1^{1/2}(\omega_{IR})\cos\beta_{IR}}{\varepsilon_2^{1/2}(\omega_{IR})\cos\beta_{IR} + \varepsilon_1^{1/2}(\omega_{IR})\cos\gamma_{IR}} \frac{\varepsilon_2^{1/2}(\omega_{IR})}{\varepsilon_M^{1/2}(\omega_{IR})} = L_T^{IR} \frac{\varepsilon_2^{1/2}(\omega_{IR})}{\varepsilon_M^{1/2}(\omega_{IR})} \quad \text{(B.66)}$$

Eq.(B.63) can be rewritten as

$$E_R^S \overset{k_T \cdot d \to 0}{\approx} 2\pi i \frac{\omega_s}{c} \frac{\sec\beta}{\varepsilon_1^{1/2}(\omega_s)} \chi_{eff}(\omega_s) L^S L_T^{Vis} L_T^{IR} \frac{\varepsilon_2^{1/2}(\omega_{IR})}{\varepsilon_M^{1/2}(\omega_{IR})} E^{Vis} E^{IR}, \quad \text{(B.67)}$$

here

$$L_T^{Vis} = \frac{2\varepsilon_1^{1/2}(\omega_{Vis})\cos\beta_{Vis}}{\varepsilon_1^{1/2}(\omega_{Vis})\cos\beta_{Vis} + \varepsilon_2^{1/2}(\omega_{Vis})\cos\gamma_{Vis}}$$
$$L_T^{IR} = \frac{2\varepsilon_1^{1/2}(\omega_{IR})\cos\beta_{IR}}{\varepsilon_2^{1/2}(\omega_{IR})\cos\beta_{IR} + \varepsilon_1^{1/2}(\omega_{IR})\cos\gamma_{IR}} \quad \text{(B.68)}$$

are the Fresnel's coefficients for the transmitted visible and IR lights in the medium 2 (water in our case), respectively.

References

(1) Castner, D. G.; Ratner, B. D. *Surface Sciencxae* **2002**, *500*, 28-60.

(2) Kasemo, B. *Current Opinion in Solid State and Materials Science* **1998**, *3*, 451-459.

(3) Somorjai, G. A.; York, R. L.; Butcher, D.; Park, J. Y. *Physical Chemistry Chemical Physics* **2007**, *9*, 3500-3513.

(4) Chen, X. Y.; Clarke, M. L.; Wang, J.; Chen, Z. *International Journal of Modern Physics B* **2005**, *19*, 691-713.

(5) York, R. L.; Browne, W. K.; Geissler, P. L.; Somorjai, G. A. *Israel Journal of Chemistry* **in press**.

(6) Mermut, O.; York, R. L.; Phillips, D. C.; McCrea, K. R.; Ward, R. S.; Somorjai, G. A. *Biointerphases* **2006**, *1*, P5-P11.

(7) Wang, J.; Buck, S. M.; Even, M. A.; Chen, Z. *Journal of the American Chemical Society* **2002**, *124*, 13302-13305.

(8) Phillips, D. C.; York, R. L.; Mermut, O.; McCrea, K. R.; Ward, R. S.; Somorjai, G. A. *Journal of Physical Chemistry C* **2007**, *111*, 255-261.

(9) Watry, M. R.; Richmond, G. L. *Journal of Physical Chemistry B* **2002**, *106*, 12517-12523.

(10) Ji, N.; Shen, Y. R. *Journal of Chemical Physics* **2004**, *120*, 7107-7112.

(11) Kim, J.; Chou, K. C.; Somorjai, G. A. *Journal of Physical Chemistry B* **2002**, *106*, 9198-9200.

(12) Hatch, S. R.; Polizzotti, R. S.; Dougal, S.; Rabinowitz, P. *Chemical Physics Letters* **1992**, *196*, 97-102.

(13) Conboy, J. C.; Messmer, M. C.; Richmond, G. L. *Journal of Physical Chemistry* **1996**, *100*, 7617-7622.

(14) Conboy, J. C.; Messmer, M. C.; Richmond, G. L. *Journal of Physical Chemistry B* **1997**, *101*, 6724-6733.

(15) Lobau, J.; Wolfrum, K. *Journal of the Optical Society of America B-Optical Physics* **1997**, *14*, 2502-2512.

(16) Lobau, J.; Wolfrum, K. *Laser Physics* **1998**, *8*, 582-592.

(17) Williams, C. T.; Yang, Y.; Bain, C. D. *Langmuir* **2000**, *16*, 2343-2350.

(18) Hatch, S. R.; Polizzotti, R. S.; Dougal, S.; Rabinowitz, P. *Journal of Vacuum Science & Technology A-Vacuum Surfaces and Films* **1993**, *11*, 2232-2238.

(19) Yang, Y. J.; Pizzolatto, R. L.; Messmer, M. C. *Journal of the Optical Society of America B-Optical Physics* **2000**, *17*, 638-645.

(20) Gautam, K. S.; Schwab, A. D.; Dhinojwala, A.; Zhang, D.; Dougal, S. M.; Yeganeh, M. S. *Physical Review Letters* **2000**, *85*, 3854-3857.

(21) Nishi, N.; Hobara, D.; Yamamoto, M.; Kakiuchi, T. *Analytical Sciences* **2003**, *19*, 887-890.

(22) Harp, G. P.; Rangwalla, H.; Yeganeh, M. S.; Dhinojwala, A. *Journal of the American Chemical Society* **2003**, *125*, 11283-11290.

(23) Knock, M. M.; Bell, G. R.; Hill, E. K.; Turner, H. J.; Bain, C. D. *Journal of Physical Chemistry B* **2003**, *107*, 10801-10814.

(24) Strunk, M. R.; Williams, C. T. *Langmuir* **2003**, *19*, 9210-9215.

(25) Rangwalla, H.; Dhinojwala, A. *Journal of Adhesion* **2004**, *80*, 37-59.

(26) Dreesen, L.; Sartenaer, Y.; Humbert, C.; Mani, A. A.; Lemaire, J. J.; Methivier, C.; Pradier, C. M.; Thiry, P. A.; Peremans, A. *Thin Solid Films* **2004**, *464*, 373-378.

(27) Kweskin, S. J.; Komvopoulos, K.; Somorjai, G. A. *Langmuir* **2005**, *21*, 3647-3652.

(28) Yeganeh, M. S.; Dougal, S. A.; Silbernagel, B. G. *Langmuir* **2006**, *22*, 637-641.

(29) Kweskin, S. J.; Rioux, R. M.; Habas, S. E.; Komvopoulos, K.; Yang, P.; Somorjai, G. A. *Journal of Physical Chemistry B* **2006**, *110*, 15920-15925.

(30) Wang, J.; Even, M. A.; Chen, X. Y.; Schmaier, A. H.; Waite, J. H.; Chen, Z. *Journal of the American Chemical Society* **2003**, *125*, 9914-9915.

(31) Chen, X. Y.; Wang, J.; Sniadecki, J. J.; Even, M. A.; Chen, Z. *Langmuir* **2005**, *21*, 2662-2664.

(32) Wang, J.; Chen, X. Y.; Clarke, M. L.; Chen, Z. *Proceedings of the National Academy of Sciences of the United States of America* **2005**, *102*, 4978-4983.

(33) Miranda, P. B.; Shen, Y. R. *Journal of Physical Chemistry B* **1999**, *103*, 3292-3307.

(34) Shen, Y. R.; Ostroverkhov, V. *Chemical Reviews* **2006**, *106*, 1140-1154.

(35) www.luxpop.com.

(36) Mermut, O.; Phillips, D. C.; York, R. L.; McCrea, K. R.; Ward, R. S.; Somorjai, G. A. *Journal of the American Chemical Society* **2006**, *128*, 3598-3607.

(37) Bloembergen, N.; Pershan, P. S. *Physical Review* **1962**, *128*, 606-622.

(38) Lambert, A. G.; Davies, P. B.; Neivandt, D. J. *Applied Spectroscopy Reviews* **2005**, *40*, 103-145.

(39) Boyd, R. W. *Nonlinear Optics*; 2nd ed.; Academic Press: San Diego, 2003.

(40) Hirose, C.; Akamatsu, N.; Domen, K. *Applied Spectroscopy* **1992**, *46*, 1051-1072.

(41) York, R. L.; Mermut, O.; Phillips, D. C.; McCrea, K. R.; Ward, R. S.; Somorjai, G. A. *Journal of Physical Chemistry C* **2007**, *111*, 8866-8871.

(42) Reva, I. D.; Stepanian, S. G.; Plokhotnichenko, A. M.; Radchenko, E. D.; Sheina, G. G.; Blagoi, Y. P. *Journal of Molecular Structure* **1994**, *318*, 1-13.

(43) Seo, Y. S.; Satija, S. *Langmuir* **2006**, *22*, 7113-7116.

(44) Du, Q.; Superfine, R.; Freysz, E.; Shen, Y. R. *Physical Review Letters* **1993**, *70*, 2313-2316.

(45) Du, Q.; Freysz, E.; Shen, Y. R. *Science* **1994**, *264*, 826-828.

(46) Walker, D. S.; Brown, M.; McFearin, C. L.; Richmond, G. L. *Journal of Physical Chemistry B* **2004**, *108*, 2111-2114.

(47) Walker, D. S.; Moore, F. G.; Richmond, G. L. *Journal of Physical Chemistry C* **2007**, *111*, 6103-6112.

Chapter 6

Sum Frequency Generation Vibrational Spectroscopy of the Amide I Mode of Interfacial Peptides Using a New Optical Parametric Amplifier based on Lithium Thioindate

The interfacial secondary structure of a model polypeptide has been studied at the hydrophobic deuterated polystyrene (d_8-PS)/buffer interface and the hydrophilic calcium fluoride (CaF_2)/buffer interface. The model polypeptide (which is known to be alpha-helical in the bulk solution under high ionic strength conditions and random coil in the bulk solution under low ionic strength conditions) contains hydrophobic leucyl (L) residues and hydrophilic lysyl (K) residues, with sequence Ac-LKKLLKLLKKLKL-NH_2. For this investigation, we have used surface-specific sum frequency generation (SFG) vibrational spectroscopy of the Amide I vibrational mode. In order to create tunable infrared light at these frequencies, we have built a new optical parametric amplifier that employs lithium thioindate. The Amide I mode at the d_8-PS/buffer interface was found to be centered around 1650 cm^{-1}, independent of the ionic strength of the solution (and hence the peptide's bulk solution secondary structure). This is interpreted has the peptide having similar secondary structure when adsorbed on the hydrophobic surface, independent of the bulk solution secondary structure, although other interpretations are discussed. At the hydrophilic CaF_2/buffer interface, the Amide I mode was found to be centered around 1670 cm^{-1} (when adsorbed from a solution in which the

peptide had alpha helical structure), suggesting a different interfacial secondary structure than the peptide adsorbed to a hydrophobic surface.

6.1. Introduction

The interaction of biological molecules and solid surfaces has important consequences for the biomaterial community, in addition to being an open fundamental problem.[1-3] It is well understood that a protein or peptide can denature as it adsorbs onto a solid surface (i.e. secondary structure is changed or often completely lost).[4] However, measuring the change in secondary structure (at the molecular level) when a protein or polypeptide adsorbs onto a solid surface has proven difficult to do with true surface specificity.

In recent years, several groups have turned to surface-specific sum frequency generation (SFG) vibrational spectroscopy to probe the interfacial structure of proteins and peptides with solid surfaces.[5-7] Here, we present a new type of optical parametric amplifier (OPA) based on lithium thioindate, $LiInS_2$ (LIS),[8,9] which more easily allows for the SFG measurement of the backbone Amide I mode (usually somewhere between 1600 cm^{-1} and 1700 cm^{-1}). The frequency of this mode is sensitive to the secondary structure of interfacial peptides.[10] For example, it is generally accepted in infrared and Raman spectroscopy that an Amide I mode observed around 1650 cm^{-1} is characteristic of an α-helix; whereas, a β-sheet has a characteristic Amide I mode observed at 1630 cm^{-1} and 1690 cm^{-1}.[10]

Although many SFG studies of biomolecules at surfaces have focused on the spectral window 2800-3100 cm^{-1}, Chen and coworkers have been studying the Amide I vibrational mode since 2003.[11-14] In one of their studies[13] they show that, much like in infrared and Raman spectroscopy, the frequency of the Amide I mode is sensitive to peptide secondary structure. In this study, they show that the Amide I mode of an α-

helical peptide at a hydrophobic surface (measured by SFG) is observed as a single peak centered around 1650 cm^{-1}.

In this report, we present the study of the interfacial Amide I mode of a model peptide, the LK_{14} peptide, which is composed of hydrophobic leucine (L) and lysine (K) residues.[15-17] This peptide is known to fold into an α-helix in solution if the ionic strength of the solution is sufficiently high; if the ionic strength is below a certain concentration, this peptide is known to be a random coil in solution.[15,18] We have found that the frequency of the interfacial Amide I mode (measured by SFG) at the hydrophobic deuterated polystyrene (d_8-PS)/buffer interface is independent of its solution secondary structure. Furthermore, the frequency of this interfacial Amide I mode at this interface is characteristic of an α-helix. In the case of the peptide adsorbing from a high ionic strength solution, this is not very shocking: the results imply that the interfacial structure of this peptide is maintained upon adsorption. In the case of this peptide adsorbing from a low ionic strength solution, this is quite interesting behavior. The implication is that although the peptide has a random coil configuration in solution, the act of adsorption induces secondary structure (specifically α-helicity) in the peptide. The implication of this interpretation is that a solid surface can induce ordering and structure into a solution phase random coil peptide. Finally, we have observed the Amide I mode to be at 1670 cm^{-1} when this peptide is adsorbed from a high ionic strength solution to the hydrophilic calcium fluoride (CaF_2)/buffer interface. This implies a different interfacial secondary structure than the adsorbed peptide at the hydrophobic surface, and possibly partial denaturation of the peptide at the hydrophilic surface.

6.2. Experimental

6.2.1. Sum Frequency Generation

SFG is based on a second-order non-linear process whereby two beams are overlapped in space and time on a surface and the resultant light at the sum-frequency is measured. In picosecond infrared-visible SFG, the two beams can be created by pumping a series of non-linear crystals by the fundamental of a Nd:YAG laser (1064 nm). In our set-up, the visible (532 nm) is the second harmonic of this fundamental. The tunable infrared is created by sending a portion of the 532 nm light into a tunable optical parametric generator (OPG) consisting of two KTP crystals. The OPG creates two tunable beams (~900 and ~1300 nm) of which one (~1300 nm) is sent to the OPA stage, where it is mixed with the remaining 1064 nm light. This OPA stage often is composed of KTA or $LiNbO_3$ crystals, which provide strong conversion efficiencies out to ~5000 nm, where the efficiency becomes quite small. To go to longer wavelengths, one has several options, each having their own advantages and disadvantages. One possibility is to take the signal and idler from the KTA (the OPA stage) and mix them in a $AgGaSe_2$ crystal (a second OPA stage). This method can produce light to long wavelengths. Unfortunately, the disadvantages are two-fold. One, due to the fact that there are two OPAs, the beam quality is poor. Two, the energy output is low (~100 μJ @ 2000 cm^{-1}). Alternatively, one could replace the KTA crystals in the second stage with $AgGaS_2$, which allows for the conversion of infrared light to wavelengths longer than 5 μm (about the limit for KTA). Since there is only one OPA stage, the beam quality is greatly improved relatively to the $AgGaSe_2$ approach. The primary disadvantage of $AgGaS_2$ is its low damage threshold. This limits the power output from this approach. Additionally,

even if the average power per pulse is held below the damage threshold, damage occurs to the surface of this crystal, which with time lowers the power output. As a third alternative, we have chosen LIS, a new type of non-linear crystal, to be used as a replacement for $AgGaS_2$. The advantages of LIS are: more infrared intensity between 5000 and 7000 nm, a high damage threshold, lower price, and better beam quality than a two OPA set-up. Figure 6.1 shows a scheme of the new OPG/OPA.

Clearly, the power output of a crystal depends on the intensity of the incoming light. In order to decide how intense the incoming light should be, we first had to measure

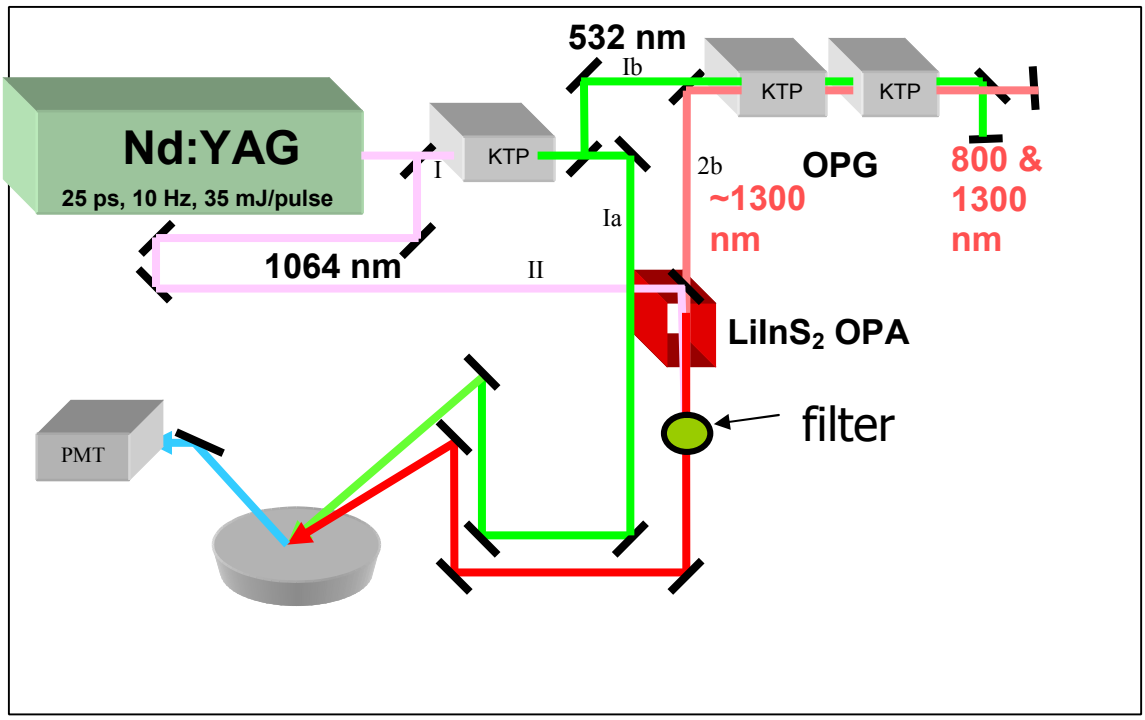

Figure 6.1. *Scheme of the OPG/OPA. Briefly, a pump laser sends light at 1064 nm into the OPG/OPA. This light is split into two beams (Beam I and Beam II). Beam I is sent into a KTP crystal, where it is frequency double to 532 nm. This beam is split into two (Beam Ia and Ib). Beam Ia is sent out of the OPG/OPA and becomes the visible (VIS) beam for our SFG experiment. Beam Ib is sent into a set of two angle tunable KTP*

crystals, whereby two more beams are created (beams 2a and 2b). This process is called optical parametric generation, and the sum of the frequency of beams 2a and 2b is equal to the frequency of beam 1b. Beam 2a (the "signal") is light at ca. 900 nm, and beam 2b (the "idler") is light at ca. 1300 nm, whereby the exact frequency of beams 2a and 2b is determined by the angles of the KTPs relative to the incoming beam 1b. Beam 2a is dumped, and beam 2b is sent to a second set of non-linear crystals (LIS). Here, beam II and beam 2b (the idler from stage 1 becomes the signal in stage 2) are mixed in the LIS crystals, and light at the difference frequency (between the two incoming beams) is created (this is called difference frequency generation or optical parametric amplification). This light (the idler from LIS) has a tunable wavelength between 5000 nm and 7000 nm. This light is sent out of the OPG/OPA and becomes the infrared (IR) for our SFG experiments.

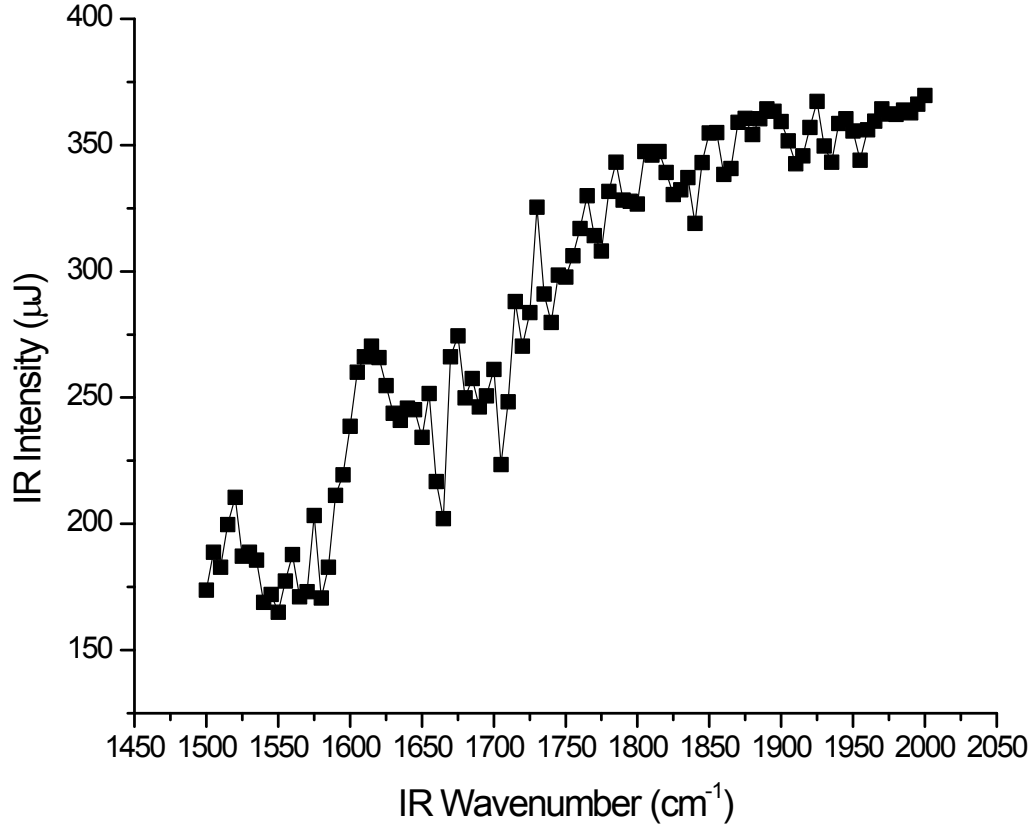

Figure 6.2. *Intensity output of LIS OPA. The intensity of the 1064 nm pump was 12 mJ/pulse.*

the damage threshold of LIS. For a 20 ps pulse, we found the damage threshold to be ~15 mJ/pulse. When pumping the LIS OPA with 12 mJ/pulse, the power output was measured and is shown in figue 6.2. The power output with this pump energy was not signifigantly increased by the addition of a second phase matched crystal.

6.2.2 Peptide Synthesis and Experimental Details

Peptide synthesis and experimental details, such as PBS buffer concentrations and SFG sample geometry are identical to our previous publications.[17,18] The sequence of the peptide studied here (named LK_{14}) is Ac-LKKLLKLLKKLLKL-NH_2.

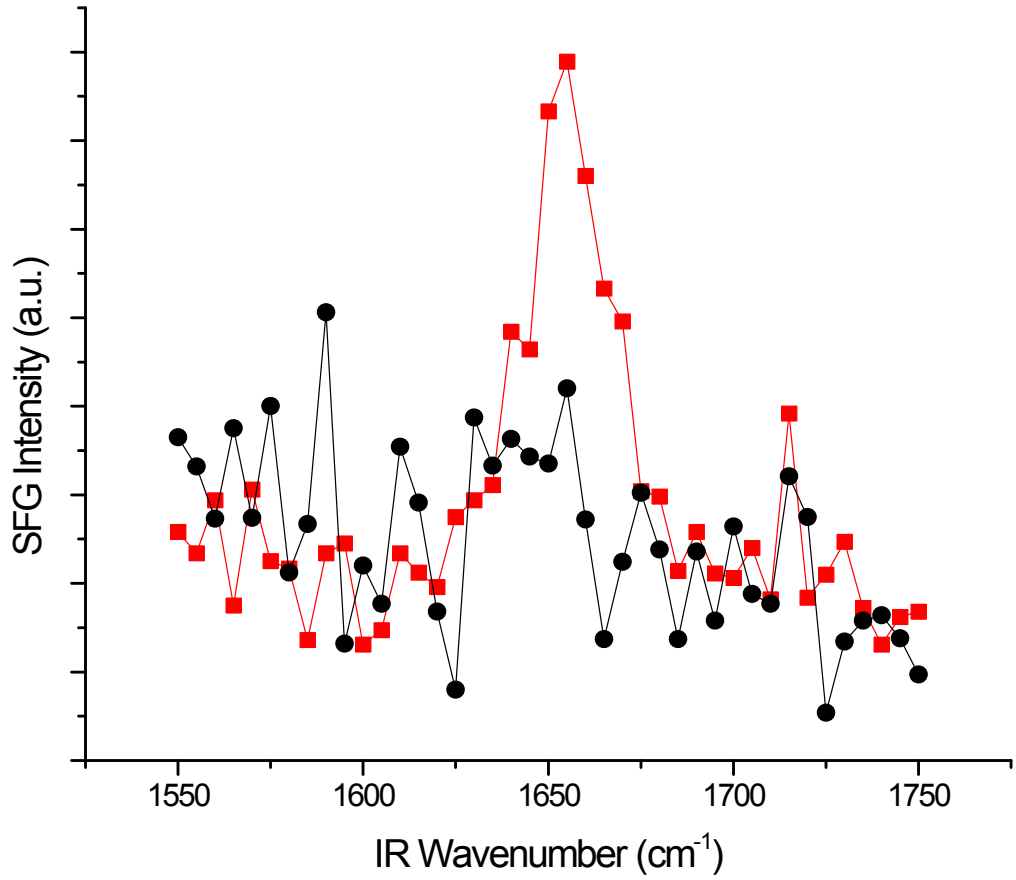

Figure 6.3. *The Amide I SFG spectrum of the LK_{14} under high ionic strength (1X) conditions (red squares) at the deuterated polystyrene/solution interface. The black circles are the SFG spectrum of the deuterated polystyrene/solution interface. The location of the Amide I mode centered at 1655 cm^{-1} is characteristic of an α-helical peptide.*

6.3 Results and Discussion

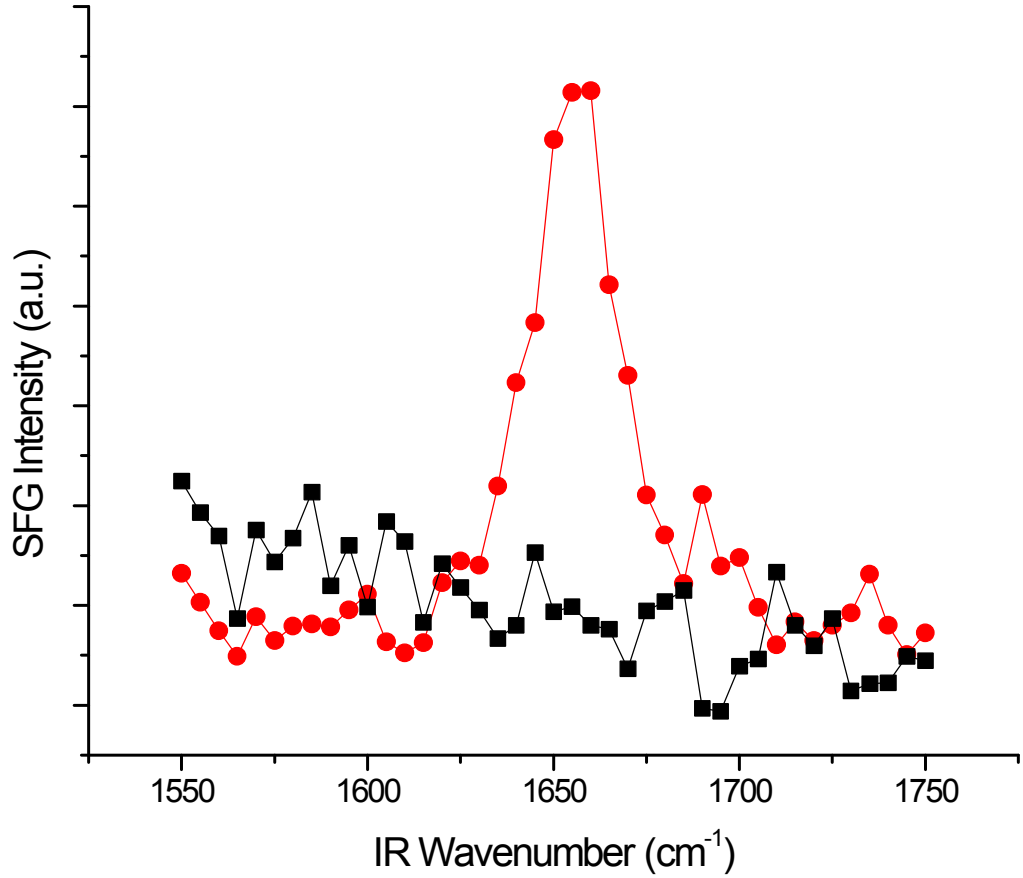

Figure 6.4. *The Amide I SFG spectrum of the LK_{14} under low ionic strength (0.01X) conditions (red circles) at the deuterated polystyrene/solution interface. The black squares are the SFG spectrum of the deuterated polystyrene/solution interface. The location of the Amide I mode centered at 1655 cm^{-1} is characteristic of an α-helical peptide. Note the similarity of the Amide I mode with Figure 6.3.*

The SFG spectrum of LK_{14} adsorbed from 1X PBS buffer at the d_8-PS/buffer interface is shown in Figure 6.3. The vibrational mode observed around 1655 cm^{-1} is assigned to the Amide I mode of the peptide backbone. It is well accepted in infrared, Raman, and more recently SFG studies that an Amide I mode at 1650 cm^{-1} can be

assigned to an α-helix.[10] Additionally, it has been established that the LK_{14} is an α-helix in solution under these experimental conditions.[15,18]

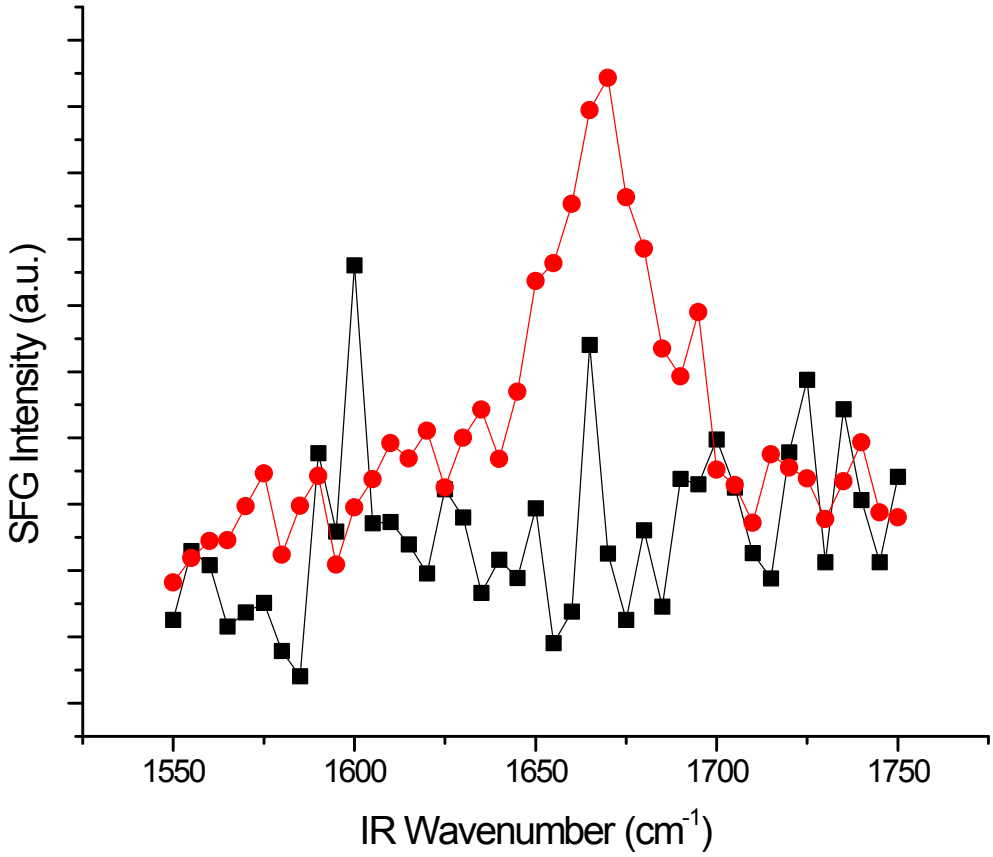

Figure 6.5. *The Amide I SFG spectrum of the LK_{14} under high ionic strength (1X) conditions (red circles) at the calcium fluoride/solution interface. The black squares are the SFG spectrum of the calcium fluoride/solution interface. The location of the Amide I mode centered at 1670 cm^{-1} is assigned to the Amide I mode of the peptide backbone. Note the difference between Figure 5 and the Amide I mode on the hydrophobic surface.*

Therefore, this spectrum is interpreted as showing that the LK_{14} has maintained its α-helical structure upon adsorption.

The SFG spectrum of LK_{14} adsorbed from 0.01X PBS buffer at the d_8-PS/buffer interface is shown in Figure 6.4. Again, a vibrational mode is observed at 1655 cm^{-1}. The similarities of Figure 6.3 and Figure 6.4 suggest that the peptide interfacial secondary structure is identical on the surface. This would imply that the random coil peptide in solution has assumed an α-helical structure upon adsorption. Surface induced ordering of polypeptides has been observed previously, especially in lipid bilayers and at the air/water interface.[19,20] However, this result is somewhat surprising, since at first glance this process would be entropically unfavorable. Additionally, the Amide I mode of a random coil peptide can also be observed around 1650 cm^{-1}. Therefore, we can not exclude the possibility that Figure 6.4 is showing the Amide I mode of a interfacial random coil.

The SFG spectrum of LK_{14} adsorbed from 1X PBS buffer at the CaF_2/buffer interface is shown in Figure 6.5. A vibrational mode is observed centered around 1670 cm^{-1}. This vibrational mode is assigned to the Amide I mode of the adsorbed peptide. The difference in frequency of the Amide I mode between the hydrophilic and hydrophobic surfaces suggests that the peptide has different secondary structures at the two surfaces. However, a precise picture of the secondary structure of LK_{14} on hydrophilic CaF_2 is not readily available from the data.

6.4. Conclusions

We have developed a new OPA based on LIS. This allows for the production of infrared light with wavelength between 1500 cm^{-1} and 2000 cm^{-1}. This new OPA has been used to measure the Amide I vibrational mode of a model peptide, LK_{14}. We have found that the frequency of the Amide I mode of this peptide at the hydrophobic d_8-

PS/buffer interface is independent of the secondary structure of the peptide in solution. This is interpreted has meaning the peptide has identical secondary structure at the d_8-PS/buffer interface, implying that a random coil in solution can become an ordered α-helix at the d_8-PS/buffer interface. It was found that the Amide I mode at the hydrophilic CaF_2/buffer interface was blue shifted from the hydrophobic d_8-PS/buffer interface, meaning the peptide had different secondary structure at those two interfaces.

References

(1) Castner, D. G.; Ratner, B. D. *Surface Science* **2002**, *500*, 28-60.

(2) Kasemo, B. *Current Opinion in Solid State and Materials Science* **1998**, *3*, 451-459.

(3) Somorjai, G. A.; York, R. L.; Butcher, D.; Park, J. Y. *Physical Chemistry Chemical Physics* **2007**, *9*, 3500-3513.

(4) *Proteins at Interfaces II: Fundamentals and Applications*; 1st ed.; American Chemical Society: Washington, D. C., 1995; Vol. 602.

(5) Chen, X. Y.; Clarke, M. L.; Wang, J.; Chen, Z. *International Journal of Modern Physics B* **2005**, *19*, 691-713.

(6) Wang, J.; Clarke, M. L.; Chen, X. Y.; Even, M. A.; Johnson, W. C.; Chen, Z. *Surface Science* **2005**, *587*, 1-11.

(7) York, R. L.; Browne, W. K.; Geissler, P. L.; Somorjai, G. A. *Israel Journal of Chemistry* **in press**.

(8) Fossier, S.; Salaun, S.; Mangin, J.; Bidault, O.; Thenot, I.; Zondy, J. J.; Chen, W.; Rotermund, F.; Petrov, V.; Petrov, P.; Henningsen, J.; Yelisseyev, A.; Isaenko,

L.; Lobanov, S.; Balachninaite, O.; Slekys, G.; Sirutkaitis, V. *Journal of the Optical Society of America B* **2004**, *21*, 1981-2007.

(9) Isaenko, L.; Vasilyeva, I.; Yelisseyev, A.; Lobanov, S.; Malakhov, Y.; Dovlitova, L.; Zondy, J. J.; Kavun, I. *Journal of Crystal Growth* **2000**, *218*, 313-322.

(10) Krimm, S.; Bandekar, J. *Advances in Protein Chemistry* **1986**, *38*, 181-364.

(11) Wang, J.; Even, M. A.; Chen, X. Y.; Schmaier, A. H.; Waite, J. H.; Chen, Z. *Journal of the American Chemical Society* **2003**, *125*, 9914-9915.

(12) Wang, J.; Chen, X. Y.; Clarke, M. L.; Chen, Z. *Proceedings of the National Academy of Sciences of the United States of America* **2005**, *102*, 4978-4983.

(13) Chen, X. Y.; Wang, J.; Sniadecki, J. J.; Even, M. A.; Chen, Z. *Langmuir* **2005**, *21*, 2662-2664.

(14) Chen, X. Y.; Chen, Z. *Biochimica Et Biophysica Acta-Biomembranes* **2006**, *1758*, 1257-1273.

(15) Degrado, W. F.; Lear, J. D. *Journal of the American Chemical Society* **1985**, *107*, 7684-7689.

(16) Long, J. R.; Oyler, N.; Drobny, G. P.; Stayton, P. S. *Journal of the American Chemical Society* **2002**, *124*, 6297-6303.

(17) Mermut, O.; Phillips, D. C.; York, R. L.; McCrea, K. R.; Ward, R. S.; Somorjai, G. A. *Journal of the American Chemical Society* **2006**, *128*, 3598-3607.

(18) York, R. L.; Mermut, O.; Phillips, D. C.; McCrea, K. R.; Ward, R. S.; Somorjai, G. A. *Journal of Physical Chemistry C* **2007**, *111*, 8866-8871.

(19) Kerth, A.; Erbe, A.; Dathe, M.; Blume, A. *Biophysical Journal* **2004**, *86*, 3750-3758.

(20) Dieudonne, D.; Gericke, A.; Flach, C. R.; Jiang, X.; Farid, R. S.; Mendelsohn, R. J. *Journal of the American Chemical Society* **1998**, *120*, 792-799.